Gallagher, S.J., Fulthorpe, C.S., Bogus, K., and the Expedition 356 Scientists
Proceedings of the International Ocean Discovery Program Volume 356
publications.iodp.org

doi:10.14379/iodp.proc.356.108.2017

Site U1463[1]

S.J. Gallagher, C.S. Fulthorpe, K. Bogus, G. Auer, S. Baranwal, I.S. Castañeda, B.A. Christensen, D. De Vleeschouwer, D.R. Franco, J. Groeneveld, M. Gurnis, C. Haller, Y. He, J. Henderiks, T. Himmler, T. Ishiwa, H. Iwatani, R.S. Jatiningrum, M.A. Kominz, C.A. Korpanty, E.Y. Lee, E. Levin, B.L. Mamo, H.V. McGregor, C.M. McHugh, B.F. Petrick, D.C. Potts, A. Rastegar Lari, W. Renema, L. Reuning, H. Takayanagi, and W. Zhang[2]

Keywords: International Ocean Discovery Program, IODP, Expedition 356, *JOIDES Resolution*, Site U1463, Northern Carnarvon Basin, Indonesian Throughflow, Miocene, Pliocene, Pleistocene, Australian monsoon, subsidence, aridity, anhydrite, tropical carbonates

Contents

Background and objectives

International Ocean Discovery Program (IODP) Site U1463 is ~150 m from the Picard-1 industry well (141 m water depth) on a flat outer ramp region (James et al., 2004). The site is 100 km southwest of IODP Site U1464 (Figures **F1**, **F2**). The seabed in the region is poorly sorted carbonate-rich (>90%) sediment made up of bioclastic gravel, sand, and mud (Jones, 1973; James et al., 2004). The wireline gamma ray log data from the Picard-1 Well reveals high variability and an upward reduction that is interpreted to be related to subsidence, glacioeustatic fluctuations, and climate variability from the Pliocene to recent.

The primary aim of coring Site U1463 was to obtain a Pliocene–Pleistocene tropical–subtropical carbonate record that will allow us to determine the subsidence, interglacial Australian monsoon, and tropical shelf-edge oceanographic histories of the region. An additional objective was to date a distinctive irregular seismic reflector postulated to be of Miocene age (Figure **F3**). Improving the age constraints on this feature will enhance regional seismic interpretations.

Operations

Transit to Site U1463

After the 131 nmi transit from IODP Site U1462, the vessel arrived at Site U1463 at 1535 h (UTC + 8 h) on 12 September 2015. Shortly after arrival, a seafloor positioning beacon was deployed.

Site U1463

Site U1463 consisted of four holes (Tables **T1**, **T2**). Hole U1463A was started with the extended core barrel (XCB) system to determine the nature of the seafloor. After recovering two cores, one of which contained soft mud, we decided that the advanced piston corer (APC) system would work at this site. Therefore, we piston cored Hole U1463B with both the APC and half-length APC (HLAPC) systems to 284.4 m drilling depth below seafloor (DSF). After partial strokes with the HLAPC system, we changed over to the XCB system. The hole was cored to a final depth of 530 m DSF. With excellent hole conditions, we decided it would be prudent to attempt the planned logging program for Site U1463. This had several advantages, including allowing us to more accurately allocate the remaining operating time at the site. Thus, after the completion of coring in Hole U1463B, a go-devil was pumped down the drill string to open the lockable float valve and the hole was conditioned for logging, including displacing the upper 360 m of the hole with heavy mud. Three logging tool deployments were completed. The triple combination (triple combo) tool string reached 454.7 m wireline log depth below seafloor (WSF) and completed both a down and up pass for the full depth of the open borehole. The Versatile Seismic Imager (VSI) tool string was assembled, and a single station was completed before whale sightings canceled the experiment. The Formation MicroScanner (FMS)-sonic tool string was deployed to 445.7 m WSF before encountering a bridge. After two FMS-sonic passes along the full length of the open hole, logging was completed and the tools recovered. The drill string was pulled out of the hole and the vessel was offset 20 m south of Hole U1463B. Hole U1463C was cored to APC refusal (280.7 m DSF). We then switched to the HLAPC system and coring continued to a remarkable 392.2 m DSF. After completing Hole U1463C and offsetting the vessel 20 m west, Hole U1463D was started. Hole U1463D was a virtual duplicate of Hole U1463C, except that the total depth was limited to 352.8 m DSF because this was the interval of scientific interest and also because of time constraints. The drill string was pulled back to the surface and secured for transit. The seafloor positioning beacon was

[1] Gallagher, S.J., Fulthorpe, C.S., Bogus, K., Auer, G., Baranwal, S., Castañeda, I.S., Christensen, B.A., De Vleeschouwer, D., Franco, D.R., Groeneveld, J., Gurnis, M., Haller, C., He, Y., Henderiks, J., Himmler, T., Ishiwa, T., Iwatani, H., Jatiningrum, R.S., Kominz, M.A., Korpanty, C.A., Lee, E.Y., Levin, E., Mamo, B.L., McGregor, H.V., McHugh, C.M., Petrick, B.F., Potts, D.C., Rastegar Lari, A., Renema, W., Reuning, L., Takayanagi, H., and Zhang, W., 2017. Site U1463. *In* Gallagher, S.J., Fulthorpe, C.S., Bogus, K., and the Expedition 356 Scientists, *Indonesian Throughflow*. Proceedings of the International Ocean Discovery Program, 356: College Station, TX (International Ocean Discovery Program).
http://dx.doi.org/10.14379/iodp.proc.356.108.2017
[2] **Expedition 356 Scientists' addresses.**
MS 356-108: Published 26 February 2017

Figure F1. Map of the northwest shelf showing major basins and location of modern and "fossil" reefs. Stars = Expedition 356 sites, green circles = Deep Sea Drilling Project/Ocean Drilling Program sites and other core locations referred to in text, yellow circles = industry well locations (Angel = Angel-1; G2/6/7 = Goodwyn-2, Goodwyn-6, Goodwyn-7; A1 = Austin-1; M/MN1 = Maitland/Maitland North-1; TR1 = West Tryal Rocks-1). WA = Western Australia, NT = Northern Territory, SA = South Australia, QLD = Queensland, NSW = New South Wales.

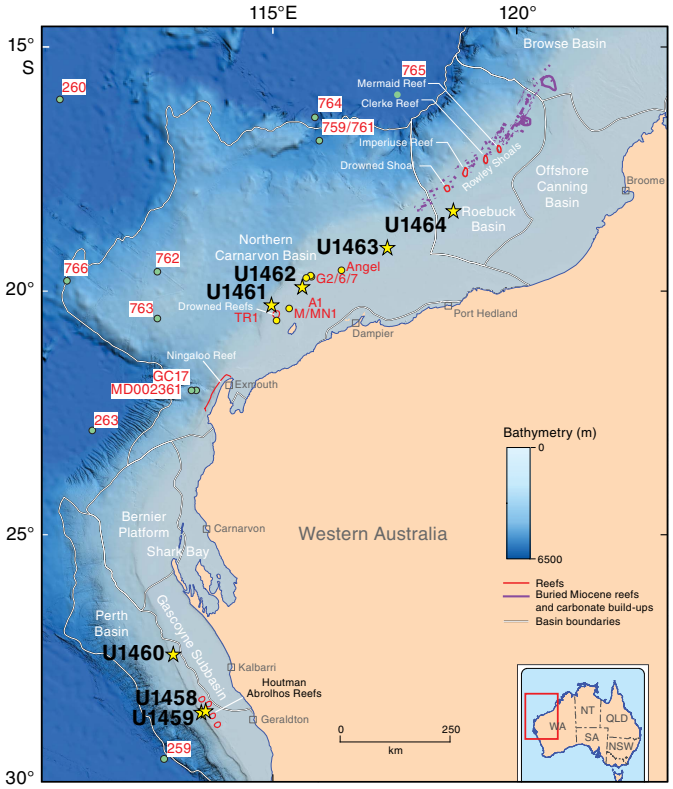

recovered and the thrusters and hydrophones were pulled back into the ship's hull before beginning the transit to Site U1464. The total time spent on Site U1463 was 147.0 h (6.13 days).

Overall, the APC system penetrated 840.3 m and recovered 835.29 m (99.4%) and 189.1 m was cored with the HLAPC system with 189.69 m of material recovered (100.3%). The XCB system cored 265.0 m and recovered 126.56 m (47.8%). The overall recovery for Site U1463 was 89.0%.

Hole U1463A

After offsetting the vessel from the beacon, preparations for coring in Hole U1463A (18°57.9181′S, 117°37.4217′E) commenced. The APC/XCB system was assembled. Given the previous difficulty with the mudline core at IODP Sites U1459 and U1462 (broken and bent core barrels, respectively), we decided to begin coring operations with the XCB coring system. An XCB core barrel was dressed with a core liner and dropped in preparation for beginning Hole U1463A. We tagged the seafloor and calculated the water depth to be 145.8 meters below sea level (mbsl). Hole U1463A was started at 1925 h on 12 September 2015. The first XCB core barrel returned empty (Core 356-U1463A-1X) and a second barrel was dropped. Core 2X recovered 8.59 m of soft mud. We decided to abandon Hole U1463A in order to begin a new hole (U1463B) with the APC system. Hole U1463A advanced 19.4 m and recovered 8.59 m of core (44.3% recovery). Hole U1463A ended at 2030 h. The total time spent on Hole U1463A was 9.75 h.

Hole U1463B

Hole U1463B (18°57.9190′S, 117°37.4340′E) began at 2100 h on 12 September 2015 with recovery of a mudline core (7.88 m). The water depth was calculated to be 145.4 mbsl. We recovered Cores 356-U1463B-1H through 30H to 271.2 m DSF. The HLAPC system was then deployed and we recovered Cores 31F through 33F to 284.4 m DSF, at which depth piston coring refusal was reached. The XCB coring system was deployed and coring continued from Core

Figure F2. Bathymetric map showing the seafloor around Sites U1463 and U1464. Bathymetric data are derived from the Geoscience Australia Australian bathymetry and topography grid, June 2009. The positions of multichannel seismic profiles are shown. Red dots = locations of preexisting industry wells.

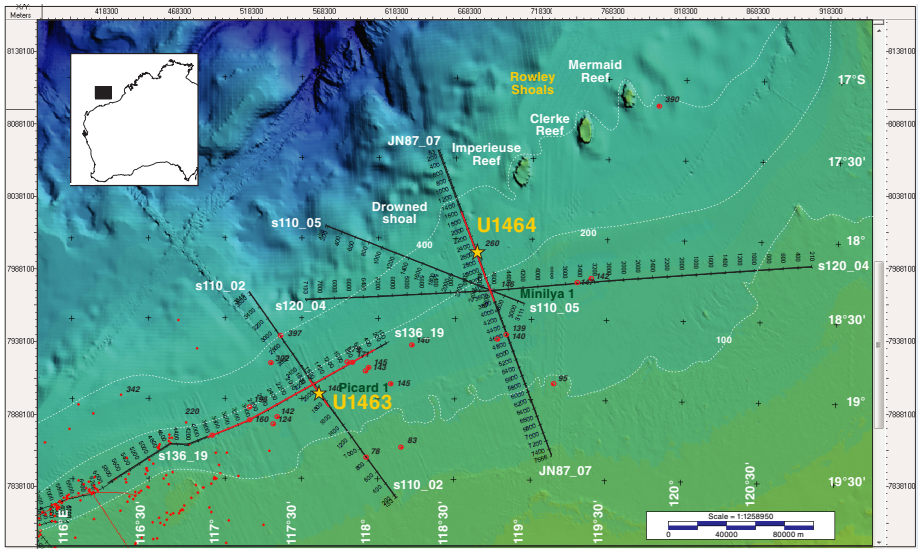

Figure F3. Multichannel seismic profile across Site U1463. Top of green shading = inferred top of the Miocene. SP = shotpoint.

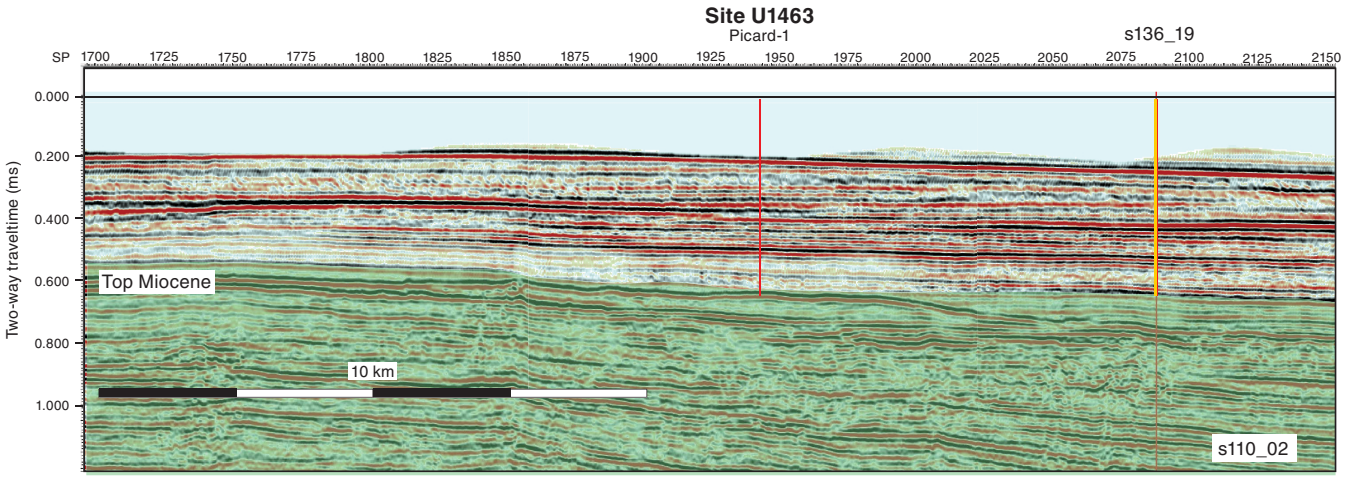

Table T1. Operations summary, Site U1463. mbsl = meters below sea level. **Download table in .csv format.**

Hole	Latitude	Longitude	Water depth (mbsl)	Penetration DSF (m)	Cored interval (m)	Recovered length (m)	Recovery (%)	Drilled interval (*N*)	Total cores (*N*)	APC cores (*N*)	HLAPC cores (*N*)	XCB cores (*N*)	RCB cores (*N*)	Time on hole (days)
U1463A	18°57.9181′S	117°37.4217′E	145.81	19.40	19.40	8.59	44	0	2	0	0	2	0	0.2
U1463B	18°57.9190′S	117°37.4340′E	145.41	530.00	530.00	399.00	75	0	60	30	3	27	0	3.08
U1463C	18°57.9295′S	117°37.4336′E	144.81	392.20	392.20	397.34	101	0	61	31	30	0	0	1.76
U1463D	18°57.9285′S	117°37.4216′E	144.60	352.80	352.80	346.61	98	0	47	32	15	0	0	1.16
		Totals:		1294.40	1294.40	1151.54		0	170	93	48	29	0	

Table T2. Site U1463 core summary. DSF = drilling depth below seafloor, CSF = core depth below seafloor. F = half-length advanced piston corer, H = advanced piston corer, X = extended core barrel. (Continued on next three pages.) **Download table in .csv format.**

Core	Top depth drilled DSF (m)	Bottom depth drilled DSF (m)	Advanced (m)	Recovered length (m)	Curated length (m)	Top depth cored CSF (m)	Bottom depth recovered CSF (m)	Recovery (%)	Date (2015)	Time on deck UTC (h)
356-U1463A-										
1X	0.00	9.70	9.7		0.00	0.00	0.00		12 Sep	1150
2X	9.70	19.40	9.7	8.59	8.59	9.70	18.29	89	12 Sep	1210
356-U1463B-										
1H	0.00	7.90	7.9	7.88	7.88	0.00	7.88	100	12 Sep	1305
2H	7.90	17.40	9.5	9.41	9.41	7.90	17.31	99	12 Sep	1335
3H	17.40	26.90	9.5	9.80	9.80	17.40	27.20	103	12 Sep	1400
4H	26.90	36.40	9.5	9.81	9.81	26.90	36.71	103	12 Sep	1415
5H	36.40	45.90	9.5	9.73	9.73	36.40	46.13	102	12 Sep	1435
6H	45.90	55.40	9.5	9.52	9.52	45.90	55.42	100	12 Sep	1455
7H	55.40	64.90	9.5	9.14	9.14	55.40	64.54	96	12 Sep	1515
8H	64.90	74.40	9.5	9.65	9.65	64.90	74.55	102	12 Sep	1530
9H	74.40	83.90	9.5	9.32	9.32	74.40	83.72	98	12 Sep	1555
10H	83.90	93.40	9.5	9.50	9.50	83.90	93.40	100	12 Sep	1640
11H	93.40	102.90	9.5	8.49	8.49	93.40	101.89	89	12 Sep	1700
12H	102.90	112.40	9.5	9.56	9.56	102.90	112.46	101	12 Sep	1720
13H	112.40	121.90	9.5	9.65	9.65	112.40	122.05	102	12 Sep	1740
14H	121.90	131.40	9.5	8.80	8.80	121.90	130.70	93	12 Sep	1800
15H	131.40	140.90	9.5	7.88	7.88	131.40	139.28	83	12 Sep	1825
16H	140.90	150.40	9.5	9.31	9.31	140.90	150.21	98	12 Sep	1925
17H	150.40	159.90	9.5	9.10	9.10	150.40	159.50	96	12 Sep	1945
18H	159.90	169.40	9.5	8.10	8.10	159.90	168.00	85	12 Sep	2100
19H	169.40	178.90	9.5	8.72	8.72	169.40	178.12	92	12 Sep	2120
20H	178.90	188.00	9.1	9.12	9.12	178.90	188.02	100	12 Sep	2200
21H	188.00	197.50	9.5	9.65	9.65	188.00	197.65	102	12 Sep	2240
22H	197.50	206.50	9.0	9.07	9.07	197.50	206.57	101	12 Sep	2315
23H	206.50	213.80	7.3	7.36	7.36	206.50	213.86	101	13 Sep	2350
24H	213.80	223.30	9.5	9.96	9.96	213.80	223.76	105	13 Sep	0035
25H	223.30	232.80	9.5	9.85	9.85	223.30	233.15	104	13 Sep	0110

Table T2 (continued). (Continued on next page.)

Core	Top depth drilled DSF (m)	Bottom depth drilled DSF (m)	Advanced (m)	Recovered length (m)	Curated length (m)	Top depth cored CSF (m)	Bottom depth recovered CSF (m)	Recovery (%)	Date (2015)	Time on deck UTC (h)
26H	232.80	241.40	8.6	8.60	8.60	232.80	241.40	100	13 Sep	0135
27H	241.40	250.90	9.5	9.86	9.86	241.40	251.26	104	13 Sep	0230
28H	250.90	256.00	5.1	5.19	5.19	250.90	256.09	102	13 Sep	0255
29H	256.00	265.50	9.5	9.97	9.97	256.00	265.97	105	13 Sep	0405
30H	265.50	271.20	5.7	5.73	5.73	265.50	271.23	101	13 Sep	0445
31F	271.20	275.90	4.7	4.91	4.91	271.20	276.11	104	13 Sep	0605
32F	275.90	279.70	3.8	3.88	3.88	275.90	279.78	102	13 Sep	0705
33F	279.70	284.40	4.7	4.51	4.51	279.70	284.21	96	13 Sep	0755
34X	284.40	292.40	8.0	9.34	9.34	284.40	293.74	117	13 Sep	0925
35X	292.40	302.10	9.7	9.87	9.87	292.40	302.27	102	13 Sep	1035
36X	302.10	311.10	9.0	6.11	6.11	302.10	308.21	68	13 Sep	1230
37X	311.10	320.80	9.7	8.45	8.45	311.10	319.55	87	13 Sep	1420
38X	320.80	330.50	9.7	6.82	6.82	320.80	327.62	70	13 Sep	1550
39X	330.50	340.20	9.7	6.96	6.96	330.50	337.46	72	13 Sep	1745
40X	340.20	344.20	4.0	5.03	5.03	340.20	345.23	126	13 Sep	1855
41X	344.20	350.60	6.4	0.00	0.00	344.20	344.20	0	13 Sep	2010
42X	350.60	360.30	9.7	9.81	9.81	350.60	360.41	101	13 Sep	2115
43X	360.30	370.00	9.7	9.04	9.04	360.30	369.34	93	13 Sep	2230
44X	370.00	379.70	9.7	9.08	9.08	370.00	379.08	94	13 Sep	2350
45X	379.70	389.40	9.7	9.31	9.31	379.70	389.01	96	14 Sep	0055
46X	389.40	399.10	9.7	6.19	6.19	389.40	395.59	64	14 Sep	0200
47X	399.10	408.80	9.7	6.83	6.83	399.10	405.93	70	14 Sep	0250
48X	408.80	418.50	9.7	3.64	3.64	408.80	412.44	38	14 Sep	0350
49X	418.50	428.20	9.7	0.78	0.78	418.50	419.28	8	14 Sep	0505
50X	428.20	437.90	9.7	1.16	1.16	428.20	429.36	12	14 Sep	0555
51X	437.90	447.60	9.7	0.11	0.11	437.90	438.01	1	14 Sep	0650
52X	447.60	457.30	9.7	0.35	0.35	447.60	447.95	4	14 Sep	0735
53X	457.30	467.00	9.7	0.12	0.12	457.30	457.42	1	14 Sep	0835
54X	467.00	476.70	9.7	0.37	0.37	467.00	467.37	4	14 Sep	0930
55X	476.70	486.40	9.7	7.80	7.80	476.70	484.50	80	14 Sep	1110
56X	486.40	496.10	9.7	0.40	0.40	486.40	486.80	4	14 Sep	1235
57X	496.10	505.80	9.7	0.09	0.09	496.10	496.19	1	14 Sep	1345
58X	505.80	515.50	9.7	0.21	0.21	505.80	506.01	2	14 Sep	1450
59X	515.50	525.20	9.7	0.05	0.05	515.50	515.55	1	14 Sep	1535
60X	525.20	530.00	4.8	0.05	0.05	525.20	525.25	1	14 Sep	1705
356-U1463C-										
1H	0.00	4.10	4.1	4.11	4.11	0.00	4.11	100	15 Sep	1835
2H	4.10	13.60	9.5	9.35	9.35	4.10	13.45	98	15 Sep	1910
3H	13.60	23.10	9.5	9.66	9.66	13.60	23.26	102	15 Sep	1940
4H	23.10	32.60	9.5	9.41	9.41	23.10	32.51	99	15 Sep	2015
5H	32.60	42.10	9.5	9.22	9.22	32.60	41.82	97	15 Sep	2035
6H	42.10	51.60	9.5	9.61	9.61	42.10	51.71	101	15 Sep	2100
7H	51.60	61.10	9.5	9.88	9.88	51.60	61.48	104	15 Sep	2135
8H	61.10	70.60	9.5	9.43	9.43	61.10	70.53	99	15 Sep	2200
9H	70.60	77.60	7.0	8.13	8.13	70.60	78.73	116	15 Sep	2230
10H	77.60	87.10	9.5	10.04	10.04	77.60	87.64	106	15 Sep	2320
11H	87.10	96.60	9.5	9.58	9.58	87.10	96.68	101	15 Sep	2340
12H	96.60	106.10	9.5	9.82	9.82	96.60	106.42	103	16 Sep	0010
13H	106.10	115.60	9.5	9.80	9.80	106.10	115.90	103	16 Sep	0100
14H	115.60	125.10	9.5	9.52	9.52	115.60	125.12	100	16 Sep	0125
15H	125.10	134.60	9.5	9.74	9.74	125.10	134.84	103	16 Sep	0200
16H	134.60	144.10	9.5	9.98	9.98	134.60	144.58	105	16 Sep	0245
17H	144.10	153.60	9.5	9.84	9.84	144.10	153.94	104	16 Sep	0315
18H	153.60	163.10	9.5	9.53	9.53	153.60	163.13	100	16 Sep	0345
19H	163.10	172.60	9.5	5.81	5.81	163.10	168.91	61	16 Sep	0410
20H	172.60	182.10	9.5	9.64	9.64	172.60	182.24	101	16 Sep	0500
21H	182.10	191.60	9.5	9.95	9.95	182.10	192.05	105	16 Sep	0525
22H	191.60	201.10	9.5	9.77	9.77	191.60	201.37	103	16 Sep	0550
23H	201.10	210.60	9.5	9.88	9.88	201.10	210.98	104	16 Sep	0615
24H	210.60	220.10	9.5	9.94	9.94	210.60	220.54	105	16 Sep	0655
25H	220.10	229.60	9.5	9.92	9.92	220.10	230.02	104	16 Sep	0725
26H	229.60	237.10	7.5	9.29	9.29	229.60	238.89	124	16 Sep	0800
27H	237.10	246.60	9.5	9.86	9.86	237.10	246.96	104	16 Sep	0830
28H	246.60	256.10	9.5	9.96	9.96	246.60	256.56	105	16 Sep	0920
29H	256.10	265.60	9.5	9.53	9.53	256.10	265.63	100	16 Sep	0955
30H	265.60	273.80	8.2	8.28	8.28	265.60	273.88	101	16 Sep	1035
31H	273.80	280.70	6.9	6.92	6.92	273.80	280.72	100	16 Sep	1115
32F	280.70	285.40	4.7	4.43	4.43	280.70	285.13	94	16 Sep	1225
33F	285.40	288.40	3.0	3.01	3.01	285.40	288.41	100	16 Sep	1250

Table T2 (continued). (Continued on next page.)

Core	Top depth drilled DSF (m)	Bottom depth drilled DSF (m)	Advanced (m)	Recovered length (m)	Curated length (m)	Top depth cored CSF (m)	Bottom depth recovered CSF (m)	Recovery (%)	Date (2015)	Time on deck UTC (h)
34F	288.40	292.30	3.9	3.96	3.96	288.40	292.36	102	16 Sep	1315
35F	292.30	297.00	4.7	4.73	4.73	292.30	297.03	101	16 Sep	1405
36F	297.00	301.70	4.7	4.75	4.75	297.00	301.75	101	16 Sep	1435
37F	301.70	306.40	4.7	4.93	4.93	301.70	306.63	105	16 Sep	1520
38F	306.40	311.10	4.7	4.86	4.86	306.40	311.26	103	16 Sep	1555
39F	311.10	311.80	0.7	0.69	0.69	311.10	311.79	99	16 Sep	1635
40F	311.80	314.40	2.6	2.67	2.67	311.80	314.47	103	16 Sep	1700
41F	314.40	317.70	3.3	3.31	3.31	314.40	317.71	100	16 Sep	1730
42F	317.70	321.20	3.5	3.52	3.52	317.70	321.22	101	16 Sep	1810
43F	321.20	324.50	3.3	3.30	3.30	321.20	324.50	100	16 Sep	1855
44F	324.50	328.60	4.1	4.12	4.12	324.50	328.62	100	16 Sep	1945
45F	328.60	330.60	2.0	2.06	2.06	328.60	330.66	103	16 Sep	2015
46F	330.60	334.70	4.1	4.11	4.11	330.60	334.71	100	16 Sep	2050
47F	334.70	338.80	4.1	4.11	4.11	334.70	338.81	100	16 Sep	2125
48F	338.80	340.00	1.2	1.25	1.25	338.80	340.05	104	16 Sep	2220
49F	340.00	343.60	3.6	3.63	3.63	340.00	343.63	101	16 Sep	2255
50F	343.60	346.80	3.2	3.29	3.29	343.60	346.89	103	16 Sep	2345
51F	346.80	349.80	3.0	3.05	3.05	346.80	349.85	102	17 Sep	0020
52F	349.80	353.20	3.4	3.42	3.42	349.80	353.22	101	17 Sep	0055
53F	353.20	356.50	3.3	3.32	3.32	353.20	356.52	101	17 Sep	0135
54F	356.50	361.20	4.7	4.53	4.53	356.50	361.03	96	17 Sep	0215
55F	361.20	365.90	4.7	4.88	4.88	361.20	366.08	104	17 Sep	0245
56F	365.90	370.60	4.7	3.87	3.87	365.90	369.77	82	17 Sep	0330
57F	370.60	375.30	4.7	4.84	4.84	370.60	375.44	103	17 Sep	0400
58F	375.30	380.00	4.7	4.80	4.80	375.30	380.10	102	17 Sep	0420
59F	380.00	384.00	4.0	4.02	4.02	380.00	384.02	101	17 Sep	0445
60F	384.00	387.50	3.5	3.49	3.49	384.00	387.49	100	17 Sep	0520
61F	387.50	392.20	4.7	4.99	4.99	387.50	392.49	106	17 Sep	0620
356-U1463D-										
1H	0.00	1.40	1.4	1.46	1.46	0.00	1.46	104	17 Sep	0950
2H	1.40	10.90	9.5	9.62	9.62	1.40	11.02	101	17 Sep	1025
3H	10.90	20.40	9.5	9.91	9.91	10.90	20.81	104	17 Sep	1045
4H	20.40	29.90	9.5	9.41	9.41	20.40	29.81	99	17 Sep	1105
5H	29.90	39.40	9.5	9.71	9.71	29.90	39.61	102	17 Sep	1120
6H	39.40	48.90	9.5	9.93	9.93	39.40	49.33	105	17 Sep	1135
7H	48.90	58.40	9.5	9.94	9.94	48.90	58.84	105	17 Sep	1155
8H	58.40	67.90	9.5	9.86	9.86	58.40	68.26	104	17 Sep	1210
9H	67.90	77.40	9.5	9.95	9.95	67.90	77.85	105	17 Sep	1230
10H	77.40	86.90	9.5	8.43	8.43	77.40	85.83	89	17 Sep	1250
11H	86.90	96.40	9.5	10.07	10.07	86.90	96.97	106	17 Sep	1310
12H	96.40	103.90	7.5	8.10	8.10	96.40	104.50	108	17 Sep	1330
13H	103.90	113.40	9.5	9.61	9.61	103.90	113.51	101	17 Sep	1355
14H	113.40	122.90	9.5	9.77	9.77	113.40	123.17	103	17 Sep	1415
15H	122.90	132.40	9.5	9.31	9.31	122.90	132.21	98	17 Sep	1430
16H	132.40	141.90	9.5	9.22	9.22	132.40	141.62	97	17 Sep	1450
17H	141.90	151.40	9.5	9.83	9.83	141.90	151.73	103	17 Sep	1515
18H	151.40	160.90	9.5	9.79	9.79	151.40	161.19	103	17 Sep	1535
19H	160.90	170.40	9.5	9.92	9.92	160.90	170.82	104	17 Sep	1600
20H	170.40	179.90	9.5	7.57	7.57	170.40	177.97	80	17 Sep	1620
21H	179.90	189.40	9.5	9.82	9.82	179.90	189.72	103	17 Sep	1640
22H	189.40	198.90	9.5	9.87	9.87	189.40	199.27	104	17 Sep	1705
23H	198.90	208.40	9.5	9.32	9.32	198.90	208.22	98	17 Sep	1745
24H	208.40	217.90	9.5	9.87	9.87	208.40	218.27	104	17 Sep	1810
25H	217.90	227.40	9.5	9.89	9.89	217.90	227.79	104	17 Sep	1845
26H	227.40	236.90	9.5	9.91	9.91	227.40	237.31	104	17 Sep	1930
27H	236.90	246.40	9.5	8.62	8.62	236.90	245.52	91	17 Sep	1950
28H	246.40	255.90	9.5	9.90	9.90	246.40	256.30	104	17 Sep	2015
29H	255.90	265.40	9.5	8.93	8.93	255.90	264.83	94	17 Sep	2040
30H	265.40	274.90	9.5	5.95	5.95	265.40	271.35	63	17 Sep	2105
31H	274.90	284.40	9.5	4.66	4.66	274.90	279.56	49	17 Sep	2135
32H	284.40	288.40	4.0	4.01	4.01	284.40	288.41	100	17 Sep	2210
33F	288.40	293.10	4.7	3.81	3.81	288.40	292.21	81	17 Sep	2250
34F	293.10	297.80	4.7	4.36	4.36	293.10	297.46	93	17 Sep	2325
35F	297.80	301.30	3.5	3.56	3.56	297.80	301.36	102	18 Sep	2350
36F	301.30	305.10	3.8	3.88	3.88	301.30	305.18	102	18 Sep	0030
37F	305.10	309.30	4.2	4.26	4.26	305.10	309.36	101	18 Sep	0105
38F	309.30	312.70	3.4	3.46	3.46	309.30	312.76	102	18 Sep	0135
39F	312.70	316.40	3.7	3.70	3.70	312.70	316.40	100	18 Sep	0205
40F	316.40	320.20	3.8	3.82	3.82	316.40	320.22	101	18 Sep	0250

Table T2 (continued).

Core	Top depth drilled DSF (m)	Bottom depth drilled DSF (m)	Advanced (m)	Recovered length (m)	Curated length (m)	Top depth cored CSF (m)	Bottom depth recovered CSF (m)	Recovery (%)	Date (2015)	Time on deck UTC (h)
41F	320.20	324.90	4.7	4.71	4.71	320.20	324.91	100	18 Sep	0410
42F	324.90	329.60	4.7	4.94	4.94	324.90	329.84	105	18 Sep	0550
43F	329.60	334.30	4.7	4.90	4.90	329.60	334.50	104	18 Sep	0615
44F	334.30	339.00	4.7	4.84	4.84	334.30	339.14	103	18 Sep	0635
45F	339.00	343.70	4.7	5.05	4.84	339.00	344.05	107	18 Sep	0700
46F	343.70	348.40	4.7	4.76	4.76	343.70	348.46	101	18 Sep	0725
47F	348.40	352.80	4.4	4.40	4.40	348.40	352.80	100	18 Sep	0755

34X through 60X to a final depth of 530.0 m DSF. Hole U1463B reached final depth at 0005 h on 15 September. The APC system advanced 271.2 m and recovered 267.73 m of core, whereas the HLAPC system recovered 13.30 m from 13.2 m cored. The XCB system was used to core 245.6 m with 117.97 m of recovered material. Overall, recovery for IODP Hole U1463B was 75.3%.

At the conclusion of coring, the hole was circulated with high-viscosity mud to clean the hole of cuttings and a go-devil was pumped through the drill string to open the lockable float valve. The drill string was pulled back to 358.1 m DSF and the upper part of the hole was displaced with heavy mud in preparation for downhole logging operations. The drill string was then pulled back further to logging depth (82.1 m DSF) and the first logging tool string (triple combo) was assembled. The triple combo tool string contained the following tools: magnetic susceptibility sonde, Hostile Environment Natural Gamma Ray Sonde (HNGS), Hostile Environment Litho-Density Tool, Enhanced Digital Telemetry Cartridge (EDTC), and logging equipment head-q tension (LEH-QT). The triple combo tool string was deployed at 0710 h on 15 September. After the tool string exited the drill pipe, the active heave compensator was turned on. A downlog was performed from just above seafloor to a bridge at 454.7 m DSF. The hole was logged up to ~350 m WSF, run back to the bottom, and a second uplog was made from 454.7 to 82.1 m WSF (end of the pipe). The tools were at the surface at 0930 h and were disassembled. The next tool string, the VSI, was then readied. A caliper extension was added to the tool because the triple combo deployment suggested a wide borehole diameter (>17 inches). The protected species watch was started at 1000 h, and the tool string was deployed at 1130 h and reached 446.7 m WSF, where it encountered a bridge. Whales were sighted continuously until 1315 h, but after 1 h of observations without any further sightings, the seismic source began a soft ramp-up and the VSI experiment began at 1445 h. One station was completed at 428.7 m WSF before another whale sighting was reported. At 1500 h, we decided to cancel the VSI and the tool string was on the rig floor at 1530 h. After rigging down the VSI, the FMS-sonic tool string was assembled with the following tools: FMS, Dipole Sonic Imager, HNGS, EDTC, and LEH-QT. At 1705 h, the FMS-sonic was deployed and two passes were made over the total depth of the open borehole (445.7–82.1 m WSF). The tool string was pulled back to the surface at 2030 h. At 2200 h on 15 September, all logging tools were dissembled and the logging wireline was secured. The drill string cleared the seafloor at 2230 h, ending Hole U1463B. The total time spent on Hole U1463B was 74.0 h (3.1 days).

Hole U1463C

After offsetting the vessel 20 m south, operations began for Hole U1463C (18°57.9295′S, 117°37.4336′E). A nonmagnetic APC core barrel was dressed with a core liner in preparation for Hole U1463C, which was started at 0435 h on 16 September 2015. The desired depth of the mudline core was corrected for tidal height and recovery offset by the stratigraphic correlators. Based on the recovery of the mudline core (4.11 m), the seafloor depth was calculated to be 144.8 mbsl. Coring continued through Core 356-U1463C-31H to 280.7 m DSF; all of these APC cores were oriented with the Icefield MI-5 orientation tool. In situ temperature measurements were made with the advanced piston corer temperature tool (APCT-3) on Cores 4H, 7H, 10H, 13H, 16H, and 20H. We switched to the HLAPC system after recovering Core 31H and recovered Cores 32F through 61F to 392.2 m DSF. A total of 280.7 m was cored with the APC system with 285.40 m recovered, and 111.5 m was cored with the HLAPC system with 111.94 m recovered, so the overall recovery for Hole U1463C was 101.3%. Hole U1463C ended at 1640 h on 17 September. The total time spent on Hole U1463C was 42.25 h (1.8 days).

Hole U1463D

The vessel was offset 20 m west of Hole U1463C, and preparations were made to start Hole U1463D (18°57.9285′S, 117°37.4216′E). A nonmagnetic APC core barrel was dressed with a core liner, and Hole U1463D was started at 1740 h on 17 September 2015. The shoot depth for the mudline core was corrected for tidal height and offset to maximize recovery for the generation of a splice by the stratigraphic correlators. Based on the recovery of the mudline core (1.40 m), the seafloor depth was calculated to be 144.5 mbsl. Coring continued through the recovery of Core 356-U1463D-32H to 288.4 m DSF before we switched to the HLAPC system. We recovered Cores 33F through 47F to 352.8 m DSF. We advanced 288.4 m with the APC system and recovered 282.16 m of core. The HLAPC system was used to core 64.4 m and recovered 64.45 m of material. The overall recovery for Hole U1463D was 98.2%. The total time spent on Hole U1463D was 25.75 h (1.1 days). After coring was completed, the drill string was pulled back to the surface, clearing the seafloor at 1750 h. The seafloor positioning beacon was recovered at 1810 h on 18 September. After securing the rig floor, the thrusters and hydrophones were pulled and secured, ending Site U1463. The total time spent on Site U1463 was 147.0 h (6.1 days).

Lithostratigraphy

Lithostratigraphy of Site U1463 is divided into five units and two subunits (Table **T3**). The lithostratigraphic units and their boundaries are defined by changes in lithology (identified by visual core description and smear slide observations), physical properties, color reflectance (L*, a*, and b*), petrographic section analyses, X-ray diffraction (XRD), and seismic data. The lithologic descriptions are

Table T3. Lithostratigraphic unit summary, Site U1463. Subunits not present in Hole U1463D. **Download table in .csv format.**

Lith. unit	Hole U1463A				Hole U1463B			
	Core, section, interval (cm)		Depth CSF-A (m)		Core, section, interval (cm)		Depth CSF-A (m)	
	Top	Bottom	Top	Bottom	Top	Bottom	Top	Bottom
	356-U1463A-	356-U1463A-			356-U1463B-	356-U1463B-		
I	2X-1, 0	2X-3, 128	9.70	13.98	1H-1, 0	2H-3, 81	0.00	11.71
II	2X-3, 128	2X-CC, 25	13.98	18.29	2H-3, 81	13H-1, 0	11.71	112.40
III					13H-1, 0	47X-1, 0	112.40	399.10
IIIa					13H-1, 0	36X-3, 71	112.40	305.81
IIIb					36X-3, 71	47X-1, 0	305.81	399.10
IV					47X-1, 0	50X-1, 0	399.10	428.20
V					50X-1, 0	60X-CC, 5	428.20	525.25

Unit	Hole U1463C				Hole U1463D			
	Core, section, interval (cm)		Depth CSF-A (m)		Core, section, interval (cm)		Depth CSF-A (m)	
	Top	Bottom	Top	Bottom	Top	Bottom	Top	Bottom
	356-U1463C-	356-U1463C-			356-U1463D-	356-U1463D-		
I	1H-1, 0	3H-1, 71	0.00	14.31	1H-1, 0	3H-4, 0	0.00	15.40
II	3H-1, 71	13H-5, 0	14.31	112.11	3H-4, 0	14H-1, 90	15.40	114.30
III	13H-5, 0	61F-CC, 25	112.11	392.49	14H-1, 90	47F-3, 140	114.30	352.80
IIIa	13H-5, 0	38F-1, 71	112.11	307.11				
IIIb	38F-1, 71	61F-CC, 25	307.11	392.49				
IV								
V								

based on sediments recovered from Holes U1463A (9.70–18.29 m core depth below seafloor [CSF-A]), U1463B (0.00–525.25 m CSF-A), U1463C (0.00–392.49 m CSF-A), and U1463D (0.00–352.80 m CSF-A). Most smear slide data are from Hole U1463B, and additional smear slides were taken in Hole U1463C to refine unit boundaries. The holes were aligned based on drilling depth and the correlation of lithologic boundaries (Figure **F4**). All thin section samples are listed in Table **T4** and XRD analyses are summarized in Table **T5**.

Unit I

Intervals: 356-U1463A-2X-1, 0 cm, through 2X-3, 128 cm; 356-U1463B-1H-1, 0 cm, through 2H-3, 81 cm; 356-U1463C-1H-1, 0 cm, through 3H-1, 71 cm; 356-U1463D-1H-1, 0 cm, through 3H-4, 0 cm
Depths: Hole U1463A = 9.70–13.98 m CSF-A (4.28 m thick); Hole U1463B = 0.00–11.71 m CSF-A (11.71 m thick); Hole U1463C = 0.00–14.31 m CSF-A (14.31 m thick); Hole U1463D = 0.00–15.40 m CSF-A (15.40 m thick)
Age: recent–Middle Pleistocene
Lithology: unlithified wackestone and mudstone with peloids
Core quality: drilling disturbance is slight and primarily soupiness and/or minimal fracturing

Unit I is defined by a relatively high abundance of peloids visible in smear slides. Peloid abundance declines markedly at the bottom of Unit I, although peloids continue in Unit II as a minor constituent. Unit I is primarily unlithified creamy-gray to light greenish-gray wackestone and mudstone. Macrofossils are abundant and diverse and include bivalves, gastropods, bryozoans, serpulids, echinoderms, pteropods, scaphopods, and small benthic foraminifers. Bioturbation is moderate but intermittent. There are a few gradational, bioturbated, and erosive contact surfaces. The unit represents a neritic to hemipelagic environment.

Unit I has relatively high calcium carbonate content (~87 wt%), very low quartz content, low natural gamma radiation (NGR), and relatively high grain density (see **Physical properties**; Figure **F5**).

Smear slides

The microfossil assemblage in the uppermost interval (0–30 cm) of Unit I differs markedly from the rest of the unit and is dominated by abundant pteropod shells and diverse planktonic and miliolid benthic foraminifers in a fine micrite matrix. Below this interval, the rest of Unit I is defined by the abundance of small- to medium-sized (75–250 µm) peloids in a fine micrite matrix (Figure **F6A**). The microfossils are mainly shell fragments and diverse planktonic and benthic foraminifers, with fragments of echinoderm spines and sponge spicules as minor components. Enigmatic microfossils include holothurian and ascidian spicules and rare pteropod fragments. Nannofossils are present in all samples, but abundances vary greatly throughout the unit. Microfossil preservation is exceptional with no sparitic cementation and only very rare glauconitization. Detrital glauconite is rare, and authigenic glauconite occurs only at the base of the unit. Silt-sized quartz and mica grains vary in abundance from accessory to very minor components, indicating low but continuous siliciclastic input at Site U1463 during the deposition of Unit I.

Unit II

Intervals: 356-U1463A-2X-3, 128 cm, through 2X-CC, 25 cm; 356-U1463B-2H-3, 81 cm, through 13H-1, 0 cm; 356-U1463C-3H-1, 71 cm, through 13H-5, 0 cm; 356-U1463D-3H-4, 0 cm, through 14H-1, 90 cm
Depths: Hole U1463A = 13.98–18.29 m CSF-A (4.31 m thick); Hole U1463B = 11.71–112.40 m CSF-A (100.69 m thick); Hole U1463C = 14.31–112.11 m CSF-A (97.80 m thick); Hole U1463D = 15.40–114.30 m CSF-A (98.90 m thick)
Age: Middle–early Pleistocene

Figure F4. Lithostratigraphic summary, Holes U1463A–U1463D. See Figure **F7** in the Expedition 356 methods chapter (Gallagher et al., 2017a) for lithology key.

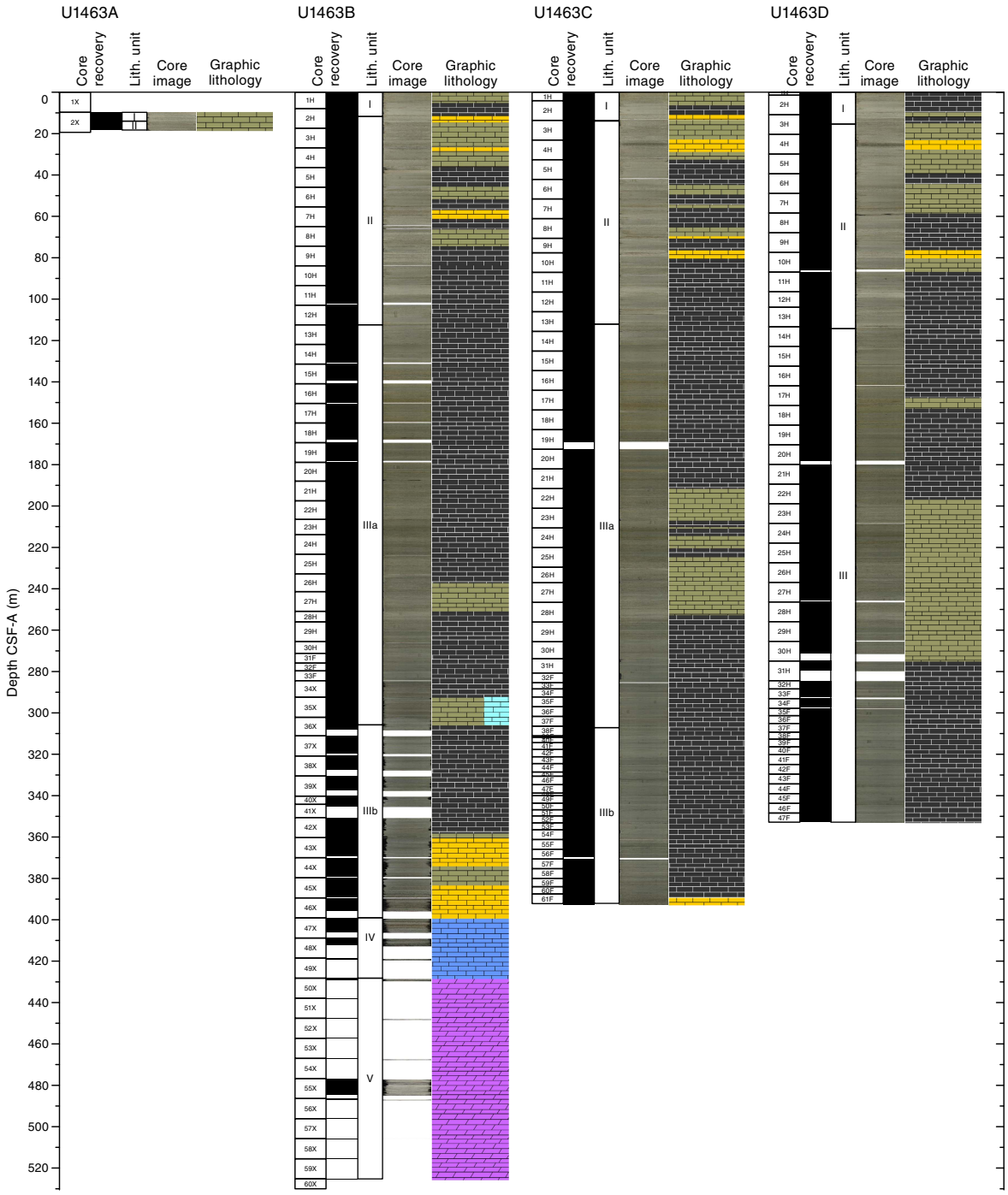

Lithology: unlithified; alternating wackestone, packstone, and mudstone intervals

Core quality: rare but severe drilling disturbance includes soupiness, fall-in, mixing, and/or damaged core liners

Unit II consists of alternating unlithified wackestone, packstone, and mudstone intervals. The packstones contain poorly sorted fine to coarse sand–sized grains, whereas the wackestone and mudstone intervals contain fine sand– to silt-sized grains. The color of Unit II alternates subtly between (light) greenish gray and creamy-gray intervals that are not always associated with lithologic changes. In Hole U1463B, the creamy-gray intervals are primarily packstones, whereas in Holes U1463C and U1463D, all three lithologies (packstone, wackestone, and mudstone) have both (light) greenish-gray and creamy-gray colors. In all holes, macrofossils are less diverse and less abundant (or absent) in mudstone intervals. In wackestone and packstone intervals, macrofossils include pteropods, scaphopods, echinoderms, bivalves, solitary corals, gastropods, bryozoans, serpulids, barnacles, and small benthic foraminifers. Bioturbation occurs occasionally in Unit II with slight to moderate intensity and is not associated with a particular lithology. Sedimentary features are minimal, consisting of occasional contact surfaces (e.g., gradational, sharp, and bioturbated). The packstones contain occasional

concretions. A thin grainstone interval in the lower part of Unit II (74.40–74.58 m CSF-A in Hole U1463B, 70.6–70.88 m CSF-A in Hole U1463C, and 78.1–78.34 m CSF-A in Hole U1463D) has abundant fragments of bivalves, gastropods, and large benthic foraminifers (LBFs). Solution cavities are present in this interval in Hole U1463B. The Unit II facies is predominantly hemipelagic.

The lithologic change between Units I and II is most evident as increasing NGR and decreasing grain density (see **Physical properties**). Calcium carbonate content is relatively high (and similar to Unit I) but decreases toward the boundary with Unit III; quartz content is generally low but increases toward the base (Figure **F5**).

Smear slides

The top of Unit II is defined by the absence of medium-sized (150–250 µm) peloids, but smaller peloids (<150 µm) are accessory components, especially at the top of Unit II. The fine fraction varies between coarse (~10–20 µm) and fine (clay sized) micrite and contains variable but generally minor amounts of clay minerals. The fossil assemblage is diverse (Figure **F6B**), but abundance decreases in the lower part of the unit. The dominant fossils are planktonic foraminifers with fewer benthic foraminifers. Well-preserved shell fragments are common but decrease in abundance deeper than 40 m CSF-A (Sample 356-U1463B-5H-5, 71 cm). Isolated, small, prismatine bivalve shells occur in the uppermost part of the unit. Echinoderm spines and sponge spicules are minor components and are less common than in Unit I. Ascidian spicules are rare with progressively poorer preservation as depth increases. Nannofossils are common to abundant in the fine fraction. Overall preservation of microfossils is very good, with only slight sparite overgrowth throughout the unit. There is slight glauconitization of foraminiferal tests in several samples from the lower part of the unit. Detrital glauconite is often present as fine sand–sized grains. Silt-sized quartz and other fine-grained siliciclastics are minor to common accessory components, with rare occurrences of larger sand-sized grains throughout the unit.

Table T4. Thin section samples, Site U1463. All thin sections are from working-half sections. **Download table in .csv format.**

Lith. unit	Core, section interval (cm)	Top depth CSF-A(m)	Bottom depth CSF-A (m)
	356-U1463B-		
II	9H-1, 0–3	74.40	74.43
IIIa	31F-1, 0–3	271.20	271.23
IIIb	42X-5, 19–21	356.79	356.81
IIIb	45X-6, 70–73	386.92	386.95
IIIb	45X-7, 9–11	387.81	387.83
IIIb	46X-2, 75–78	391.60	391.63
IIIb	46X-3, 29–32	392.60	392.63
IIIb	46X-4, 66–69	394.44	394.47
IV	47X-3, 87–90	402.91	402.94
V	50X-CC, 14–17	429.15	429.18
V	54X-CC, 23–26	467.23	467.26
V	55X-1, 101–104	477.71	477.74
V	55X-2, 80–83	479.00	479.03
V	55X-4, 75–78	481.84	481.87
V	55X-5, 21–24	482.80	482.83
V	55X-6, 21–24	483.79	483.82

Thin sections

The only thin section from Unit II (Table **T4**; Figure **F7A**) is foraminiferal packstone with fine to medium sand–sized planktonic and small benthic foraminifers, with lower abundances of bivalve, bryozoan, and echinoderm fragments.

XRD

The two samples from Unit II (Table **T5**) are dominated by low-Mg calcite (54%) with quartz (18%), dolomite (16%), and aragonite (11%) as minor components. Kaolinite is present in only one sample (356-U1463B-6H-5, 72 cm), whereas illite is present in both samples. The average Mg content of the dolomite is 46%.

Unit III

Intervals: 356-U1463B-13H-1, 0 cm, through 47X-1, 0 cm; 356-U1463C-13H-5, 0 cm, through 61F-CC, 25 cm; 356-U1463D-14H-1, 90 cm, through 47F-3, 140 cm
Depths: Hole U1463B = 112.40–399.10 m CSF-A (286.7 m thick); Hole U1463C = 112.11–392.49 m CSF-A (280.38 m thick); Hole U1463D = 114.30–352.80 m CSF-A (238.5 m thick)
Age: early Pleistocene–late Miocene
Lithology: homogeneous fine-grained mudstone with subordinate wackestone and packstone intervals and increasing lithification with depth
Core quality: slight to severe drilling disturbance includes soupiness, mixing, fragmentation, and biscuits

The top of Unit III marks the end of the creamy-gray intervals in the alternating lithologies of Unit II. Instead, Unit III is composed predominantly of homogeneous mudstone containing fine sand–sized grains. The mudstone contains intervals of wackestone with very fine sand– to silt-sized grains. In the lowermost part of Hole

Table T5. Semiquantitative XRD analysis of dominant mineral phases, Site U1463. LMC = low-Mg calcite, HMC = high-Mg calcite. $MgCO_3$ of dolomite was calculated based on the d-value of the [104] peak (Lumsden, 1979). **Download table in .csv format.**

Lith. unit	Core, section, interval (cm)	Depth CSF-A (m)	Clay mineral group	Relative (%)								Mg content (mol%)
				Celestite	Anhydrite	Quartz	Aragonite	LMC	HMC	Dolomite	Gypsum	
	356-U1463B-											
II	6H-5, 72	52.62	Illite/Kaolinite	0	0	16	19	54	0	11	0	46
II	10H-3, 70	87.60	Illite	0	0	20	4	55	0	21	0	46
IIIa	19H-3, 70	173.10	Illite/Kaolinite	0	0	29	6	57	0	8	0	43
IIIb	40X-2, 71	342.41	Illite/Kaolinite	3	0	38	2	54	0	3	0	
IIIb	46X-2, 73	391.58	Illite/Kaolinite	0	0	22	0	61	0	17	0	44
IV	47X-3, 56	402.60	Illite/Kaolinite	0	0	2	0	70	0	28	0	45
V	55X-2, 81	479.01		0	0	0	0	0	0	44	56	49
V	56X-CC, 19	486.59		0	0	0	0	0	0	52	48	50

Figure F5. Summary of synthetized correlation of lithostratigraphy at Site U1463 with data from smear slides (peloids, quartz content, and grain size), geochemistry (calcium carbonate content), physical properties (MS, NGR, grain density, *P*-wave velocity, and porosity), and biostratigraphy. Data from Holes U1463A and U1463B are plotted for MS (blue) and NGR (orange). See Figure **F7** in the Expedition 356 methods chapter (Gallagher et al., 2017a) for lithology key. WRMSL = Whole-Round Multisensor Logger. cps = counts per second.

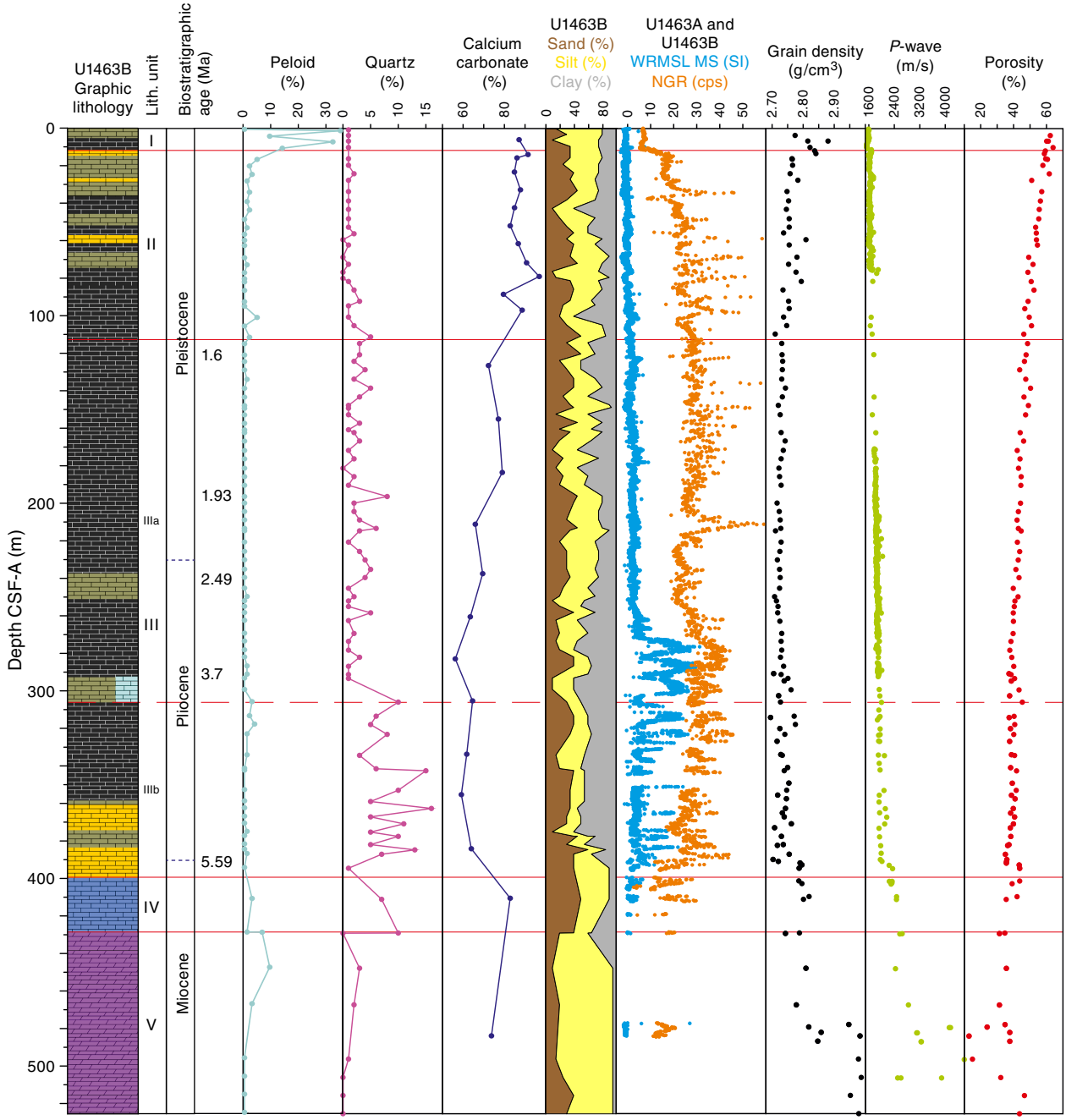

U1463B, wackestones alternate with packstones. Lithification increases progressively with depth in Hole U1463B. Macrofossils are uncommon in Unit III, and both diversity and abundance decrease with depth. Small benthic foraminifers and bivalve fragments are the most common bioclasts; less common constituents include fragments of gastropods, bryozoans, echinoderm spines, crustaceans, scaphopods, barnacles, and unidentified tube structures. Unit III is divided into two subunits that are macroscopically very similar; the top of Subunit IIIb is defined by an abrupt downhole increase in quartz content (seen in smear slides). Unit III is also present in Hole U1463D and shows similar variations in core images as Holes U1463B and U1463C (Figure **F4**). However, Unit III was not divided into subunits in Hole U1463D because smear slides were not taken from this hole. As a result, the quartz content, used to define subunits, was not estimated. The Unit III facies is predominantly hemipelagic.

Unit III is characterized by overall decreasing calcium carbonate content (see **Geochemistry**), relatively high NGR, and gradually increasing *P*-wave velocity (Figure **F5**). Deeper than about 290 m CSF-A, both magnetic susceptibility (MS) and NGR values are

Figure F6. Representative smear slide photomicrographs of units, Hole U1463B. A. Unit I: sediment rich in small peloids (p) with abundant miliolid benthic and planktonic foraminifers (f), well-preserved mollusk shell fragments (m), a single siliceous sponge spicule (s); note very fine-grained authigenic glauconite (black arrow) and mica (white arrows) (7H-2, 71 cm). B. Unit II: dominant planktonic and benthic foraminifers (f) with fewer well-preserved shell fragments (m); quartz (q), ascidian spicules (blue arrow), and mica (white arrow) are common accessory to minor components; note small authigenic glauconite grains, often in aggregates with clay-sized sediment (black arrows) (3H-2, 71 cm). C. Subunit IIIa: benthic and planktonic foraminifers (f) and shell fragments (m) in a coarse (fine silt sized) matrix; accessory echinoderm spine (e) and sponge spicule (s) fragments; note common quartz (q), mica (white arrows), and accessory authigenic glauconite (black arrows) (17H-2, 71 cm). D. Cross-polarized light (XPL) image of C, illustrating silt-sized quartz (q) in a carbonate matrix with sand-sized bioclasts. E. Subunit IIIb: benthic and planktonic foraminifers (f) with poorly preserved shell fragments (m); note increased siliciclastic components dominated by quartz (q) and feldspar (fsp), with mica (white arrow) and rare chlorite (cl); authigenic glauconite and glauconitized foraminifers are also common (black arrows) (40X-2, 71 cm). F. Unit V: large anhydrite (a) grains in a dolomite matrix (white arrows) (59X-CC); XPL.

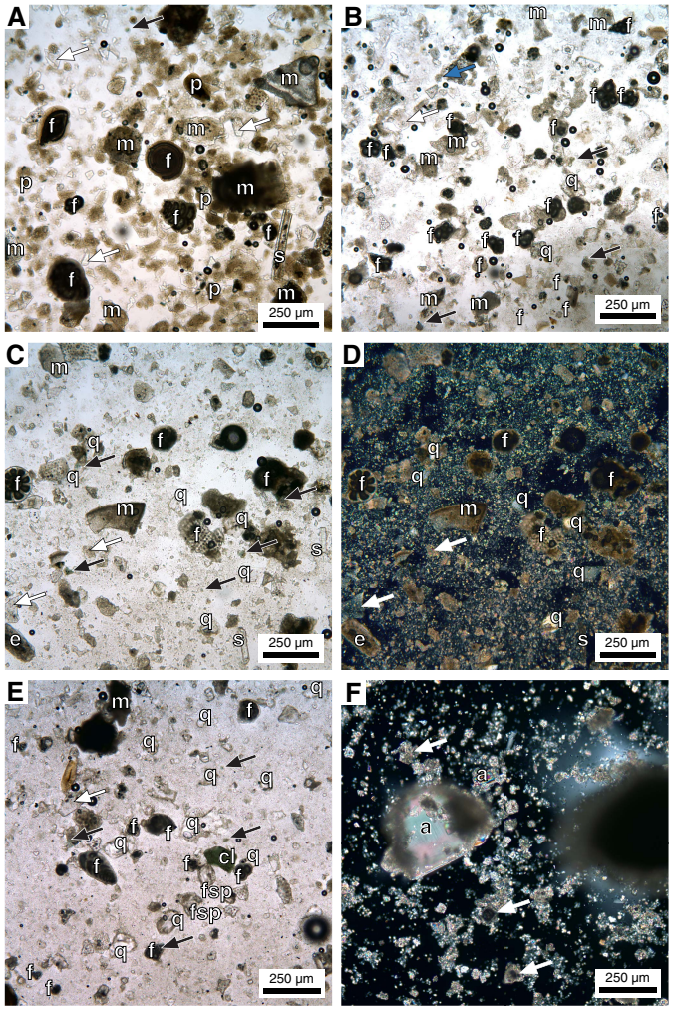

highly variable, whereas *P*-wave velocity and porosity values remain very stable.

Subunit IIIa

Intervals: 356-U1463B-13H-1, 0 cm, through 36X-3, 71 cm; 356-U1463C-13H-5, 0 cm, through 38F-1, 71 cm

Figure F7. Representative thin section photomicrographs, Hole U1463B. A. Unit II: skeletal packstone with abundant medium sand–sized benthic and planktonic foraminifers (f) and few echinoderm fragments (e) (9H-1); XPL. B. Subunit IIIa: skeletal packstone with abundant planktonic and benthic foraminifers (f) and pore space filled by large bluish to grayish single celestite crystals (arrows) (31F-1); XPL. C. Subunit IIIb: foraminiferal grainstone with abundant benthic foraminifers *Amphistegina* (a) and *Cibicidoides* (c) and rare echinoderm fragments (e); planktonic foraminifers are rare; note abundant greenish glauconitic and brownish iron oxide staining and high interparticle porosity (46X-3). D. Unit IV: foraminiferal packstone with abundant LBFs and rare planktonic foraminifers (f), common echinoderm fragments (e), and abundant glauconitization (white arrows) as well as brownish iron oxide staining (47X-3). E. Unit V: skeletal packstone with abundant small benthic foraminifers (f) and echinoderm fragments, and euhedral dolomite (d); pore space is cemented mainly with calcite and partly with celestite (blue arrows) (54X-CC). F. Unit V: dolomitic limestone with intensive anhydrite (a) replacement, micrite (m), dolomite (d) and celestite (white arrow) (55X-6).

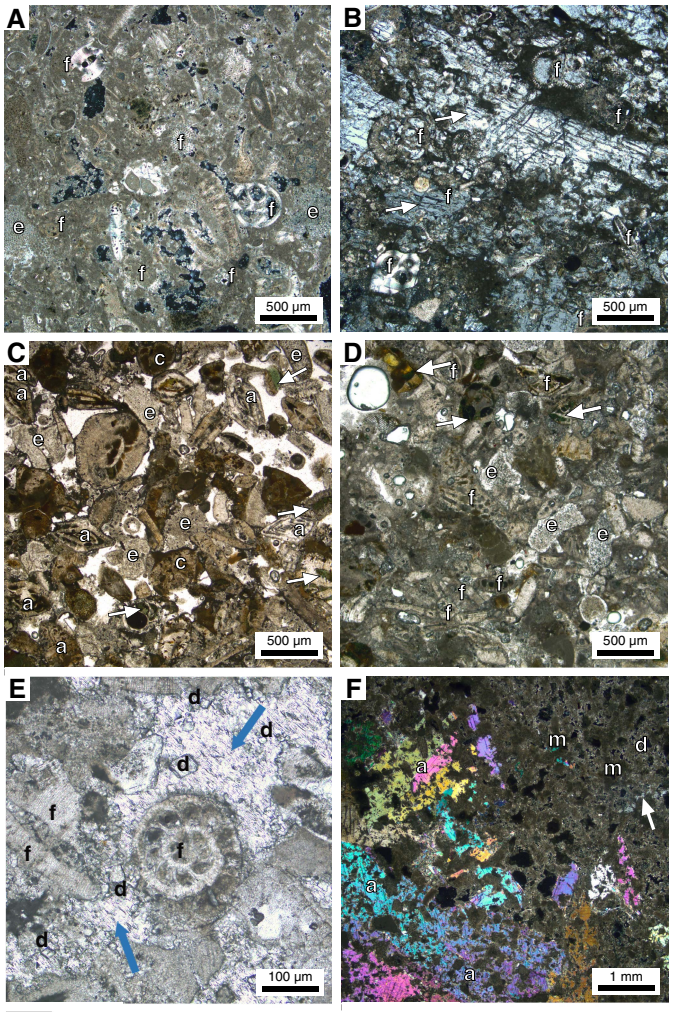

Depths: Hole U1463B = 112.40–305.81 m CSF-A (193.41 m thick); Hole U1463C = 112.11–307.11 m CSF-A (195.00 m thick)
Age: early Pleistocene–early Miocene
Lithology: homogeneous fine-grained mudstone and subordinate wackestone
Core quality: slight to severe drilling disturbance includes soupiness, mixing, fragmentation, and biscuits

Subunit IIIa is composed predominantly of well-sorted homogeneous mudstone with wackestone intervals. Its appearance changes from lighter to generally darker colors with increasing depth. Bio-

turbation begins in the darker interval and generally increases in intensity toward the base of the subunit. In all holes, celestite (and possibly gypsum) occurs as concretions and as crystals just above and below an erosive and/or sharp contact surface (~250 m CSF-A in Hole U1463B, ~180 m CSF-A in Hole U1463C, and ~177 m CSF-A in Hole U1463D). Below this contact, disseminated pyrite grains and nodules gradually become more abundant. There are occasional sedimentary structures, including parallel laminations and bioturbated, wavy, sharp, scoured, and gradational contacts.

Smear slides

The top of Subunit IIIa is marked by a continued increase (from Unit II) of coarse silt– to fine sand–sized quartz grains in an otherwise bioclastic sediment. The abundance of sand-sized grains decreases downhole with increasingly clay-rich sediments toward the base of the unit, although coarser sand-rich layers occur throughout Subunit IIIa. Dominant microfossils are planktonic and benthic foraminifers with common to abundant shell fragments that have moderate to poor preservation. Echinoderm spine fragments and sponge spicules are accessories throughout the subunit (Figure **F6C–F6D**). Nannofossils are common in the upper part of the subunit but decrease sharply at ~200 m CSF-A and then gradually increase toward the base of the subunit, coinciding with the gradual increase in clay-sized material (Figure **F5**). Foraminifers decrease in abundance over the same interval. Abundance of shell fragments is variable without any trend throughout the subunit. Microfossil preservation is generally moderate to occasionally poor with sparite overgrowth on many foraminifers. Shell fragments are usually heavily altered, and aragonite ultrastuctures are rarely preserved. Authigenic glauconite and glauconitized microfossils are more abundant than in Unit II, and this increase is accompanied by increased abundances of framboidal pyrite, fine crystalline euhedral dolomite, and anhydrite. The total siliciclastic content is greater than that of Unit II, particularly medium silt–sized mica. Quartz content is also higher than in Unit II (an increase in quartz content is the primary marker for the top of Subunit IIIa), and feldspar and rare heavy mineral grains (e.g., zircon and apatite) are accessories throughout Subunit IIIa.

Thin sections

The only thin section (Table **T4**; Figure **F7B**) prepared from Subunit IIIa (356-U1463B-31F-1, 0–3 cm) is a skeletal wackestone to packstone with foraminifers as the most abundant bioclastic component together with some celestite replacement.

XRD

The only XRD sample from Subunit IIIa (Table **T5**) is dominated by low-Mg calcite (57%) and quartz (29%) with nearly equal amounts of aragonite and dolomite (6% and 8%, respectively). Illite and kaolinite are present. The Mg content of the dolomite is 43%.

Subunit IIIb

Intervals: 356-U1463B-36X-3, 71 cm, through 47X-1, 0 cm; 356-U1463C-38F-1, 71 cm, through 61F-CC, 25 cm
Depths: Hole U1463B = 305.81–399.10 m CSF-A (93.29 m thick); Hole U1463C = 307.11–392.49 m CSF-A (85.38 m thick)
Age: early–late Miocene
Lithology: homogeneous fine-grained mudstone and subordinate packstone and wackestone
Core quality: slight to severe drilling disturbance includes soupiness, mixing, fragmentation, and biscuits

Subunit IIIb consists predominantly of homogeneous fine-grained mudstone with subordinate packstone and wackestone. The top is defined by an abrupt downhole increase in quartz content in smear slides. Macroscopic core descriptions do not indicate a distinctive lithologic change at this depth. The lower part of Subunit IIIb is characterized by coarsening grain size with increasing depth and by alternating lithologies. The lower interval consists of alternating lithified packstones and wackestones in Hole U1463B and alternating wackestones and mudstones in Hole U1463C. The packstones are dark greenish gray and contain sand-sized grains, the wackestones are light greenish gray, and the mudstones are olive-gray. It is possible that these lithologic differences between Hole U1463B and U1463C cores are related to the effects of XCB versus HLAPC coring (see **Physical properties**). Bioturbation is common to complete throughout this lower interval, and pyrite is present as disseminated grains and as nodules. Sparse macrofossils include small benthic foraminifers, bivalves, bryozoans, and echinoderm spines. Intermittent sedimentary features occur as parallel laminations, normal grading, and sharp, gradational, and bioturbated contact surfaces. There is evidence for soft-sediment deformation (e.g., slump folds) in Hole U1463B at 350.6–351.6 m CSF-A.

Smear slides

In Subunit IIIb, total siliciclastic content increases markedly and quartz becomes a common component of the sediment. The common occurrence of large (>200 µm) quartz grains clearly distinguishes Subunit IIIb from Subunit IIIa (Figure **F6E**). Overall bioclastic content is higher in the uppermost part of Subunit IIIb but gradually decreases in the lower part of the subunit. The microfossil assemblage of Subunit IIIb shows a distinct shift from planktonic to benthic foraminifers and a marked decrease in shell fragments relative to Subunit IIIa. Echinoderm spine fragments are a common but minor component. Fragments of sponge spicules are rare, and ascidian spicules are absent. Sand-sized bioclasts are generally more abundant in Subunit IIIb than in Subunit IIIa. Nannofossils are abundant throughout the upper part, often dominating fine silt– to clay-sized fractions. Microfossil preservation is moderately good to very good in Subunit IIIb with rare occurrences of heavy alteration by sparite overgrowth. Glauconitization is common but usually only in some foraminiferal tests. There is slightly less authigenic glauconite than in Subunit IIIa, but detrital glauconite grains are generally larger (fine sand sized) and more common. Siliciclastic grains are common throughout the subunit, but total abundance varies markedly. Quartz is the dominant siliciclastic mineral. Mica and feldspar are common, and heavy minerals (e.g., zircon and apatite) are common accessories throughout the subunit.

Thin sections

Six thin sections (Table **T4**; Figure **F7C**) prepared for Subunit IIIb consist of pyrite- and glauconite-rich foraminiferal packstones to grainstones. Large-sized benthic foraminifers (e.g., *Amphistegina* and *Cibicidoides*) dominate bioclastic components, and planktonic foraminifers, mollusks, and echinoderm fragments are rare to absent. Silt-sized angular quartz grains are present and increase in abundance downhole.

XRD

The two XRD samples from Subunit IIIb (Table **T5**) are dominated by low-Mg calcite (average = 57%) and quartz (average = 30%). Dolomite is present in small amounts (3%) in the upper sam-

ple (from 342.41 m CSF-A) but increases to 17% toward the base of the unit (391.58 m CSF-A), where the average Mg content of the dolomite is 44%. Aragonite (2%) and celestite (3%) are present at 342.41 m CSF-A.

Unit IV

Interval: 356-U1463B-47X-1, 0 cm, through 50X-1, 0 cm
Depth: Hole U1463B = 399.10–428.20 m CSF-A (29.10 m thick)
Age: Miocene
Lithology: partially lithified to lithified grainstone, slightly dolomitized
Core quality: slight drilling disturbance includes soupiness, fragmentation, and/or biscuits

Unit IV consists of a slightly dolomitic grainstone interval in Hole U1463B that grades downhole from light greenish gray to dark greenish gray, contains coarse to medium sand–sized grains composed mainly of bioclasts (e.g., bivalves, bryozoans, and small benthic foraminifers), and has relatively high amounts of pyrite. Bioturbation is less intense than in Unit III. Macrofossil fragments, mainly bivalves, bryozoans, and small benthic foraminifers, are common to locally abundant. The grainstone has various sedimentary features, including normal grading, parallel and wavy laminations, medium bedding, intraclasts, and numerous contact surfaces (e.g., wavy, scoured, gradational, and sharp). There is some dolomitization and less quartz than in Unit III. The facies is interpreted as neritic.

Unit IV has low MS and NGR values relative to the base of Unit III (Figure **F5**), relatively high grain density and *P*-wave velocity, and slightly increased porosity.

Smear slides

Only one smear slide was prepared from Unit IV because the sediment was generally coarse grained and lithified. The composition was similar to that of Subunit IIIb but with more poorly preserved coarse (medium sand sized) shell fragments and much lower quartz content.

Thin sections

The only thin section from Unit IV (Table **T4**; Figure **F7D**) is foraminiferal packstone to grainstone, rich in glauconite and iron oxide/hydroxide, that is similar to the lower part of Unit III. The dominant bioclasts are LBFs (*Amphistegina*) and echinoderm fragments, whereas planktonic foraminifers are rare.

XRD

The only XRD sample taken in Unit IV contains 28% dolomite, 70% calcite, and has a low quartz content (2%) compared to Unit III. The average Mg content of the dolomite is 45%.

Unit V

Interval: 356-U1463B-50X-1, 0 cm, through 60X-CC, 5 cm
Depth: Hole U1463B = 428.20–525.25 m CSF-A (97.05 m thick)
Age: Miocene
Lithology: dolostone characterized by anhydrite nodules and dissolution features
Core quality: drilling disturbance is slight to severe fragmentation

Unit V consists primarily of creamy-gray to light brown dolostone with sand-sized grains. There are many anhydrite nodules and dissolution features. Colors vary between light gray and brown. Sand-sized grains of pyrite and/or glauconite occur both in patches and as disseminated grains throughout the matrix. Bioturbation and macrofossils are locally common, and the main bioclasts are bivalves with occasional bryozoans and foraminifers. This unit is interpreted as neritic.

Because of poor recovery, Unit V sediments cannot be correlated with the MS and NGR data (Figure **F5**). Moisture and density (MAD) and *P*-wave data show that Unit V has relatively low porosity, high grain density, and high *P*-wave velocity (see **Physical properties**).

Smear slides

Unit V is characterized by common anhydrite and dolomite (Figure **F6F**) and a sharp increase in lithification relative to Unit IV. Smear slides were prepared only when sufficient amounts of sediment could be scraped from the core. Microfossil preservation and overall abundance both decrease relative to Unit IV, reflecting the marked change in mineral composition. Microfossils are generally rare to absent, reflecting an increase in dolomitization and anhydrite cementation. Celestite is a rare accessory authigenic mineral. When present, the dominant microfossils are moderately to very poorly preserved benthic and planktonic foraminifers with lesser amounts of poorly preserved shell fragments. Echinoderm spines are common but not abundant. Nannofossils are rare in the upper part of Unit V, decrease rapidly with depth, and are absent in the lowermost heavily dolomitized interval of the unit. The siliciclastic content is low, which may reflect a sampling bias caused by preferential sampling of softer dolomite-rich sediment.

Thin sections

Seven thin sections from Unit V (Table **T4**; Figure **F7E–F7F**) display a transition from calcitic skeletal packstones to skeletal packstones and grainstones with dolomite and gypsum/anhydrite cements. Dominant bioclasts are benthic foraminifers with rare bivalve and echinoderm fragments. Fine-grained dolomitic limestones associated with evaporitic cements in Core 356-U1463B-55X may indicate early diagenetic evaporitic conditions.

XRD

The two samples (Table **T5**) from Unit V consist of gypsum (52%) and dolomite (48%). The average Mg content of the dolomite is 50%.

Biostratigraphy and micropaleontology

Core catcher (CC) samples from Site U1463 were processed at 20 m resolution. Nannofossil analyses were done at 10 m resolution in selected intervals to better constrain biostratigraphic datums between Holes U1463B and U1463C, and additional benthic foraminiferal samples were taken from selected intervals when specific assemblages were absent from core catcher samples.

Site U1463 yielded a complete stratigraphic succession from the late Miocene to early Pleistocene, with abundant and well-preserved nannofossils (Figure **F8**). The Pliocene/Pleistocene boundary (2.58 Ma; within NN16) is between 240.7 and 265.87 m CSF-A, and the Miocene/Pliocene boundary (5.33 Ma; within Biozone NN12) is between 345 and 379 m CSF-A. The abundance and preservation of planktonic foraminifers at Site U1463 was the best among all investigated sites so far during Expedition 356. Moderate to very good preservation was encountered in the entire Pleistocene to Pliocene succession with common to abundant planktonic foraminifers between 7.78 and 378.9 m CSF-A. Biostratigraphic marker

Figure F8. Nannofossil preservation (1 = poor [P], 2 = moderate, 3 = good [G], 4 = very good) and abundance (0 = barren [B], 1 = rare, 2 = few, 3 = common, 4 = abundant, 5 = dominant [D]) data, Holes U1463B and U1463C. See **Biostratigraphy and micropaleontology** in the Expedition 356 methods chapter (Gallagher et al., 2017a) for preservation and abundance definitions. Biozonation scheme is that of Martini (1971), see Figure **F9** for details on biostratigraphic datums.

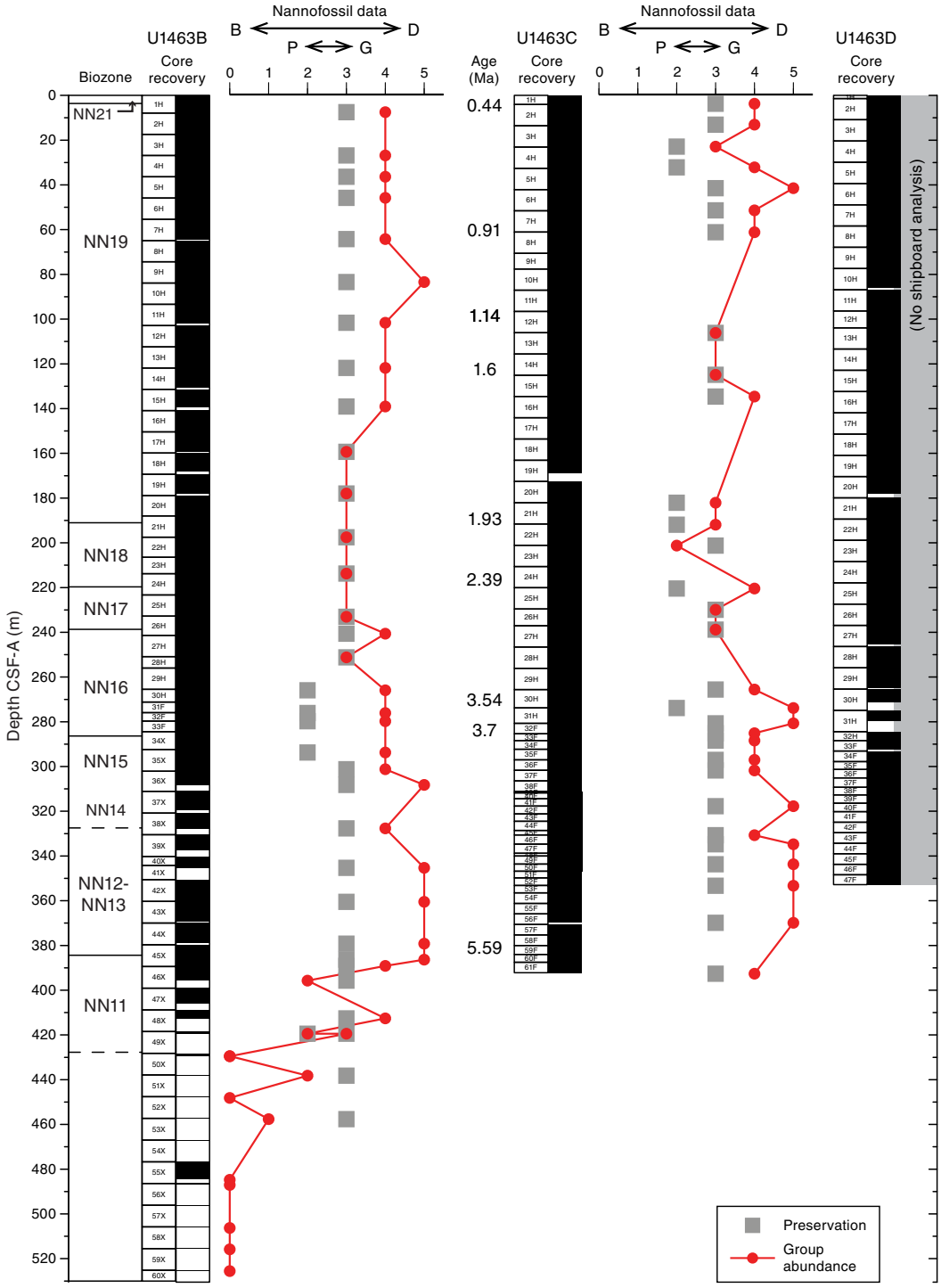

species were identified for the Middle Pleistocene (0.61 Ma; top of *Globorotalia tosaensis*) at 46 m CSF-A, the Pliocene/Pleistocene boundary below the top of *Globorotalia limbata* (2.39 Ma; 220.54 m CSF-A), *Dentoglobigerina altispira* (3.47 Ma; 265.87 m CSF-A) for the Pliocene, and *Sphaeroidinellopsis kochi* (top at 4.53 Ma; 334.71 m CSF-A) for the early Pliocene. An extended interval that was barren, or contained heavily recrystallized foraminifers and very rare nannofossils, occurs deeper than 429.28 m CSF-A to the bottom of Hole U1463B (~530 m CSF-A). The oldest biostratigraphic datum suggests the material in Sample 356-U1463B-48X-CC (412.44 m CSF-A) is older than 6.252 Ma (top of *Reticulofenestra rotaria* Biozone NN11; Young, 1998).

The samples from Holes U1463A–U1463C contain between 10% and 100% benthic foraminifers, with *Cibicidoides* spp. the most

common taxa. Five assemblages can be identified based on the abundance of *Quinqueloculina* spp. and *Textularia* spp. (Assemblage 1); *Operculina* spp. and *Amphistegina* spp. (Assemblage 2); *Cibicidoides* spp., *Rotalinoides gaimardii*, and *Lenticulina* spp. (Assemblage 3); *Pseudorotalia* spp., *Neoeponides* spp., *Planorbulinella larvata*, and *Bolivina* spp. (Assemblage 4); and *Cibicidoides* spp., *Anomalinoides* spp., and *Amphistegina lessonii* (Assemblage 5). Samples contained 1–43 species. Assemblages suggest paleodepths that start moderately deep (middle to outer shelf, Assemblage 1) and continue to fluctuate between middle to outer shelf and bathyal settings for the remainder of the site (Assemblage 3) with instances of downslope transported shallow-water taxa within deeper foraminiferal assemblages (Assemblages 2, 4, and 5). Preservation was affected by fragmentation, abrasion, and encrustation and varied from very good to poor throughout the site but was most frequently good to moderate with poor preservation only occurring deeper than 390 m CSF-A to the base of the site.

Calcareous nannofossils

A total of 73 smear slides were examined from Holes U1463B and U1463C, mainly at 20 m intervals, but at 10 m intervals where the presence of nannofossil datums was anticipated. Calcareous nannofossils recovered at Site U1463 represent a stratigraphic succession from the late Miocene to Late Pleistocene (Biozones NN11–NN19) (Figures **F8**, **F9**; Table **T6**). Calcareous nannofossils are common to abundant with moderate to good preservation throughout the section. Barren intervals were found from 429.28 m CSF-A to the bottom of Hole U1463B. Reworked specimens are not a major component of the sediments at this site, and only a few specimens of Oligocene taxa were observed in Samples 356-U1463B-36X-CC through 44X-CC (208–279 m CSF-A) and 356-U1463C-61F-CC (392.49 m CSF-A).

Pleistocene

Scanning electron microscope (SEM) analysis confirmed the presence of *Emiliania huxleyi* (Figure **F10A**) in the mudline sample (Section 356-U1463B-1H-1), placing the top of this core within nannofossil Biozone NN21 (<0.29 Ma). The occurrence of *Pseudoemiliania lacunosa* (Figure **F10B**) and absence of *E. huxleyi* in the uppermost core catcher samples in Holes U1463B and U1463C at 7.8 m CSF-A (Sample 356-U1463B-1H-CC) and 4.11 m CSF-A (Sample 356-U1463C-1H-CC), indicate that the samples are within Biozone NN19 (>0.44 Ma; Figure **F9**). The species *Reticulofenestra asanoi* (Figure **F10C**) is in Samples 356-U1463B-7H-CC through 11H-CC (64.54–101.89 m CSF-A), constraining the age to 0.91–1.14 Ma within Biozone NN19. The top occurrence of *Calcidiscus macintyrei* (1.6 Ma; Figure **F10D**), which indicates the basal part of Biozone NN19, is present in Samples 356-U1463B-15H-CC (139.28 m CSF-A) and 356-U1463C-14H-CC (125.12 m CSF-A) (Figure **F9**). The top of *Discoaster brouweri* (Figure **F10E**), which defines the NN18/NN19 boundary (1.93 Ma), correlates well between Holes U1463B and U1463C and is present in Samples 356-U1463B-21H-CC (197.65 m CSF-A) and 356-U1463C-21H-CC (192.05 m CSF-A). The Biozone NN18/NN17 boundary (2.39 Ma) is defined by the top occurrence of *Discoaster pentaradiatus* (Figure **F10F**) in Samples 356-U1463B-25H-CC (233.15 m CSF-A) and 356-U1463C-24H-CC (220.54 m CSF-A).

The Pleistocene assemblages are characterized by different (size defined) morphotypes of *Gephyrocapsa* spp., *P. lacunosa*, and *Reticulofenestra* spp. Small placoliths (<3 µm) are abundant to dominant in the early Pleistocene section (Table **T7**). Other common taxa include *Calcidiscus leptoporus, Umbilicosphaera sibogae, Syracosphaera pulchra, Pontosphaera* spp., and *Helicosphaera* spp. Specimens of *Coccolithus pelagicus* are absent in the Late Pleistocene but are rare in the early Pleistocene section.

Pliocene

The top of Biozone NN16, which includes the Pliocene/Pleistocene boundary, is marked by the presence of *Discoaster surculus* (2.49 Ma; Figures **F9**, **F10G**) in Section 356-U1463B-26H-6 (240.7 m CSF-A). The top occurrence of *Discoaster tamalis* (2.8 Ma, within Biozone NN16; Figure **F10H**) is in Sample 27H-CC (251.26 m CSF-A) but was not observed in core catcher samples from Hole U1463C. The top occurrence of *Sphenolithus* spp. (3.54 Ma; Figure **F10I**), in the basal part of Biozone NN16, is at 276.11 m CSF-A in Hole U1463B (Sample 31F-CC) and 273.88 m CSF-A in Hole U1463C (Section 30H-6). The Biozone NN16/NN15 boundary (3.7 Ma) is defined by the top occurrence of *Reticulofenestra pseudoumbilicus* (Figure **F10J**) at 293.74 m CSF-A (Sample 356-U1463B-34X-CC) and 288.41 m CSF-A (Section 356-U1463C-33F-2), marking the early/late Pliocene boundary.

The Pliocene nannofossil assemblages mainly consist of different (size defined) morphotypes of *Reticulofenestra* spp. and *P. lacunosa*. Small placoliths (2–3 and 3–5 µm) are common to very abundant in the Pliocene section (Table **T7**). Other typical contributors to the assemblage include rare to few *Discoaster* spp.; common to abundant *Sphenolithus* spp.; and few *Calcidiscus* spp., *Helicosphaera carteri, Pontosphaera* spp., *Umbilicosphaera* spp., and *Scyphosphaera* spp. Specimens of *C. pelagicus* are present between Samples 356-U1463B-38X-CC and 49X-CC (327.62 and 419.38 m CSF-A), characterizing earliest Pliocene and late Miocene assemblages (see below).

Late Miocene

We did not observe the marker species that define late Miocene and early Pliocene Biozones NN14–NN12 (e.g., *Amaurolithus* spp. and *Ceratolithus* spp.). Therefore, the Miocene/Pliocene boundary in Biozone NN12 was difficult to constrain. The top of late Miocene Biozone NN11 (5.59 Ma) was identified by the presence of *Discoaster quinqueramus* (Figure **F10K**) at 386.22 m CSF-A (Section 356-U1463B-45X-6) and 392.49 m CSF-A (Sample 356-U1463C-61F-CC). The top occurrence of *R. rotaria*, which has a short age range within Biozone NN11B (Young, 1998, Figure **F10L**), is in Sample 356-U1463B-48X-CC (412.44 m CSF-A). Deeper than ~415 m CSF-A, calcareous nannofossils markedly decreased to rare or few or were absent. Therefore, the downhole extension of Biozone NN11 is not further constrained.

The Miocene assemblages are dominated by small-sized (2–5 µm) *Reticulofenestra* spp. with variable contributions of *R. pseudoumbilicus* (<7 and >7 µm); common to abundant *Sphenolithus* spp.; and rare to common *Discoaster* spp., *Calcidiscus* spp., *C. pelagicus, H. carteri, Pontosphaera* spp., and *Umbilicosphaera rotula*.

Planktonic foraminifers

One sample was examined from Hole U1463A, 34 from Hole U1463B, and 25 from Hole U1463C. Planktonic foraminifers recovered at Site U1463 represent a stratigraphic succession from the early Pliocene to recent (Table **T6**). Preservation ranged from moderate to very good in Holes U1463B and U1463C (to ~345 m CSF-A) with 12–16 species per sample (Table **T8**; Figure **F11**) and up to 80% planktonic foraminifers relative to benthic foraminifers. From

Figure F9. Ranges of late Miocene to Late Pleistocene calcareous nannofossil age markers, Holes U1463B and U1463C (no shipboard analyses were done on Hole U1463D). Green bars = age-depth tie points and robust correlations between holes. Pliocene/Pleistocene boundary (2.58 Ma) lies within Biozone NN16, approximated by the top of *Discoaster surculus* (2.49 Ma). Early Pliocene/late Pliocene boundary lies between the top of *Sphenolithus* spp. (3.54 Ma) and top of *Reticulofenestra pseudoumbilicus* (3.7 Ma). The base of *Pseudoemiliania lacunosa* (4.2 Ma) is used to denote the base of early Pliocene Biozone NN14. Miocene/Pliocene boundary (5.33 Ma) lies within Biozone NN12 but is difficult to constrain because of the lack of marker species. The top of *D. quinqueramus* indicates late Miocene (Messinian) age (Biozone NN11).

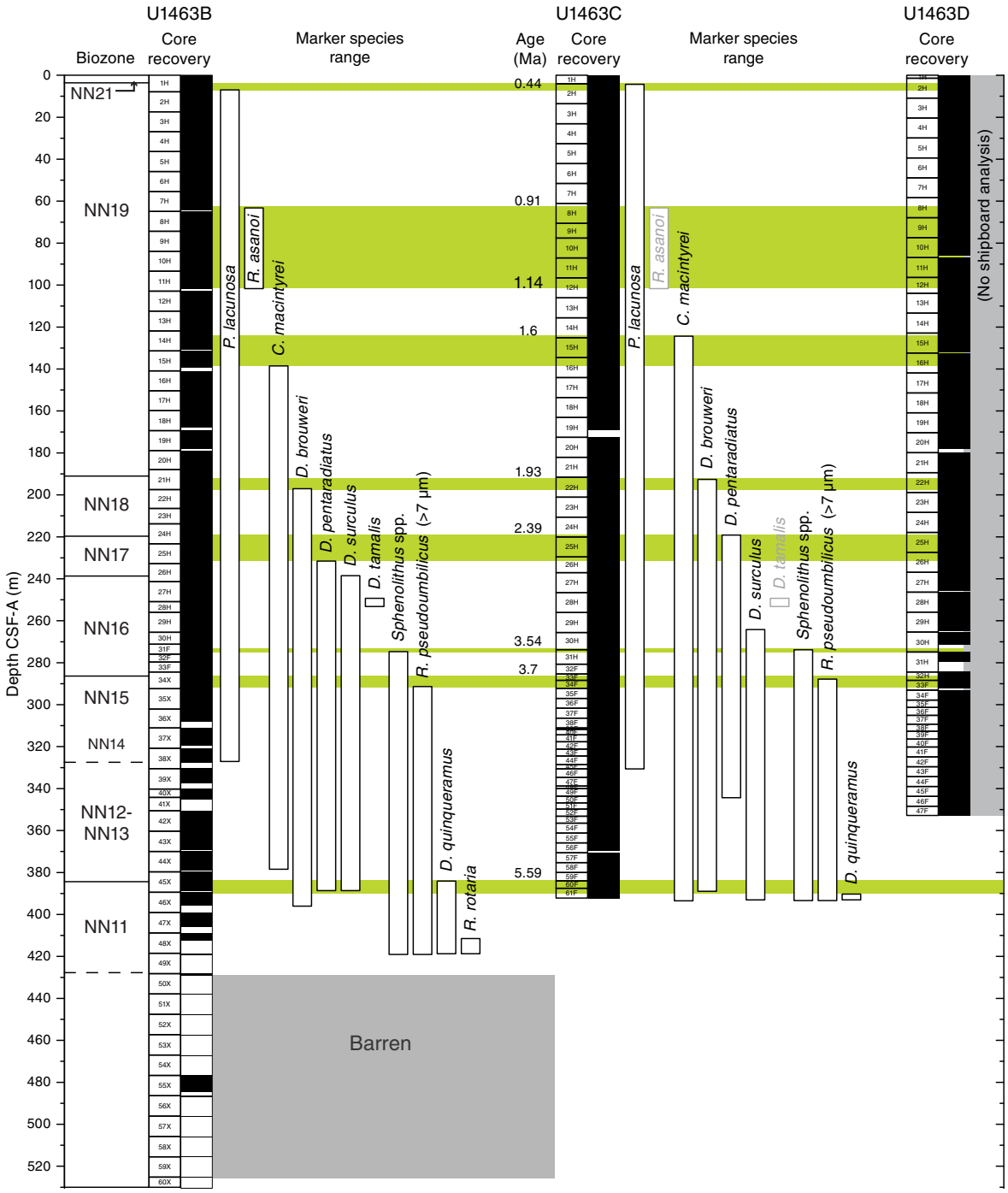

~360 m CSF-A (early Pliocene) downhole preservation was generally poor (poor to moderate) and accordingly, planktonic foraminiferal abundance decreased (Figure **F12**; Table **T9**). An extended barren interval occurred in the bottom of Hole U1463B from 429.26 to 525.25 m CSF-A (Samples 50X-CC through 60X-CC), corresponding to the deepest sections of the site.

The general preservation for the Pleistocene–Pliocene section at Site U1463 is better than at the previous sites of this expedition (Figure **F11**). Accordingly, the biostratigraphy could be established down to the early Pliocene (Tables **T6**, **T8**; Figure **F13**). The top of *G. tosaensis* at 0.61 Ma is in Sample 356-U1463C-2H-CC (13.45 m CSF-A) indicating the Middle Pleistocene (transition Biozone Pt1a–

Table T6. Calcareous nannofossil (CN) and planktonic foraminifer (PF) datums, Site U1463. * = datums likely out of position. X = change in coiling direction. Ages are based on Gradstein et al. (2012). Table is based on all core catcher samples from all holes, indicating only the highest/lowest depth for each top/base event. **Download table in .csv format.**

Hole, core, section, interval (cm)	Depth CSF-A (m)	Marker species	Type (CN/PF)	Zone name	Age (Ma)	Reference
356-						
U1463C-1H-CC	4.11	Top *Pseudoemiliania lacunosa*	CN	NN19	0.44	Gradstein et al., 2012
U1463C-2H-CC	13.45	Top *Globorotalia tosaensis*	PF	Pt1a	0.61	Gradstein et al., 2012
U1463B-7H-CC	64.54	Top *Reticulofenestra asanoi*	CN	NN19	0.91	Gradstein et al., 2012
U1463B-11H-CC	101.89	Base *Reticulofenestra asanoi*	CN	NN19	1.14	Gradstein et al., 2012
U1463C-14H-CC	125.12	Top *Calcidiscus macintyrei*	CN	NN19	1.60	Gradstein et al., 2012
U1463B-15H-CC	139.28	Top *Globigerinita apertura*	PF	Pt1a	1.64	Gradstein et al., 2012
U1463C-20H-CC	182.24	Base *Globorotalia truncatulinoides*	PF	Pt1a	1.93	Gradstein et al., 2012
U1463C-21H-CC	192.05	Top *Discoaster brouweri*	CN	NN18	1.93	Gradstein et al., 2012
U1463C-21H-CC	192.05	Top *Globigerinoides extremus*	PF	PL6	1.99	Gradstein et al., 2012
U1463C-24H-CC	220.54	Top *Discoaster pentaradiatus*	CN	NN16	2.39	Gradstein et al., 2012
U1463C-24H-CC	220.54	Top *Globigerinoides fistulosus**	PF	PT1a	1.88	Gradstein et al., 2012
U1463C-24H-CC	220.54	Top *Globorotalia limbata*	PF	PL5	2.39	Gradstein et al., 2012
U1463C-26H-CC	238.89	Base *Globorotalia tosaensis*	PF	PL5	3.35	Gradstein et al., 2012
U1463B-26H-6, 50–50	240.70	Top *Discoaster surculus*	CN	NN16	2.49	Gradstein et al., 2012
U1463B-27H-CC	251.26	Top *Discoaster tamalis*	CN	NN16	2.80	Gradstein et al., 2012
U1463C-29H-CC	265.63	Top *Dentoglobigerina altispira* (Pacific)	PF	PL4	3.47	Gradstein et al., 2012
U1463C-30H-6	273.88	Top *Sphenolithus* spp.	CN	NN16 (basal part)	3.54	Gradstein et al., 2012
U1463C-30H-6	273.88	Top *Pulleniatina primalis*	PF	PL3	3.66	Gradstein et al., 2012
U1463C-33F-2	288.41	Top *Reticulofenestra pseudoumbilicus* (>7 µm)	CN	NN15	3.70	Gradstein et al., 2012
U1463C-36F-4	301.75	Top *Globorotalia margaritae*	PF	PL2	3.85	Gradstein et al., 2012
U1463B-36X-CC	308.11	X *Pulleniatina* sin to dex	PF	PL2	4.08	Gradstein et al., 2012
U1463B-36X-CC	308.11	Top *Sphaeroidinellopsis seminulina**	PF	PL3	3.58	Gradstein et al., 2012
U1463C-46F-3	334.71	Top *Sphaeroidinellopsis kochi*	PF	PL1 (Indo-Pacific)	4.53	Gradstein et al., 2012
U1463B-45X-6, 0–0	386.22	Top *Discoaster quinqueramus*	CN	NN11	5.59	Gradstein et al., 2012
U1463B-48X-CC	412.44	Top *Reticulofenestra rotaria*	CN	NN11	6.25	Young, 1998

Figure F10. SEM and plane-polarized light (PPL) photomicrographs of calcareous nannofossils, Site U1463. A. *Emiliania huxleyi*. B. *Pseudoemiliania lacunosa*. C. *Reticulofenestra asanoi*. D. *Calcidiscus macintyrei*. E. *Discoaster brouweri*. F. *Discoaster pentaradiatus*. G. *Discoaster surculus*. H. *Discoaster tamalis*. I. *Sphenolithus* spp. J. *Reticulofenestra pseudoumbilicus*. K. *Discoaster quinqueramus*. L. *Reticulofenestra rotaria*.

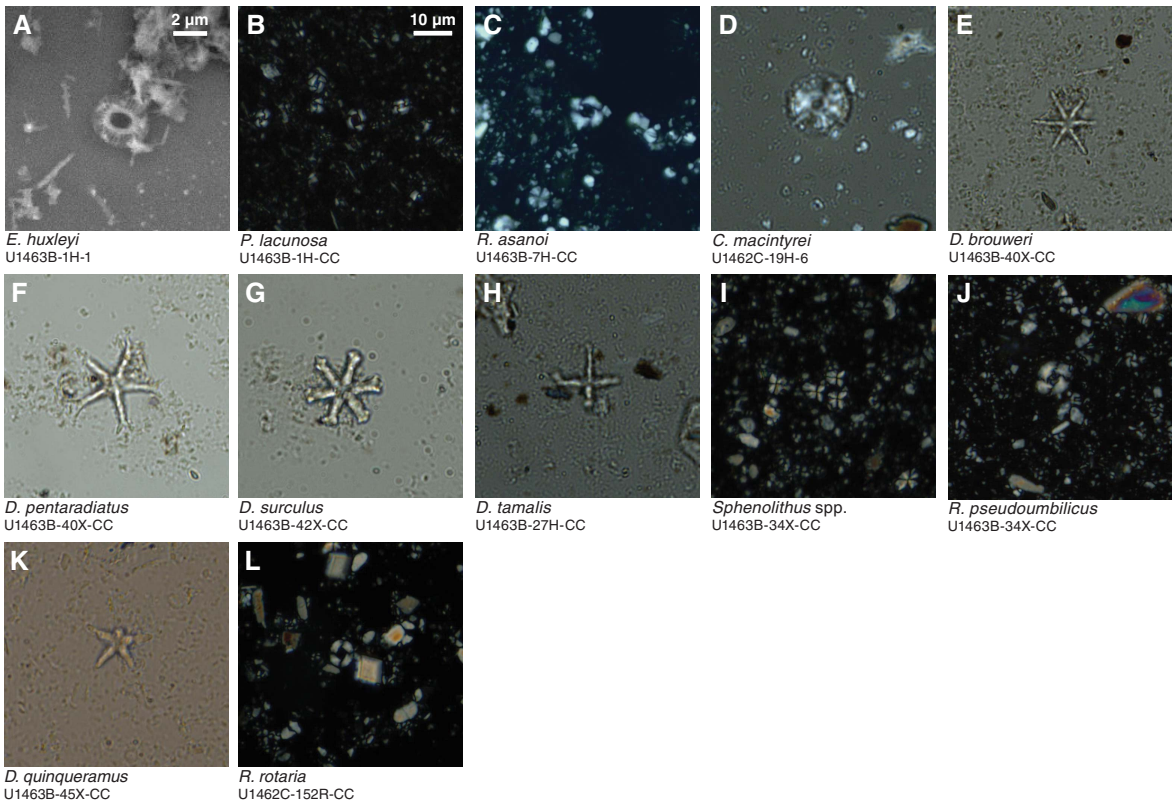

Table T7. Calcareous nannofossil abundance and range charts, Site U1463. **Download table in .csv format.**

Table T8. Planktonic foraminifer presence, abundance, and preservation at Site U1463, including characteristic mineral and other bioclast occurrences. **Download table in .csv format.**

Figure F11. SEM photomicrographs of typical preservation states of planktonic foraminifers, Site U1463. The depicted species is *Globigerinoides sacculifer* (or closely related to *G. sacculifer*). Depths are in CSF-A.

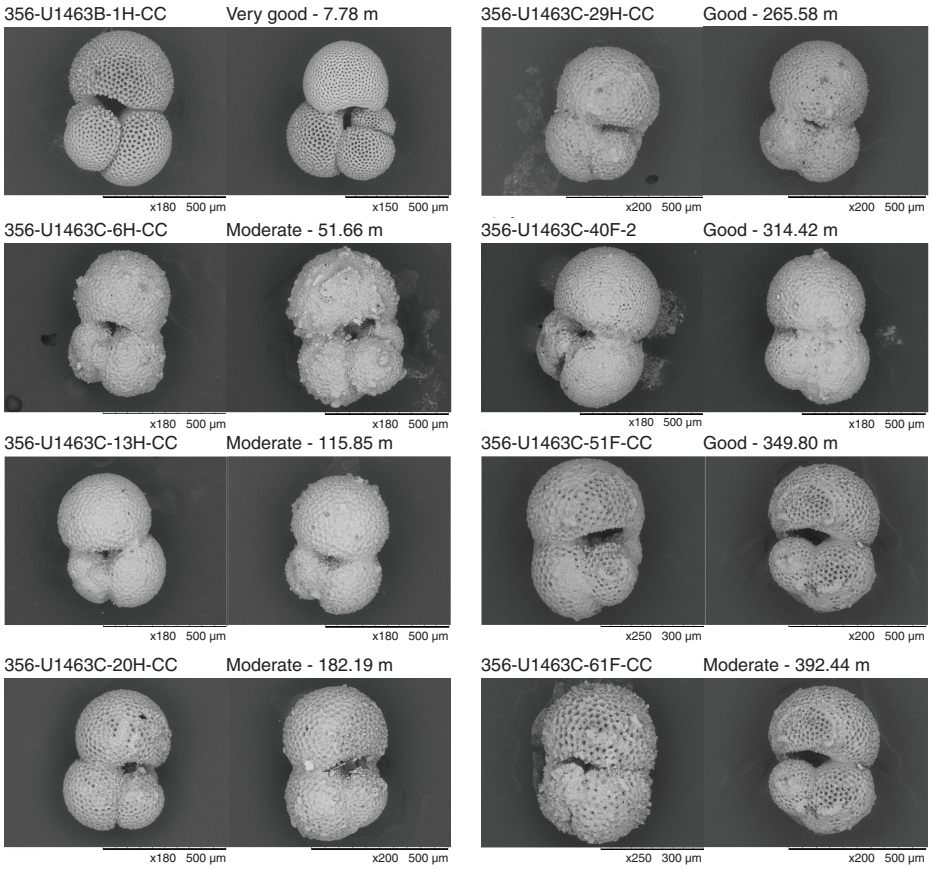

Figure F12. Planktonic foraminiferal abundance, Site U1463. 0 = barren, 1 = very rare, 2 = rare, 3 = few, 4 = common, 5 = abundant (see **Biostratigraphy and micropaleontology** in the Expedition 356 methods chapter [Gallagher et al., 2017a] for definitions).

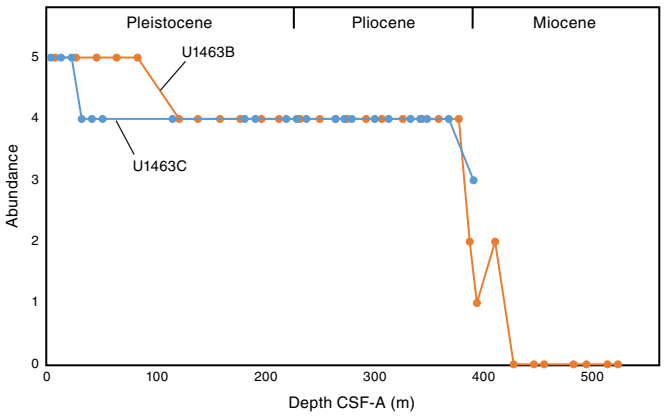

Pt1b). The early Pleistocene is characterized by the base of *Globorotalia truncatulinoides* (base of Biozone Pt1a; 1.93 Ma) in Sample 20H-CC (182.24 m CSF-A) and *Globigerinoides extremus* (top of Biozone PL6; 1.99 Ma) in Sample 21H-CC (192.05 m CSF-A), followed by the transition into the Pliocene below the top of *G. limbata* (Biozone PL5; 2.39 Ma) in Sample 24H-CC (220.54 m CSF-A). Pliocene marker species, such as *G. tosaensis* (3.35 Ma, base of Biozone PL5), *D. altispira* (3.47 Ma, top of Biozone PL4), *Pulleniatina primalis* (3.66 Ma, top of Biozone PL3), and *Globorotalia margaritae* (3.85 Ma, top of Biozone PL2), were found at the same approximate depths in Holes U1463B and U1463C (Table **T6**; Figure **F13**). Additionally, early Pliocene Biozone PL1 could be identified at Site U1463 by the top of *S. kochi* (top at 4.53 Ma) in the sample from Section 356-U1463C-46F-3 (334.71 m CSF-A). Moreover, typical species for the early Pleistocene like *Globigerinoides obliquus, Globigerinita apertura*, and *Globigerinoides fistulosus* were also present.

The well-preserved samples allowed determination of the dominant coiling direction in the genus *Pulleniatina* (Table **T10**) (Saito, 1976; Pearson, 1995). Two well-recorded changes from sinistral to 100% dextral coiling can be used as stratigraphic markers for the early Pliocene (4.08 Ma), identified at ~310 m CSF-A (Figure **F14**) and the disappearance of sinistral specimens between Samples 356-U1463B-3H-CC and 9H-CC (27.1 and 83.62 m CSF-A) at <0.8 Ma (Gradstein et al., 2012; Chaisson and Pearson, 1997).

Table T9. Planktonic foraminifer abundance, Site U1463. 0 = barren, 1 = very rare, 2 = rare, 3 = few, 4 = common, 5 = abundant (see **Biostratigraphy and micropaleontology** in the Expedition 356 methods chapter [Gallagher et al., 2017a] for definitions). **Download table in .csv format.**

Core, section	Depth CSF-A (m)	Abundance
356-U1463B-		
1H-CC	7.88	5
3H-CC	27.20	5
5H-CC	46.13	5
7H-CC	64.54	5
9H-CC	83.72	5
13H-CC	122.05	4
15H-CC	139.28	4
17H-CC	159.50	4
19H-6	178.12	4
21H-CC	197.65	4
23H-5	213.81	4
25H-CC	233.10	4
27H-CC	251.18	4
29H-CC	265.92	4
31F-CC	276.11	4
34X-CC	293.74	4
36X-CC	308.21	4
38X-CC	327.62	4
40X-CC	345.21	4
42X-CC	360.39	4
44X-CC	379.05	4
45X-CC	388.96	2
46X-CC	395.59	1
48X-CC	412.44	2
50X-CC	429.36	0
52X-CC	447.95	0
53X-CC	457.40	0
55X-CC	484.50	0
57X-CC	496.19	0
59X-CC	515.55	0
60X-CC	525.25	0

Benthic foraminifers

One core catcher sample was investigated from Hole U1463A, 34 from Hole U1463B, and 14 from Hole U1463C. Additionally, a spot sample was taken from Hole U1463B in order to confirm the presence of a particular assemblage (5; see below). Overall, the number of species present per sample ranged from 1 (Core 356-U1463B-55X; 484.4.5 m CSF-A) to 43 (Sample 1H-CC; 7.88 m CSF-A). The benthic foraminiferal percentage ranged from 10% (e.g., Sample 356-U1463C-40X-CC; 345.21 m CSF-A) to 100% (e.g., Samples 356-U1463B-53X-CC and 55X-CC; 457.4–484.5 m CSF-A) (Tables **T11**, **T12**). The three deepest samples from Hole U1463B were barren of benthic foraminifers (Samples 57X-CC through 60X-CC; 496.19–525.25 m CSF-A).

Preservation in the single sample from Hole U1463A (Sample 2X-CC; 18.29 m CSF-A) was good. In Hole U1463B, preservation ranged from very good to poor with the majority of samples being moderate (11 out of 31) (Table **T11**). In Hole U1463C, 1 out of 14 samples showed poor preservation and 5 were well preserved, whereas the majority showed moderate preservation (7 out of 14). Preservation was affected by abrasion and fragmentation (breakage), as well as occasional cementation and infilling (coating in secondary crystals) with glauconite and pyrite. Secondary crystal coating and clay clumps were partially removed by ultrasonication.

Cibicidoides spp. was almost always present throughout this site, but five foraminiferal assemblages were defined by varying dominant taxa. Except for Assemblages 2 and 5, all assemblages overlapped without clear boundaries (Table **T12**; Figure **F15**).

The first benthic foraminiferal assemblage is found in all three holes analyzed (Holes U1463A–U1463C) from the uppermost core in each hole through Sample 356-U1463B-9H-CC (83.72 m CSF-A) in Hole U1463B and through Sample 356-U1463C-3H-CC (23.26 m CSF-A) in Hole U1463C. This assemblage contains a wide range of both shallow-water (0–50 m paleodepth) species such as *Quinqueloculina* spp. and *Rosalina* spp. and also abundant deeper (50–200 m) species, including *Triloculina* spp., *Lenticulina* spp., and uvigerinids, with between 22 and 43 species per sample and very good to poor preservation. Other abundant taxa include *Textularia* spp., *Lagena* spp., and *A. lessonii* (Figure **F15**). Owing to the wide-ranging species comprising this assemblage, the paleodepth ranges from inner shelf to outer shelf.

Assemblage 2 is marked by the strong dominance of inner shelf LBFs *Amphistegina* spp. and large specimens of *Operculina* spp. and *Operculina ammonoides* (>1 cm diameter). Assemblage 2 was only encountered in Sample 356-U1463C-9H-CC (78.63 m CSF-A). This assemblage is dominated by large endosymbiotic foraminiferal species typical of a shallow (0–50 m) marine setting proximal to a reef. Because Assemblage 2 appears only briefly, is bounded by a middle to outer shelf assemblage (Assemblage 1; Figure **F15**), and has sharp nongradational boundaries, it is likely that these specimens have been transported in from a shallower marine setting.

Assemblage 3 is present in Samples 356-U1463B-11H-CC through 23H-CC (101.87–213.7 m CSF-A) and 356-U1463C-11H-CC through 22H-CC (96.68–201.37 m CSF-A) (Figure **F15**). With 19–32 species per sample and good to moderate preservation, Assemblage 3 is dominated by *Cibicidoides* spp. with prominent secondary taxa *Lenticulina* spp. and *Textularia* spp. and occasionally by larger benthic species such as *R. gaimardii* or *Neoeponides margaritifer*. This assemblage likely indicates a middle to outer shelf setting.

Assemblage 4 is present in Samples 356-U1463B-25H-CC through 44X-CC (233.05–379.05 m CSF-A) and 356-U1463C-25H-CC through 56F-CC (220.49–396.77 m CSF-A). The assemblage has between 17 and 27 species per sample with good to moderate preservation. Assemblage 4 is dominated by a broad and varying range of both shallow endosymbiotic species, including *P. larvata*, and deeper inner shelf and middle to outer shelf taxa, including *Lenticulina* spp., *Pseudorotalia indopacifica, Pseudorotalia schroeteriana, N. margaritifer*, and *R. gaimardii* (Figure **F15**; Table **T11**).

Assemblage 5 is present in Samples 356-U1463B-45X-CC through 55X-CC (388.96–484.5 m CSF-A) and 356-U1463C-61F-CC (392.49 m CSF-A) (Figure **F15**; Table **T11**). With 1–21 species per sample, it is marked by a sharp drop in preservation quality and is dominated by species such as *Cibicidoides* spp. and *Anomalinoides* spp. Common secondary species include *A. lessonii, P. larvata*, and *Elphidium craticulatum*. *Anomalinoides* spp. and *Cibicidoides* spp. indicate an outer shelf to upper bathyal marine setting with downslope transported shallow *Amphistegina* spp., *Planorbulinella* spp., and *Elphidium* spp. These species are typical of various bathymetric settings from inner to outer shelf. Due to the poor quality of these specimens, Assemblage 5 was likely impacted by selective preservation, which destroyed more fragile test types and influenced the planktonic/benthic ratio. This poor preservation may be due to the original high-energy setting of this section (see **Unit IV** and **Unit V**). The co-occurrence of specimens either heavily affected or completely unaffected by glauconite together with recrys-

Figure F13. Planktonic foraminiferal marker species ranges, Holes U1463B and U1463C. Ages are based on published values (Gradstein et al., 2012).

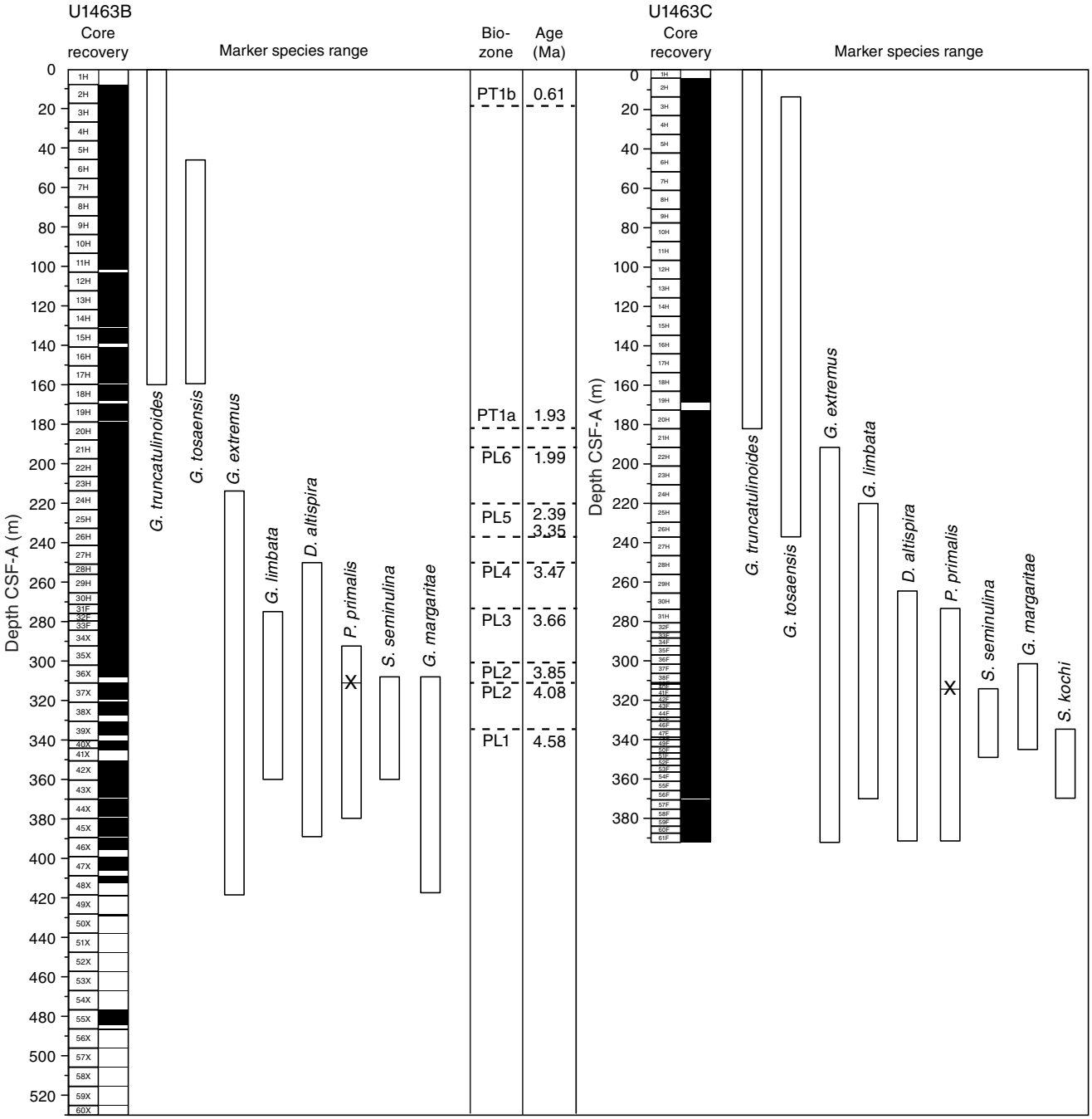

tallized and heavily abraded specimens suggests a phase of reworking of older material in this region.

Overall paleodepth estimates based on the planktonic/benthic foraminifer ratio (%P) range between 30 (100% benthic in Sample 356-U1463B-40X-CC; 345.21 m CSF-A) and >1000 m (10% benthic in Sample 53X-CC; 447.95 m CSF-A) (Table **T11**). The shallowest paleodepths (30–150 m) are encountered in Assemblage 5; however, poor preservation and the large drop in planktonic abundance make it likely that the %P of this assemblage is not representative and therefore unreliable for paleodepth reconstructions.

Investigated benthic foraminifer percentage and diversity, combined for all holes at Site U1463, are illustrated in Figure **F16**.

Table T10. Coiling direction for *Pulleniatina* spp. at Site U1463, including specific species per sample. Estimated age based on Table **T6** and Saito (1976). **Download table in .csv format.**

Hole, core, section	Top depth CSF-A (m)	Bottom depth CSF-A (m)	Species (Pullen)	Dextral	Sinistral	Total	% dextral	Estimated age	Coiling age	Saito, 1976 events
356-										
U1463B-1H-CC	7.78	7.88	*P. obliquiloculata*	27	0	27	100			
U1463A-2X-CC	18.19	18.29	*P. obliquiloculata*	34	0	34	100			
U1463B-3H-CC	27.10	27.20	*P. obliquiloculata*	19	0	19	100	<0.44		
U1463B-9H-CC	83.62	83.72	*P. obliquiloculata*	18	5	23	78	>0.91	>0.8	L1/L2
U1463C-13H-CC	115.85	115.90	*P. obliquiloculata*	6	0	6	100	<1.6		
U1463C-20H-CC	182.19	182.24	*P. obliquiloculata*	3	2	5	60	1.93		L5–L8
U1463C-21H-CC	192.00	192.05	*P. obliquiloculata*	7	0	7	100	1.99		
U1463B-23H-5	213.76	213.81	*P. obliquiloculata*	14	2	16	88	1.99		L5–L8
U1463C-24H-CC	220.49	220.54	*P. obliquiloculata*	4	8	12	33	2.39		L5–L8
U1463B-25H-CC	233.05	233.10	*P. obliquiloculata*	9	0	9	100	2.39		
U1463C-29H-CC	265.58	265.63	*P. obliquiloculata*	7	0	7	100	3.47		
U1463B-34X-CC	293.64	293.74	*P. obliquiloculata/P. primalis*	15	1	16	94	3.7		
U1463C-36F-4	301.70	301.75	*P. obliquiloculata/P. primalis*	18	0	18	100	3.85		
U1463B-36X-CC	308.11	308.21	*P. primalis*	0	5	5	0	4.08	4.08	L9
U1463C-51F-CC	349.80	349.85	*P. primalis*	1	16	17	6			
U1463C-56F-3	369.72	396.77	*P. primalis*	0	6	6	0			
U1463C-61F-CC	392.44	392.49	*P. primalis*	1	1	2				

Figure F14. Variation in the coiling direction of planktonic foraminiferal genus *Pulleniatina*, Site U1463. Samples to 265 m CSF-A are *P. obliquiloculata*, samples deeper than 308 m CSF-A are *P. primalis*, and samples in between are a mixture of both species. Note that specimens of *P. finalis* were included with *P. obliquiloculata* (Kennett and Srinivasan, 1983). Ages are based on Saito (1976) and Pearson (1995) and recalibrated following Wade et al. (2011).

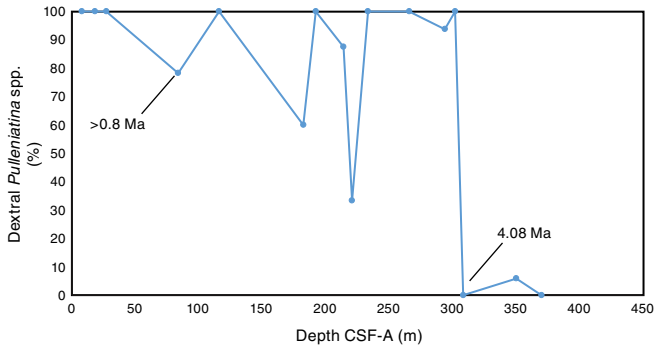

Table T11. Occurrence of the main genera and species of benthic and planktonic foraminifers and additional bioclasts and minerals, Site U1463. Preservation: G = good, VG = very good. Paleodepth estimates are based on calculations from van Hinsbergen et al. (2005). Bathymetric zones: IS = inner shelf, MS = middle shelf, OS = outer shelf, UB = upper bathyal. Abundance: C = common, P = present, R = rare. (Only a portion of this table appears here. The complete table is available in **.csv format**.)

			Benthic foraminifers							Planktonic foraminifers				Other							
Core, section	Top depth CSF-A (m)	Bottom depth CSF-A (m)	Preservation	Benthic foraminifers/total foraminifer assemblage (%)	Planktonic foraminifers/total foraminifer assemblage (%)	Paleodepth estimate %P (m)	Total number of benthic species	Bathymetric zone	Most abundant benthic foraminifer species (descending order)	Preservation	Total number of planktonic species	Most frequent planktonic foraminifer species	Biozone (Gradstein et al., 2012)	Glauconite	Pyrite	Sponge spicules	Ostracods	Pteropods	Fish teeth	Bryozoans	Comment
356-U1463A-																					
2X-CC	18.19	18.29	G	18	82	924	39	MS/OS/UB	*Cibicidoides* spp., *Lagena* spp., *Lenticulina* spp., *Quinqueloculina* spp., *Rosalina* spp., *Siphouvigerina porrecta*, *Triloculina* spp., *Uvigerina* spp.	VG	11	*P. obliquiloculata, G. truncatulinoides, G. crassaformis, G. siphonifera, N. dutertrei, G. ruber*					X				100% dex Pulleniatina (34 dex, 0 sin)
356-U1463-B-																					
1H-CC	7.78	7.88	VG	25	75	691	43	IS/MS/OS	*Quinqueloculina* spp., *Lagena* spp, *Cibicidoides* spp., *Lenticulina* spp., *Nodosaria* spp., *Rosalina* spp., *Siphouvigerina porrecta*, *Spiroloculina* sp. 1, *Textularia* spp., *Triloculina* spp., *Uvigerina* spp.	VG	14	*P. obliquiloculata, G. tumida, N. dutertrei, G. siphonifera, C. nitida, S. dehiscens, G. ruber*					X	X			Ostracods (R); pteropods (P); scaphopods (C)
3H-CC	27.1	27.2	VG	27	73	635	37	IS/MS/OS	*Textularia* spp., *Amphistegina papillosa*, *Cibicidoides* spp., *Lenticulina* spp., *Quinqueloculina* spp., *Rosalina* spp., *Siphogenerina raphana*, *Siphonaperta* spp.	G	9	*G. truncatulinoides, G. crassaformis, P. obliquiloculata, N. dutertrei, G. ruber*	T *Globorotalia tosaensis*	X			X		X		

Table T12. Benthic foraminifer abundance, Site U1463. **Download table in .csv format.**

Figure F15. Optical and SEM photomicrographs of dominant benthic foraminiferal species and assemblages at Site U1463 together with paleodepth based on planktonic/benthic ratio (%P) and bathymetric zone interpretation. Assemblage bathymetric zones were smoothed to generate a synthesis, resulting in slight differences from hole summary data. For raw bathymetric zonation see Table **T11**. This figure is available in an **oversized format**.

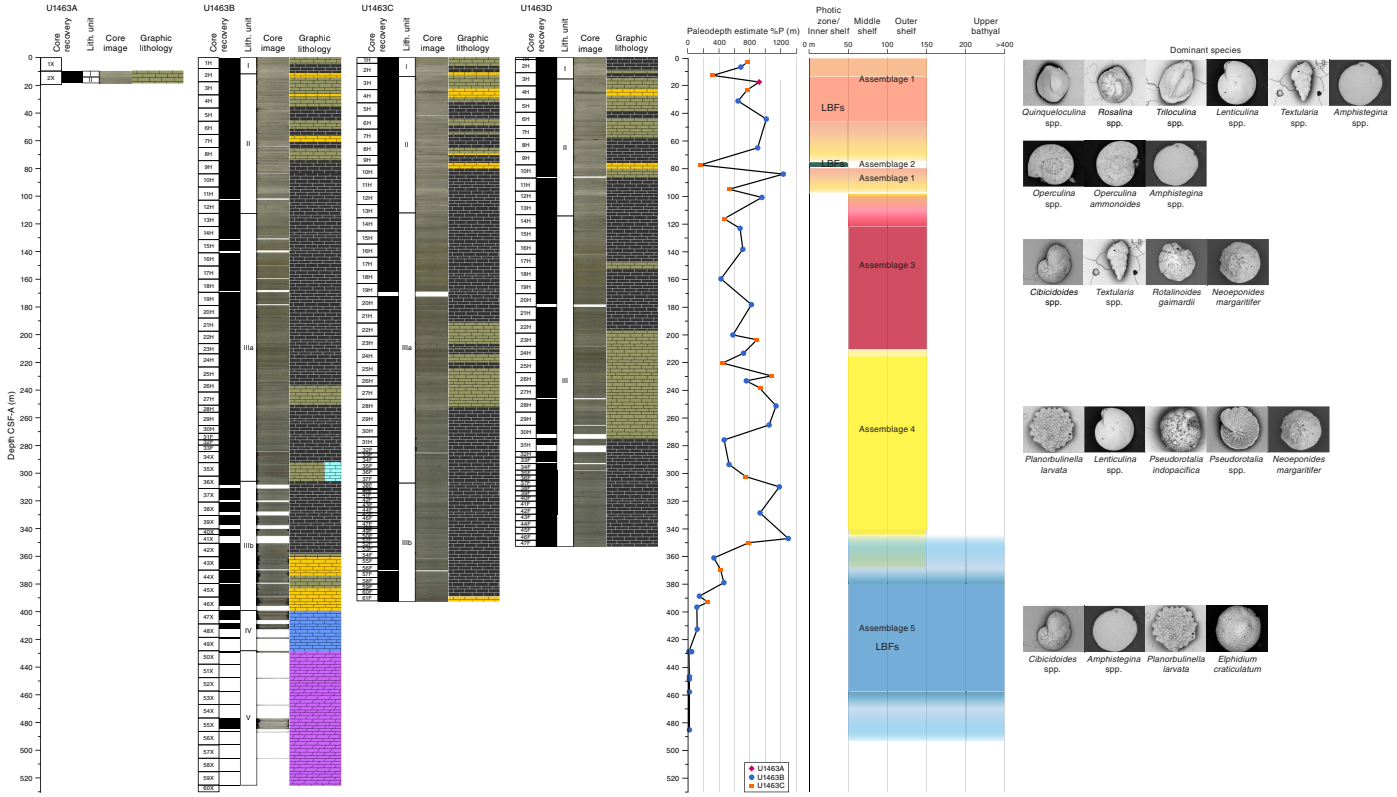

Figure F16. Benthic foraminifer diversity (number of species) and benthic percentage of total foraminifers, Site U1463. Analyzed samples from Holes U1463A–U1463C are combined by CSF-A.

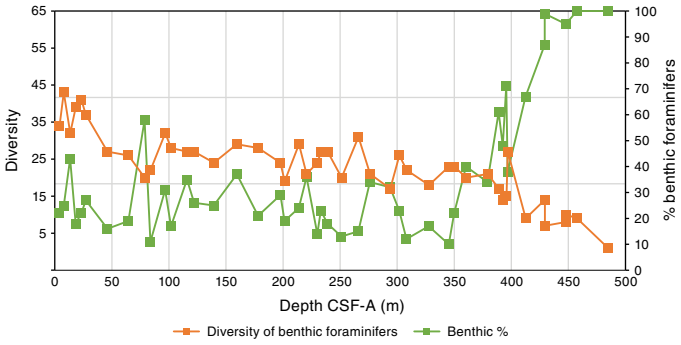

Geochemistry

At Site U1463, 56 samples were analyzed for headspace gas content and 25 samples (5–15 cm whole rounds) for interstitial water (IW) geochemistry and bulk sediment geochemistry (total organic carbon [TOC], calcium carbonate, and total nitrogen [TN]). No IW samples were collected in Holes U1463C or U1463D because these two holes recovered a section that had already been sampled in Holes U1463A and U1463B. Only one sample was taken from Hole U1463A. Thus, "bottom" in this geochemistry section refers to the base of Hole U1463B (530 m CSF-A), which corresponds to the base of the section. In general, elevated salinity characterizes the site, with a value of 35 at the top, increasing gradually with depth to a value of 111 at the bottom, and a mean value of 70. Similar to Site U1462, the high salinity at Site U1463 and a number of elemental trends noted in the IW samples appear to be related to the presence and dissolution of anhydrite, which was observed at the bottom of the section (Unit V; 428.2–525.25 m CSF-A). A number of elements exhibit increasing concentrations with depth, including sodium, chloride, barium, bromine, calcium, potassium, and sulfate. Site U1463 is characterized by low headspace gas concentrations, with methane concentrations ranging from 1.6 to 13.4 parts per million by volume (ppmv) and almost no detection of higher molecular weight hydrocarbons. Further, this site is characterized by high calcium carbonate content (mean = 77.5 wt%), low TOC (mean = 0.7 wt%), and low TN (mean = 0.031 wt%).

Headspace gases

Headspace gas analysis for routine safety monitoring revealed the presence of methane and ethane in low concentrations (Figure **F17**; Table **T13**). All 56 samples analyzed contained methane, ranging in concentration from 1.6 to 13.4 ppmv. Ethane is only present in two samples (356-U1463B-42X-4, 0–5 cm, and 44X-4, 0–5 cm; 355 and 374 m CSF-A) and in trace concentrations (<1.1 ppmv), whereas propane was not detected. Methane concentrations display an overall increasing trend from the surface to ~200 m CSF-A, with

one data point at 136 m CSF-A (Sample 15H-4, 0–5 cm) exhibiting especially high values. From 200 to 516 m CSF-A, methane concentrations display an overall gradual decreasing trend.

Interstitial water geochemistry

Salinity ranges from 34 to 111 (Figure **F18**). From 0 to ~50 m CSF-A, salinity values remain constant with a value of around 35, similar to modern seawater. Deeper than 50 m CSF-A, salinity values increase gradually until ~240 m CSF-A. Deeper than 240 m CSF-A, salinity values remain relatively constant and range from 103 to 111. Alkalinity at Site U1463 is low with values ranging from a high of 3.97 mM at the surface and gradually decreasing with increasing depth to a low of 0.77 mM near the bottom of the hole. pH ranges from 7.3 to 8 and displays decreasing values from the surface to ~200 m CSF-A and subsequently slightly increasing values toward the bottom of the hole.

Similar to the salinity trend, sodium, chloride, bromide, calcium, sulfate, and magnesium all display relatively constant values shallower than ~50 m CSF-A, followed by gradually increasing values with increasing depth until ~240 m CSF-A, subsequently remaining relatively constant deeper than 240 m CSF-A (Figures **F18**, **F19**). Potassium remains constant in the upper 211 m and gradually increases from 10 to ~22 µM toward the bottom (Figure **F19**). Ammonium is constant at about 200 µM in the upper 50 m, followed by a rapid increase up to 1505 µM at 183 m CSF-A, and then significantly decreases to 524 µM at the bottom. Iron and phosphate concentrations are low and display little overall variability with depth (Figures **F19**, **F20**). Barium displays an overall trend of increasing concentration from 0.6 µM at the surface to 5 µM at the bottom (Figure **F20**). Boron remains constant in the upper 50 m and then gradually increases from 457 to ~1116 µM until ~240 m CSF-A, followed by a decrease to 671 µM at 355 m CSF-A, and then a slight increase toward the bottom. Lithium displays a marked increase in concentration from 24 to 139 µM in the upper 305 m and then gradually decreases to 99 µM at the bottom. Manganese was not detected in the upper 150 m and displays a similar trend to lithium deeper than 150 m CSF-A. Silicon concentration remains constant in the upper 155 m, followed by a decrease from 277 to 137 µM until ~355 m CSF-A, and then remains constant toward the bottom. Strontium concentration displays a marked increase from 90 to 865 µM until ~155 m CSF-A and then gradually decreases to 429 µM at the bottom.

As at Site U1462, the unusually high salinity at this site is likely related to the dissolution of anhydrite ($CaSO_4$), which is observed deeper than 477 m CSF-A (Unit V; see **Lithostratigraphy**). Deeper than ~50 m CSF-A, the increasing calcium and sulfate concentra-

Figure F17. Hydrocarbons present in headspace gases, Site U1463.

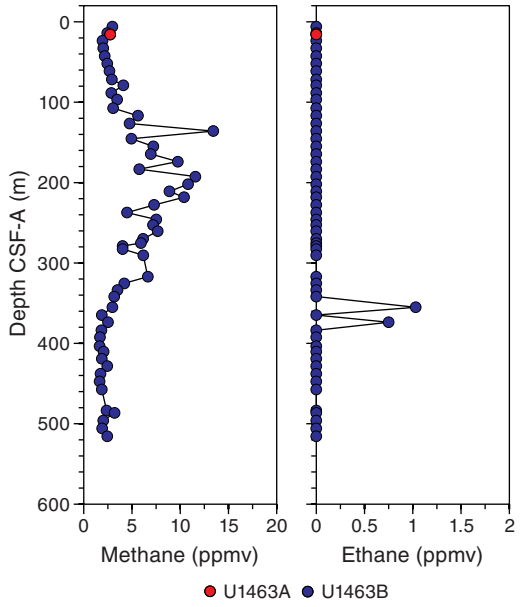

Table T13. Headspace gas contents, Site U1463. **Download table in .csv format.**

Figure F18. Alkalinity, pH, salinity, sodium, chloride, and the sodium to chloride ratio, Site U1463.

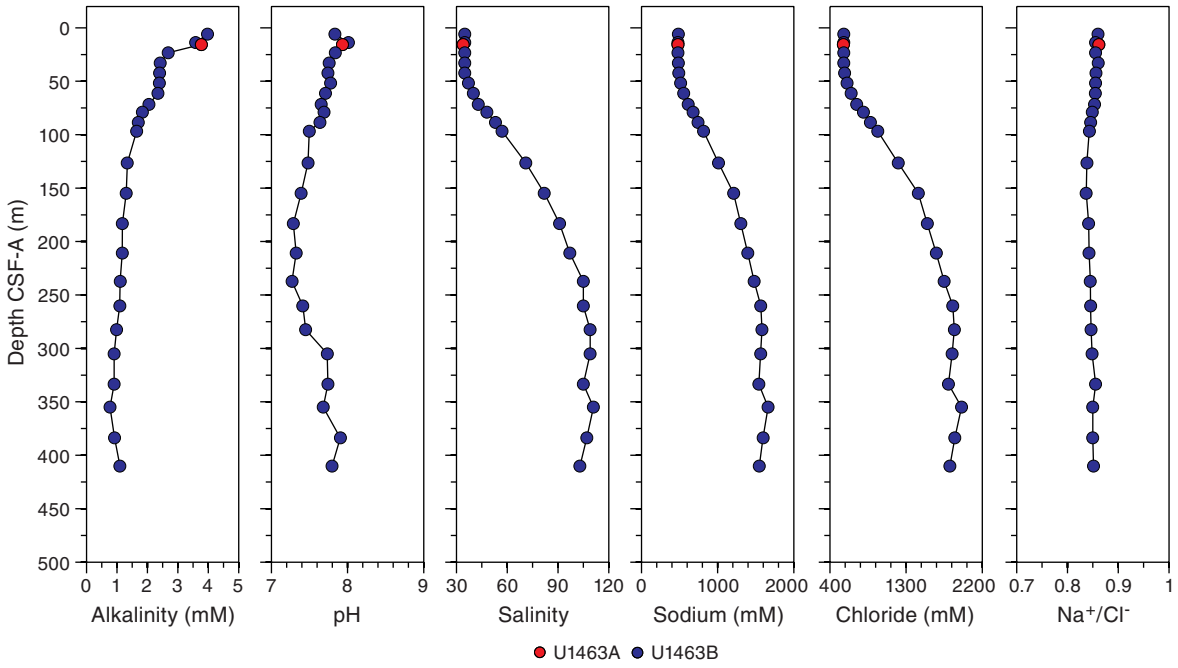

Figure F19. Major element interstitial water geochemistry (bromide, magnesium, calcium, sulfate, potassium, ammonium, and phosphate), Site U1463.

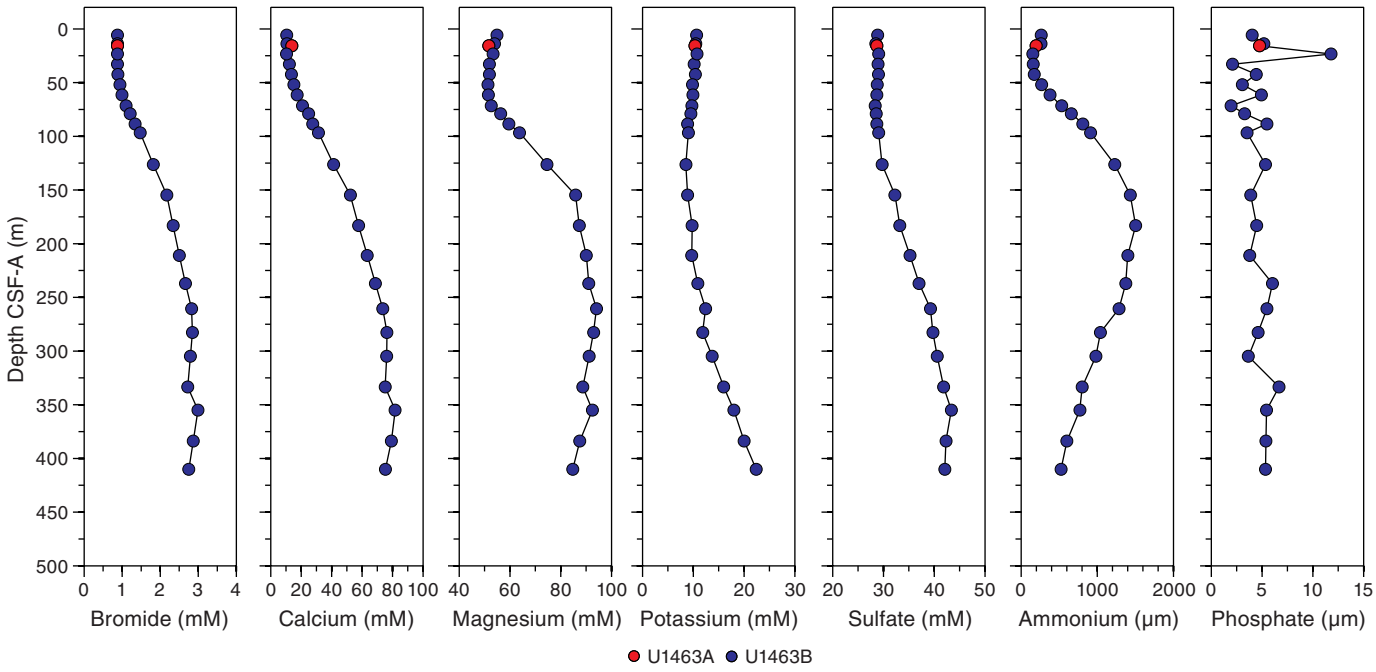

Figure F20. Minor element interstitial water geochemistry (barium, boron, iron, lithium, manganese, silicon, and strontium), Site U1463. Manganese was not detected at depths shallower than 150 m CSF-A.

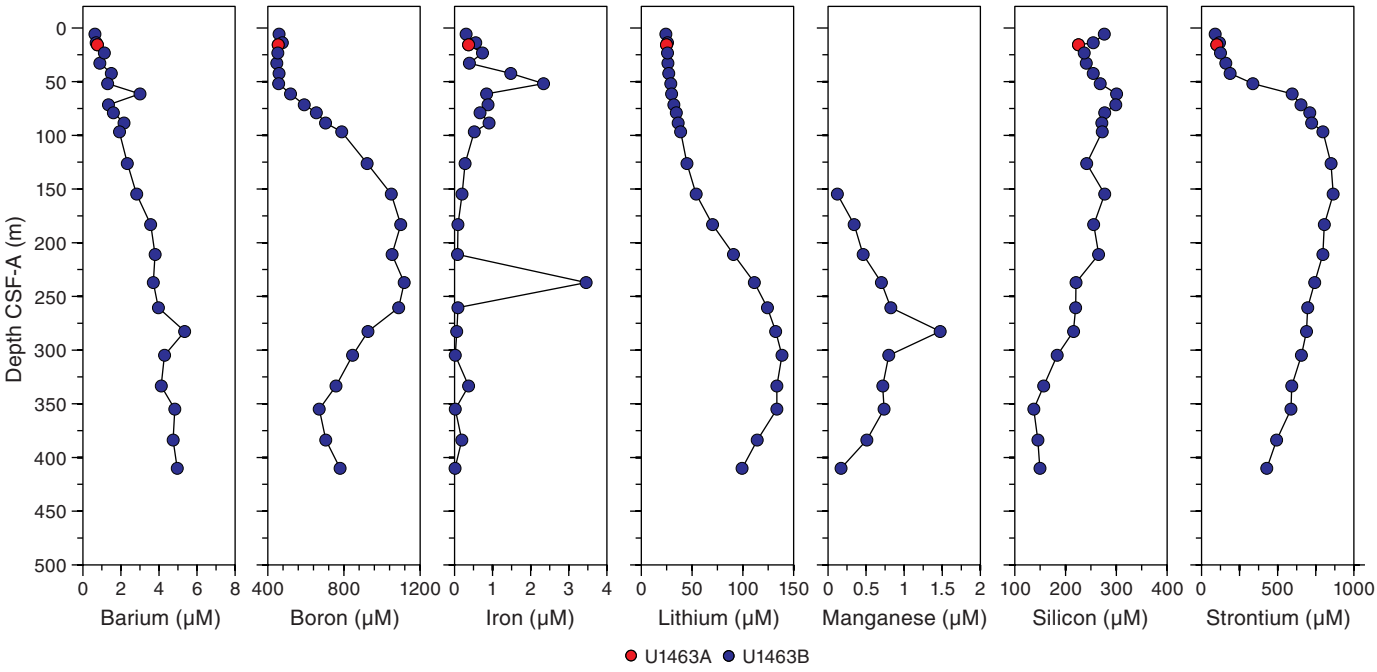

tions with increasing depth may also be related to the dissolution of anhydrite. A rapid increase in strontium concentration from 0 to 155 m CSF-A may indicate aragonite, because aragonite can contain strontium. The presence of strontium in pore water may also be related to the solubility of celestite ($SrSO_4$), which is observed in the core and likely precipitates where strontium and sulfate values are relatively high (see **Lithostratigraphy**). Thus, the decrease in strontium deeper than 155 m CSF-A may be due to the precipitation of celestite. Another major feature noted in IW geochemistry is the slight decrease in magnesium from ~260 m CSF-A, indicating the formation of dolomite, which is present in this site (see **Lithostratigraphy**).

Bulk sediment geochemistry

Calcium carbonate content ranges from 56.2 to 96.9 wt% with a mean of 77.5 wt% (Figure **F21**). An overall trend of gradually decreasing calcium carbonate is noted from ~80 m CSF-A (96.9 wt%) to ~350 m CSF-A (59.2 wt%). Deeper than 350 m CSF-A, calcium

Figure F21. Bulk sediment geochemistry (calcium carbonate, TOC, and TN), Site U1463.

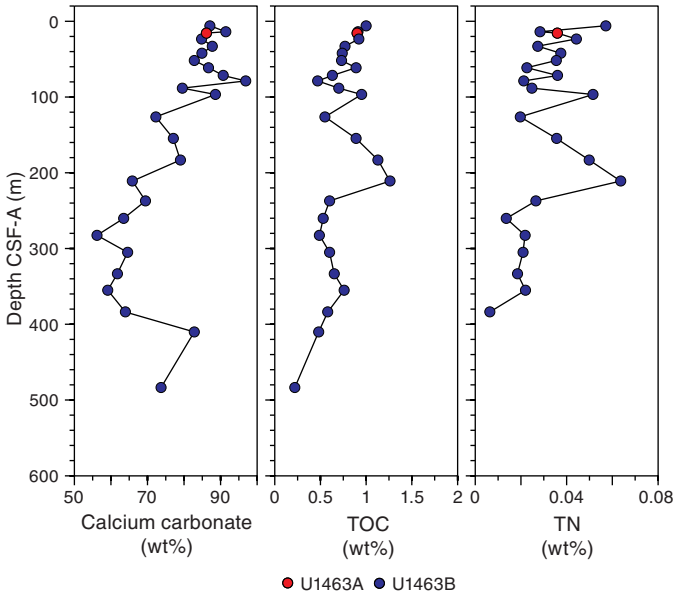

carbonate content increases to ~80 wt%. TOC ranges from 0.2 to 1.3 wt% with a mean of 0.7 wt%. The highest TOC content is at 211 m CSF-A, whereas the lowest TOC content is at 484 m CSF-A. TN contents are below detection level at the bottom of the hole (410–483 m CSF-A). Where TN content is detected, values are low, ranging from 0.006 to 0.064 wt% with a mean of 0.031%.

Paleomagnetism

Paleomagnetism investigations at Site U1463 focused on natural remanent magnetization (NRM) and alternating field (AF) demagnetization measurements. Superconducting rock magnetometer (SRM) results are reported from cores recovered with APC and XCB coring systems from 0 to 390 m CSF-A from Holes U1463B and U1463C. Magnetostratigraphic data for Hole U1463C show evidence that the Gauss/Gilbert boundary (3.596 Ma; Gradstein et al., 2012) occurs at ~282 m CSF-A. In addition, it is possible that the transition between Chron C3n and C3r intervals (5.235 Ma; Gradstein et al., 2012) occurs at ~375 m CSF-A because it corresponds with a biostratigraphic datum of 5.59 Ma at ~392.5 m CSF-A (see **Biostratigraphy and micropaleontology**).

Rock magnetic measurements of 11 discrete samples taken from Holes U1463B and U1463C included isothermal remanent magnetization (IRM) and backfield IRM acquisition, bulk susceptibility, and AF demagnetization of saturation IRM (SIRM) measurements. Two out of three discrete samples selected for IRM acquisition reached SIRM at ~100–200 mT, and one exceptional sample did not reach saturation in an impulse peak field of 1.2 T. Backfield IRM acquisition measurements yielded remanent coercivity values between 35 and 75 mT.

Archive-half measurements

Archive-half core sections from Holes U1463B and U1463C were measured on the SRM to construct the magnetostratigraphy for Site U1463 (Figures **F22**, **F23**; Table **T14**). AF demagnetization results from Hole U1463B (Figure **F22**) show intensity values that

Figure F22. Magnetostratigraphic data set, Hole U1463B. Magnetic inclination and intensity data from archive-half sections measured on the SRM after background and tray correction. Measurements from the tops and bases of sections were omitted (see **Paleomagnetism** in the Expedition 356 methods chapter [Gallagher et al., 2017a]).

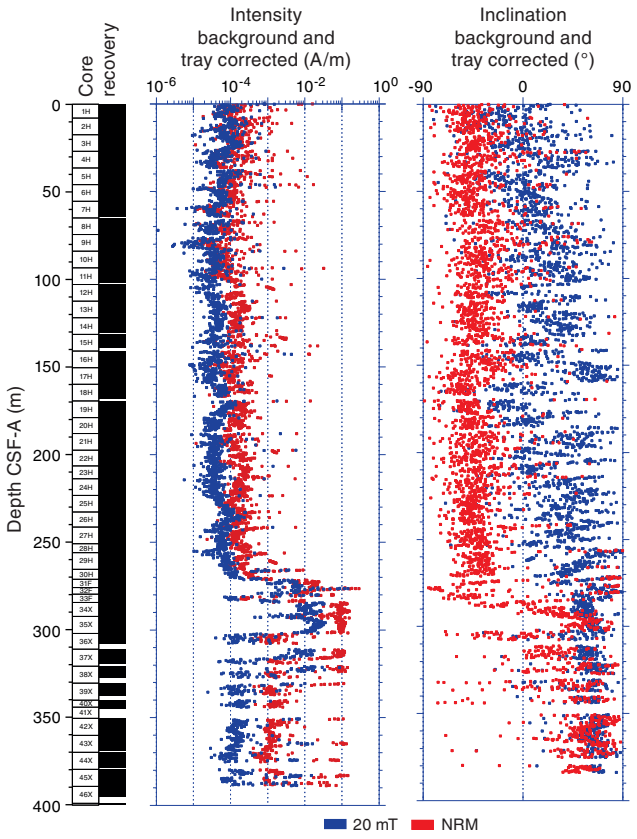

decrease by about one order of magnitude from NRM values. Measured values ranged from 10^{-5} to 10^{-2} A/m in the upper 0 to ~275 m CSF-A, and from 10^{-4} to 10^{-1} A/m from ~275 to ~485 m CSF-A. Declination values from Cores 356-U1463C-2H through 31H (~7.6–275.8 m CSF-A) were corrected using data provided by the Icefield MI-5 orientation tool (see the **Expedition 356 methods** chapter [Gallagher et al., 2017a]). In order to distinguish reversal trends throughout the succession, we estimated the expected magnetic inclination for the latitude of Hole U1463C (18°57.9295′S) based on the geocentric axial dipole model (about –34.5°).

In the upper two-thirds of Hole U1463B (0–275 m CSF-A), NRM inclination values show primarily negative values compared to shallower and mostly positive values measured after AF demagnetization. Inclination values from ~275 to ~290 m CSF-A show a striking transition where NRM inclination values swing from steeply negative values to steeply positive values. Intensity values are also higher beginning at the same depth, ~275 m CSF-A, and continues to the base of the hole (~485 m CSF-A). The transition at ~290 m CSF-A could be related to observed lithologic changes (see **Lithostratigraphy**) from partially lithified mudstones to wackestones and visible patches of disseminated pyrite.

Based on results obtained from SRM measurements on the archive-half sections from Hole U1463B, we modified our standard AF demagnetization procedures for Hole U1463C. Archive-half sections from Cores 356-U1463C-1F through 9H (upper 83 m CSF-

Figure F23. Magnetostratigraphic data set, Hole U1463C. Magnetic inclination, declination, and intensity data with different color data points representing different demagnetization steps of measurements from the same hole. Results are from archive-half sections measured on the SRM after background and tray correction with polarity (black = normal, white = reversed, gray = unidentified) and shown with biostratigraphic datums for reference. Measurements from the tops and bases of sections were omitted (see **Paleomagnetism** in the Expedition 356 methods chapter [Gallagher et al., 2017a]).

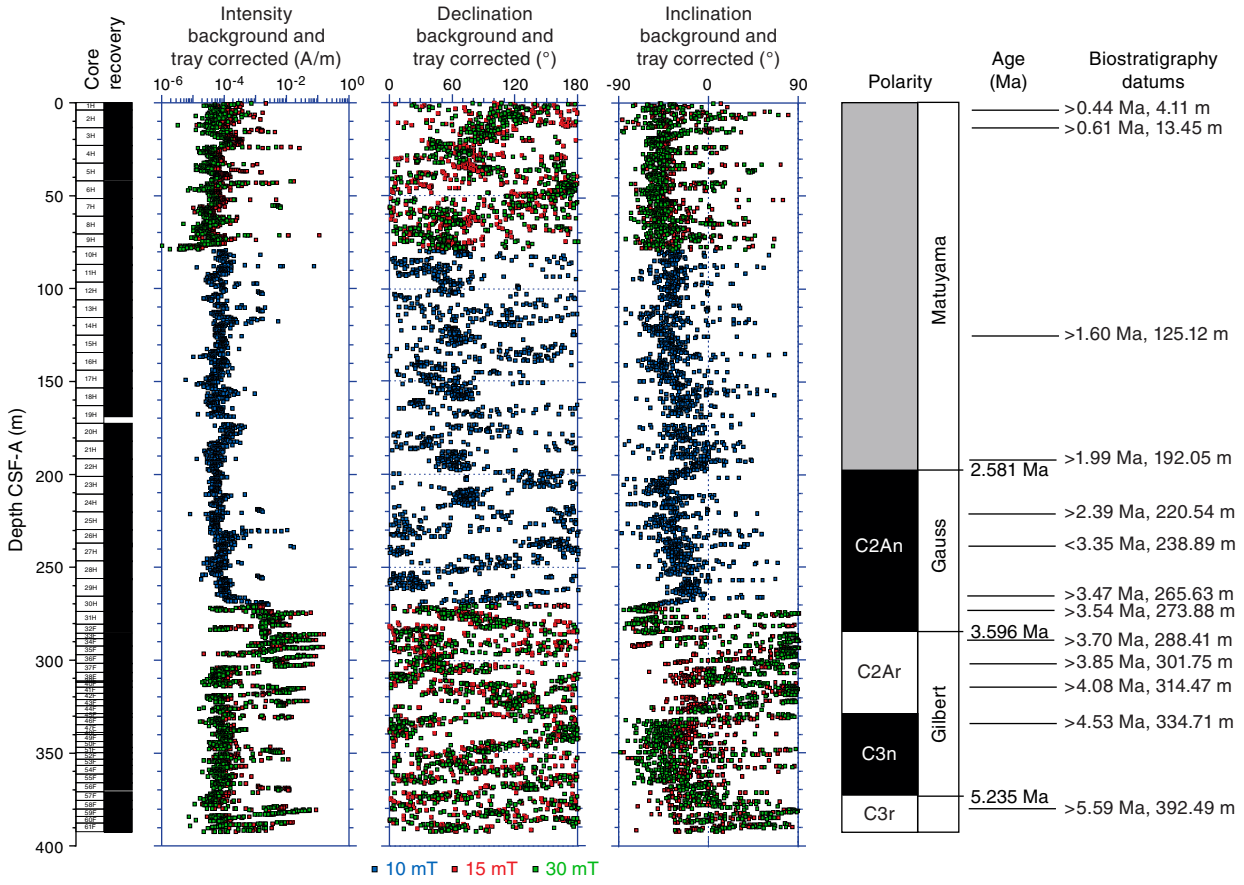

Table T14. Core or sample intervals and correlative magnetozones, Hole U1463B discrete samples and Hole U1463C archive-half measurements. Polarity and time interval from Gradstein et al. (2012). **Download table in .csv format.**

Core, section, interval (cm)	Depth CSF-A (m)	Polarity, age, and chron
Higher confidence		
356-U1463C-		
31H through 32F	270–282	Normal; Gauss C2An (2.581–3.596 Ma)
32F through 42F	282–320	Reversed; Gilbert C2Ar (3.596–4.187 Ma)
42F through 56F	320–370	Normal; Gilbert C3n (4.187–5.235 Ma)
56F through 61F	370–392	Reversed; Gilbert C3r (5.235–6.033 Ma)
Lower confidence		
356-U1463B-		
1H-3, 80–82, through 33F-2, 80–82	40.19–282	Normal; Gauss C2An (2.581–3.596 Ma)
37X-1, 86–88	311.96	Normal; Gilbert C3n (4.187–5.235 Ma)
43X-4, 59–61; 46X-1, 75–77; and 55X-2, 120–122	365.39–479.4	Reversed; Gilbert C3r (5.235–6.033 Ma)

A of Hole U1463C) were measured after stepwise AF demagnetization at 0, 15, and 30 mT (Figure **F23**) to characterize demagnetization behavior. Comparisons between the demagnetization steps show that demagnetization at 15 and 30 mT results in steeply negative inclination values. We demagnetized the sections using lower peak fields of 0, 5, and 10 mT for Hole U1463C cores until Section 30H-4 (~270 m CSF-A) in hopes that it would yield more detailed directional data. However, deeper than ~270 m CSF-A, we returned to the original demagnetization sequence (peak fields of 0, 15, and 30 mT) because of the evidence for high-coercivity material in the lower third of Hole U1463B. Directional data from the lower third of Hole U1463C shows negative (normal) inclination values after 15 and 30 mT AF demagnetization from ~275 m CSF-A to the bottom of the hole at 390 m CSF-A. We attribute this difference to a more accurate determination of characteristic remanent magnetization (ChRM) after demagnetization at higher steps.

Discrete sample measurements

A total of 11 discrete samples from Hole U1463B underwent AF demagnetization, of which four (Samples 356-U1463B-9H-2, 85–87

cm, 33F-2, 80–82 cm, 37X-1, 86–88 cm, and 55X-2, 120–122 cm) were investigated further for rock magnetic characteristics using IRM and backfield IRM acquisition measurements, as well as bulk susceptibility. IRM acquisition curves (Figure **F24**) indicate that Sample 9H-2, 85–87 cm, reached SIRM at low fields (~100–200 mT), which is commonly attributed to the presence of magnetite and/or titanomagnetite (Dunlop and Özdemir, 1997). Samples 33F-2, 80–82 cm, and 37X-1, 86–88 cm, from Hole U1463B did not reach SIRM within the limit of shipboard analysis (~1.2 T), suggesting the presence of high-coercivity phases. The differences between these two samples are noteworthy: Sample 33F-2, 80–82 cm, reached a magnetization intensity of 3.34×10^{-1} A/m, whereas Sample 37X-1, 86–88 cm, reached a value an order of magnitude higher, 3.28 A/m. Backfield IRM acquisition curves were performed for three samples (9H-2, 85–87 cm, 33F-2, 80–82 cm, and 55X-2, 120–122 cm), and their remanent coercivity values are ~74, ~75, and ~35 mT, respectively. Sample 37X-1, 86–88 cm, also underwent AF demagnetization after IRM acquisition up to 1.2 T and provided a median destructive field value of between 30 and 40 mT (Figure **F25**).

Bulk magnetic susceptibility measurements (Table **T15**) were conducted for all of the discrete samples taken from Hole U1463B using the KLY 4S Kappabridge (AGICO, Inc.). Results ranged from 4.40×10^{-6} to 140.68×10^{-6} SI units, with the exception of the shallowest (Sample 1H-3, 80–82 cm; 3.8 m CSF-A) and deepest (Sample 55X-2, 120–122 cm; 479.4 m CSF-A) samples, which exhibited diamagnetic behavior (negative susceptibility values). Sample bulk susceptibility measurements, at 282 and 311.96 m CSF-A, exhibited an increasing trend that is similar to the one observed for equivalent measurements on the whole-round and split cores (see **Physical properties**) between 270 and 310 m CSF-A.

Figure F24. IRM acquisition curves for four discrete samples from Hole U1463B and their respective backfield curves. Inset shows enlarged view of negative *x*-axis, showing the coercivity of remanence estimation for each sample.

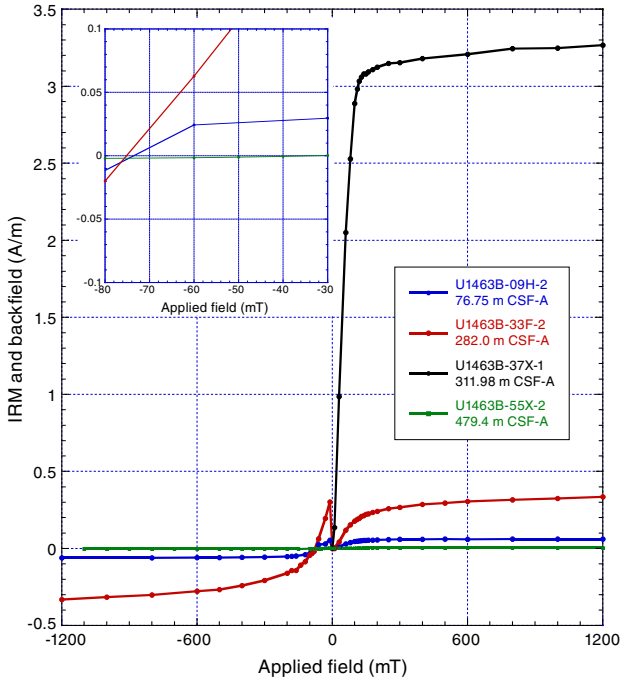

Figure F25. IRM curve and corresponding AF demagnetization trend, Sample 356-U1463B-37X-1, 86–88 cm (311.96 m CSF-A).

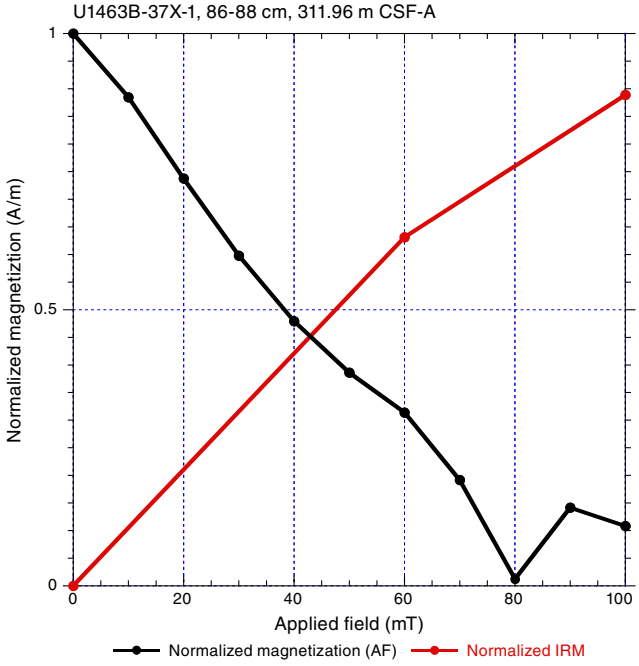

Table T15. Results of principal component analysis (PCA), together with NRM intensity and bulk susceptibility, for discrete samples, Hole U1463B. χ = bulk susceptibility, *D* = declination, *I* = inclination, MAD = maximum angular deviation. **Download table in .csv format.**

Core, section, interval (cm)	Top depth CSF-A (m)	NRM intensity (10^{-3} A/m)	χ (10^{-6} SI)	Component 1				Component 2			
				D (°)	*I* (°)	MAD (°)	PCA range (mT)	*D* (°)	*I* (°)	MAD (°)	PCA range (mT)
356-U1463B-											
1H-3, 80–82	3.82	0.081	–3.29	174.2	–22.6	13.3	30, 40, 50, 60				
5H-3, 79–81	40.19	0.102	4.40	144.5	–13.9	10.6	20, 30, 40	178.8	–20.0	7.3	40–70
9H-2, 85–87	76.77	0.076	10.32	162.9	–12.2	5.9	NRM to 20	169.1	–26.3	8.9	70–100
14H-3, 74–76	125.64	0.141	15.22	92.5	–66.5	6.4	20–40				
20H-3, 60–62	182.48	0.106	18.64	153.3	–14.1	7.4	20–50				
26H-2, 90–92	235.20	0.249	20.61	240.7	–37.1	8.7	10–30, 50				
33F-2, 80–82	282.00	0.199	49.21	218.7	–44.8	13.2	10–70				
37X-1, 86–88	311.96	45.500	140.68	197.1	51.1	14.8	10–50	190.0	18.9	4.0	60–100
43X-4, 56–61	365.39	0.876	49.90	223.6	63.9	12.1	NRM, 10	233.5	–35.2	22.5	20–60, 80
46X-1, 75–77	390.15	0.250	18.20	19.7	–36.7	35.0	20, 30, 50, 70, 80				
55X-2, 120–122	479.40	0.065	–5.11	290.3	–61.7	23.8	30, 40, 50				

Magnetostratigraphy

AF demagnetization steps up to 100 mT were used to measure discrete samples from Hole U1463B (Figure **F26**; Table **T15**) to get an overview of the demagnetization behavior and possible trends in the archive-half results. Discrete samples from 40.19 to ~282 m CSF-A (Samples 356-U1463B-1H-3, 80–82 cm, through 33F-2, 80–82 cm) in Hole U1463B (Table **T15**) had negative inclination values that suggest normal polarity. Sample 37X-1, 86–88 cm, at 311.96 m CSF-A shows a pattern of steeply inclined positive values that decrease in the same direction with each demagnetization step, becoming negative after 60 mT and trending toward the origin. The ChRM for this sample, therefore, may also reflect normal polarity, representing Chron C3n (4.187–5.235 Ma) with a reversed overprint corresponding to Chron C2An (2.581–3.596 Ma). The three deepest discrete samples (43X-4, 59–61 cm [365.39 m CSF-A], 46X-1, 75–77 cm [390.15 m CSF-A], and 55X-2, 120–122 cm [479.4 m CSF-A]) have weak but positive inclination NRM values. These three samples fall below biostratigraphic datums at 3.70, 5.59 (386.22 m CSF-A), and 5.94 Ma (412.44 m CSF-A), respectively. This most likely correlates the interval from 365 to 479 m CSF-A in Hole U1463B with Chron C3r (5.235–6.033 Ma). However, magnetostratigraphic interpretations based on low-resolution discrete samples alone should not be considered definitive.

Magnetostratigraphic data from archive-half measurements from Hole U1463C (Figure **F23**; Table **T14**) may encompass the Gauss/Gilbert boundary and adjacent magnetozones. The high-intensity interval between Cores 356-U1463C-30H and 42F (265.6 and 321.2 m CSF-A) indicates a prominent bias of inclination data toward positive values, corresponding to reversed polarity. Correlation with the previously mentioned biostratigraphic datums of 3.54 (276.11 m CSF-A) and 3.70 Ma (293.74 m CSF-A), suggest that this interval represents the upper part (Chron C2Ar) of the Gilbert Chron. Another reversed polarity interval at ~370–392 m CSF-A in Hole U1463C may correlate with Chron C3r (5.235–6.033 Ma), again using the biostratigraphic constraint of 5.59 Ma at 392.49 m CSF-A.

Figure F26. AF demagnetization results for discrete samples from 4 depths, Hole U1463B. Orthogonal projection (Zijderveld diagram) and equal area projection of NRM vector measured after each demagnetization treatment. Horizontal = declination, vertical = inclination. Equal area projection: solid circles = positive inclination, open circles = negative inclination. Normalized magnetization behavior plots show highest magnetization intensity (M_{max}) = 1 on *y*-axis with AF demagnetization strengths shown after each measurement on *x*-axis.

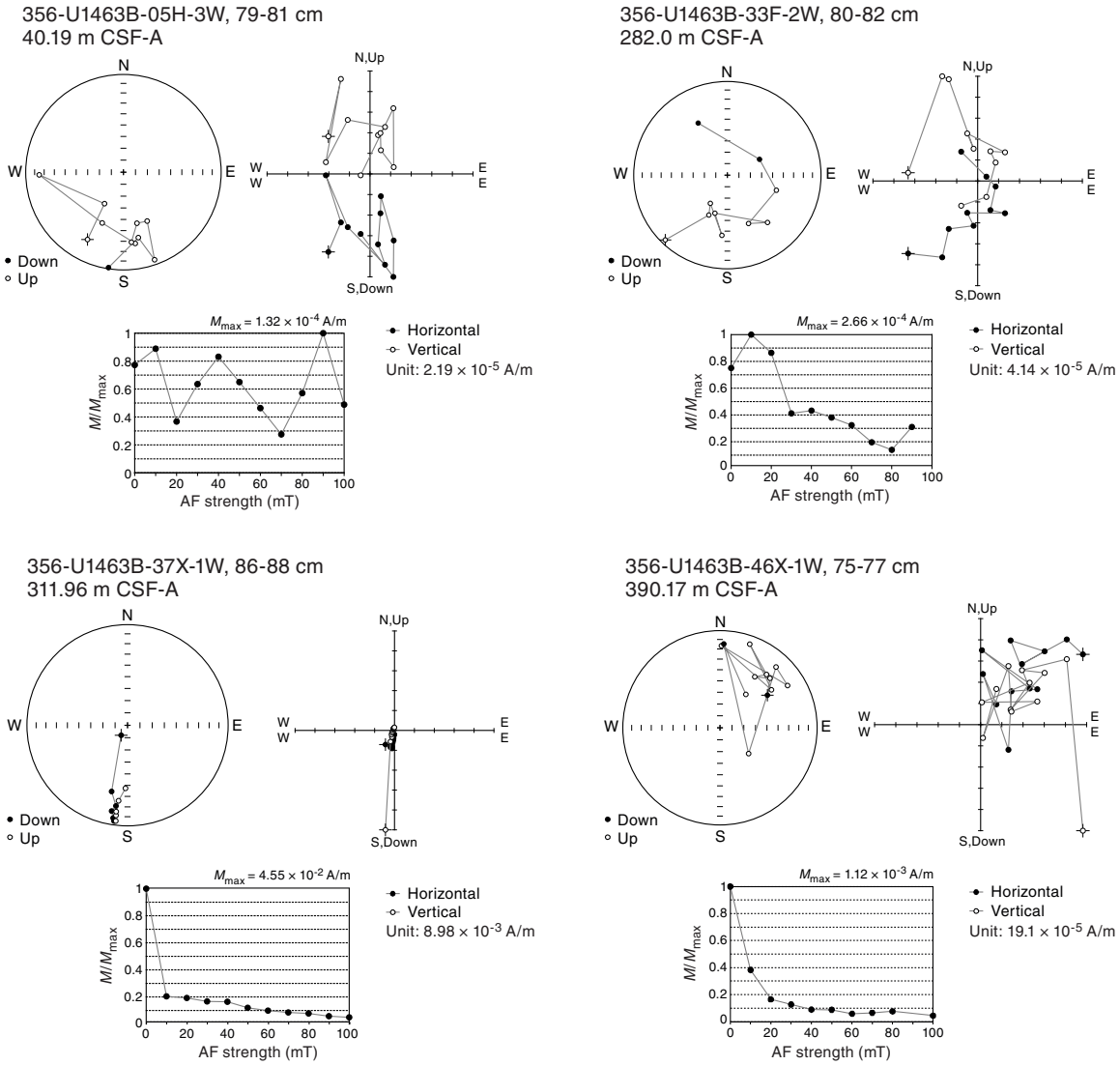

Physical properties

Physical properties measurements were performed using the Whole-Round Multisensor Logger (WRMSL), NGR sensor, and discrete sampling on cores. NGR measurements revealed similar trends and variations in all holes. MS values revealed 10–20 m scale variability, with maximum amplitude (about 30 SI) from 270 to 330 m CSF-A. MS patterns are consistent between holes and between the WRMSL and the Section Half Multisensor Logger (SHMSL). Variability at the 10–20 m scale was also observed in NGR and *P*-wave velocity as measured on the WRMSL, and was verified through discrete measurements. *P*-wave velocity increases from about 1500 to 1900 m/s in the top 300 m. From 300 to 390 m CSF-A, discrete measurements of *P*-wave velocity show diverging trends between Holes U1463B (XCB cores) and U1463C (APC cores). Porosity decreases from 64% to 40% at 250 m CSF-A and is scattered with a range of 13%–43% deeper than 270 m CSF-A.

Magnetic susceptibility

MS measurements were carried out on the WRMSL at 5.0 cm intervals and on the SHMSL at 2.5 cm intervals. SHMSL data were obtained by averaging two measurements per position, except for the interval between Core 356-U1463D-21H (179.9 m CSF-A) and the base of Hole U1463D, where only one measurement was made per position. MS values on the WRMSL between the top of the hole and 255 m CSF-A increase from ~1 to 5 SI. Deeper than 270 m CSF-A, 10 m scale variability is seen with approximately 20 SI amplitude (Figure **F27**). At 330 m CSF-A, the variability decreases; however, several peaks (up to 20 SI) are observed between 360 and 390 m CSF-A. All of these trends and variations are similar in all holes as well as in the SHMSL readings, even after decreasing the resolution on the SHMSL for the lower half of Hole U1463D. In Hole U1463B, the MS values decrease to 0 SI at the bottom of the hole.

Natural gamma radiation

NGR was measured on whole-round cores at 20 cm intervals in Hole U1463A. Measurements in Holes U1463B, U1463C, and U1463D were taken at 20 cm intervals from the surface to Cores 356-U1463B-31F, 356-U1463C-31H, and 356-U1463D-31H, respectively. Below these intervals, measurements were taken at 10 cm intervals. NGR values tend to be relatively low in the top 10 m (Figure **F27**). This corresponds with lithostratigraphic Unit I, which is composed of relatively pure aragonite mud (see **Lithostratigraphy**). The lack of a terrestrial component, including clays, explains the low NGR values. Variability on a 10–20 m scale is observed from the surface to 420 m CSF-A. This scale of variability is also seen in MS and in *P*-wave velocity as measured on the WRMSL (Figures **F27**, **F28**). Generally, NGR corresponds well between all four holes. However there are some discrepancies. For example, from 32 to 39 m CSF-A, NGR data from Hole U1463B show a high-amplitude

Figure F27. WRMSL MS, SHMSL point magnetic susceptibility (MSP), and NGR results, Site U1463. SHMSL data are raw MS from Hole U1463A and drift-corrected MS from all the other holes.

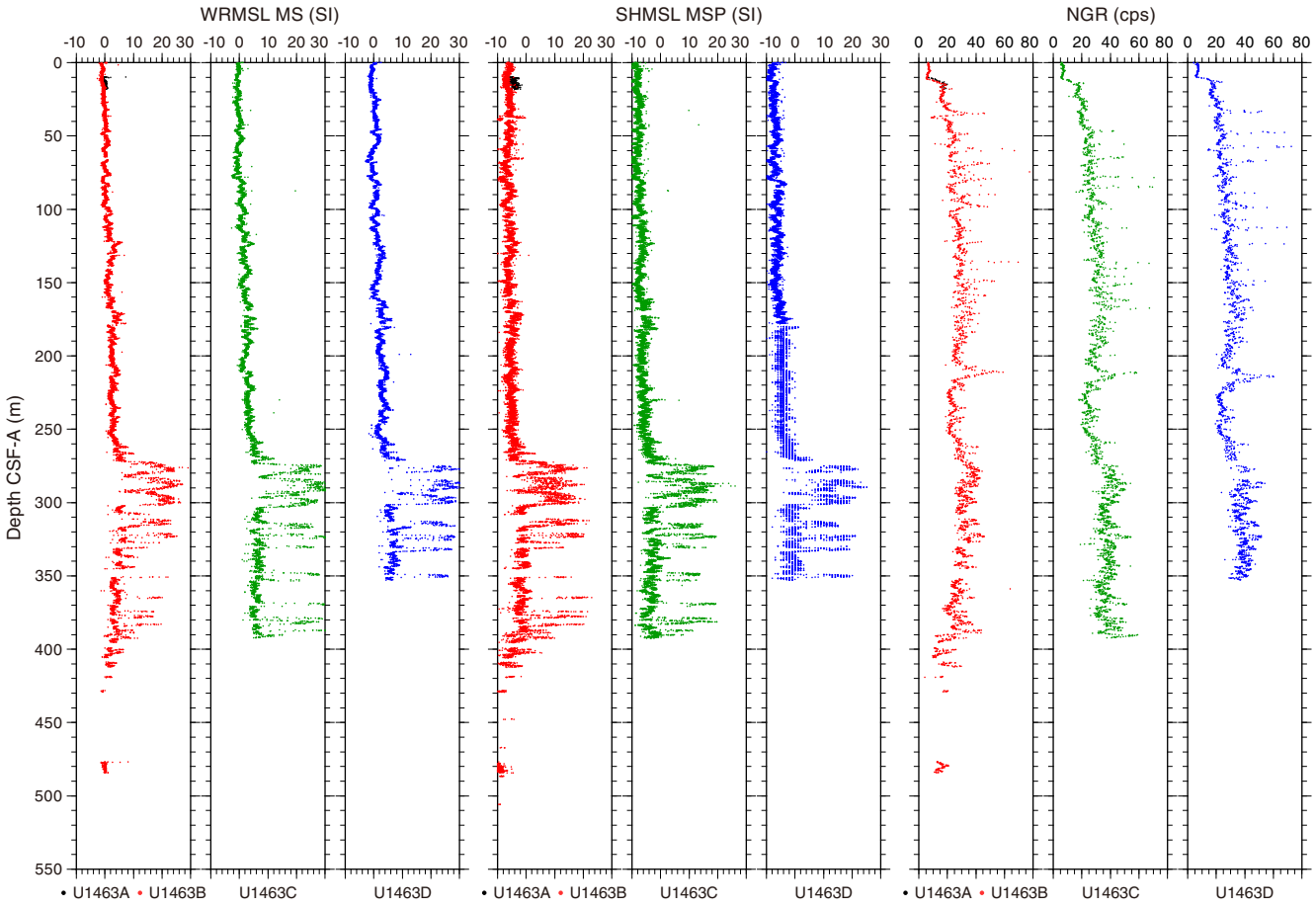

Figure F28. A. *P*-wave velocity, Site U1463 (dots = WRMSL, open circles = measured in liner, triangles = measured without liner; solid circles = MAD cubes with error bars showing ranges of their measurements taken in three orthogonal directions). Note that Hole U1463B was cored using APC shallower than 284 m CSF-A and XCB deeper than 284 m CSF-A, and Holes U1463C and U1463D were cored using APC and HLAPC only. Black = Hole U1463A, red = Hole U1463B, green = Hole U1463C, blue = Hole U1463D. Expanded view of (B) Hole U1463C and (C) Hole U1463D showing high-frequency discrete *P*-wave velocity measurements compared to WRMSL measurements. For B and C, dots = WRMSL, open circles = discrete measurements.

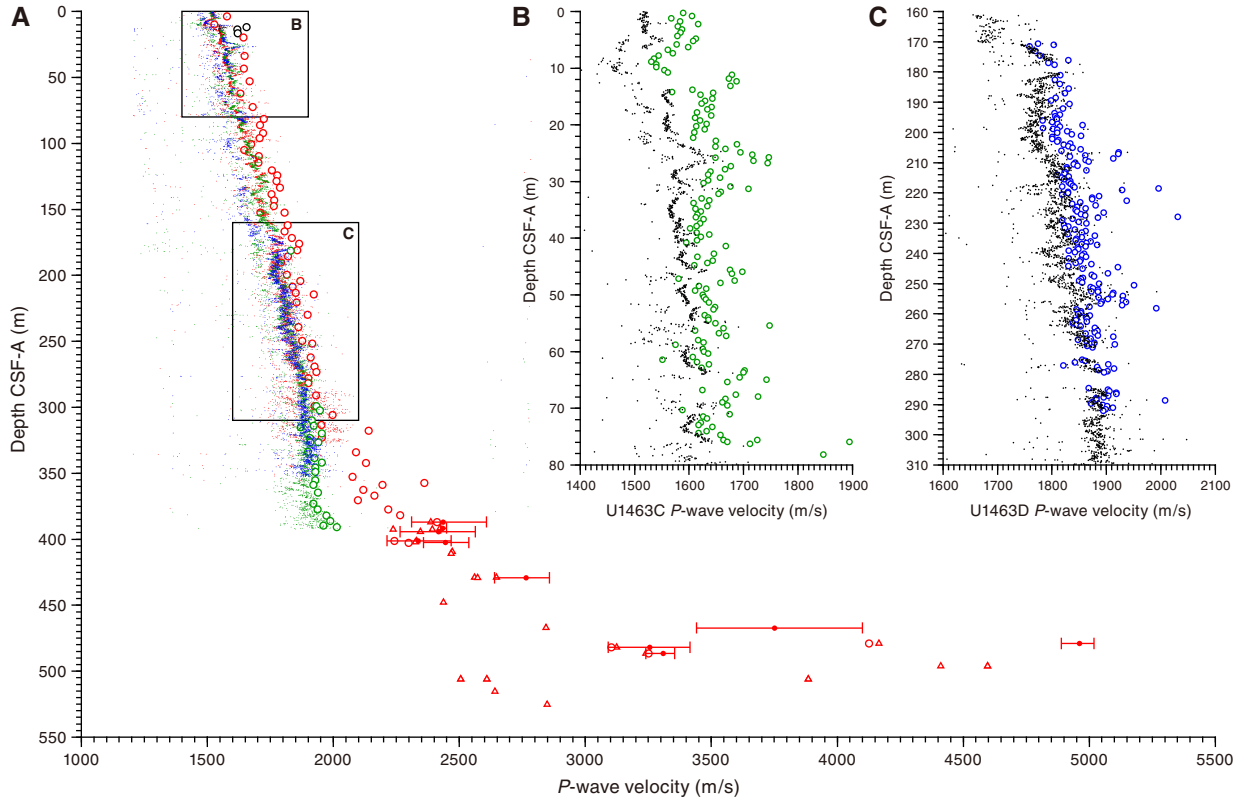

variation that rises from 20 to 47 counts/s and falls to 8 counts/s before returning to the 20 counts/s background. This swing is also seen as a 50 counts/s peak in Hole U1463D but is not observed in Hole U1463C (Figure **F27**). A prominent peak is seen at 210 m CSF-A in all holes and also in the total spectral gamma ray (HSGR) data from downhole logging (see **Downhole measurements**; Figure **F33**).

P-wave sonic velocity

P-wave velocities were measured using two different instruments: the WRMSL (5 cm intervals) in all holes and one or two discrete measurements made with the *P*-wave caliper on each core from Hole U1463B. Because of the fully filled core liners, WRMSL *P*-wave velocities showed values that were consistent with but often slightly lower than those of the discrete measurements (Figure **F28**). In the uppermost 300 m, *P*-wave velocities increase gradually from ~1500 to 1900 m/s. From 300 to 330 m CSF-A, discrete measurements continue the gradual rise, whereas in Hole U1463B the WRMSL data become scattered. However, in Holes U1463C and U1463D the WRMSL data do not show this scatter and instead show a moderate rise with low variability. From 330 to 390 m CSF-A, *P*-wave velocities measured on HLAPC cores from Hole U1463C are relatively constant at about 1900 m/s. However, discrete measurements made on XCB cores from Hole U1463B show a rapid increase in velocity with values of about 2100 m/s at 350 m CSF-A and 2600 m/s at 450 m CSF-A. All of these differences suggest a discrepancy in sonic velocity measured in APC versus XCB cores. This issue is compounded by the fact that downhole sonic velocities parallel but are higher than the velocities measured in the XCB cores of Hole U1463B (see **Downhole measurements**; Figure **F36**).

Meter-scale variability in *P*-wave velocities measured on the WRMSL was verified through high-frequency discrete measurements between Cores 356-U1463C-1H and 9H (0 and 77.6 m CSF-A) and between Cores 356-U1463D-23H and 33F (198.9 and 293.1 m CSF-A) (Figure **F28B–F28C**). These measurements were taken at three locations in each section. These discrete measurements were consistent with the variability observed in the WRMSL data. For example, the discrete measurements reproduced the shift in velocity between 10 and 15 m CSF-A and local maxima in sonic velocity at 26, 46, 208, 235, and 255 m CSF-A.

Gamma ray attenuation

Gamma ray attenuation (GRA) was measured to estimate bulk density using the WRMSL at 5.0 cm intervals. In the upper 170 m, 10–20 m scale variability, similar to that seen in NGR data, is observed (Figures **F27**, **F29**). Additional results are reported with those from discrete measurements of bulk density in **Moisture and density**, below.

Moisture and density

In Holes U1463A and U1463B, MAD measurements were taken on one or two samples per core, synchronizing with smear slides and thin sections. In Hole U1463C, additional samples were taken, one every other core from Core 356-U1463C-34F (288.4 m CSF-A)

Figure F29. Bulk density (dots = GRA, open circles = MAD), grain density, and porosity, Site U1463. Black = Hole U1463A, red = Hole U1463B, green = Hole U1463C, blue = Hole U1463D.

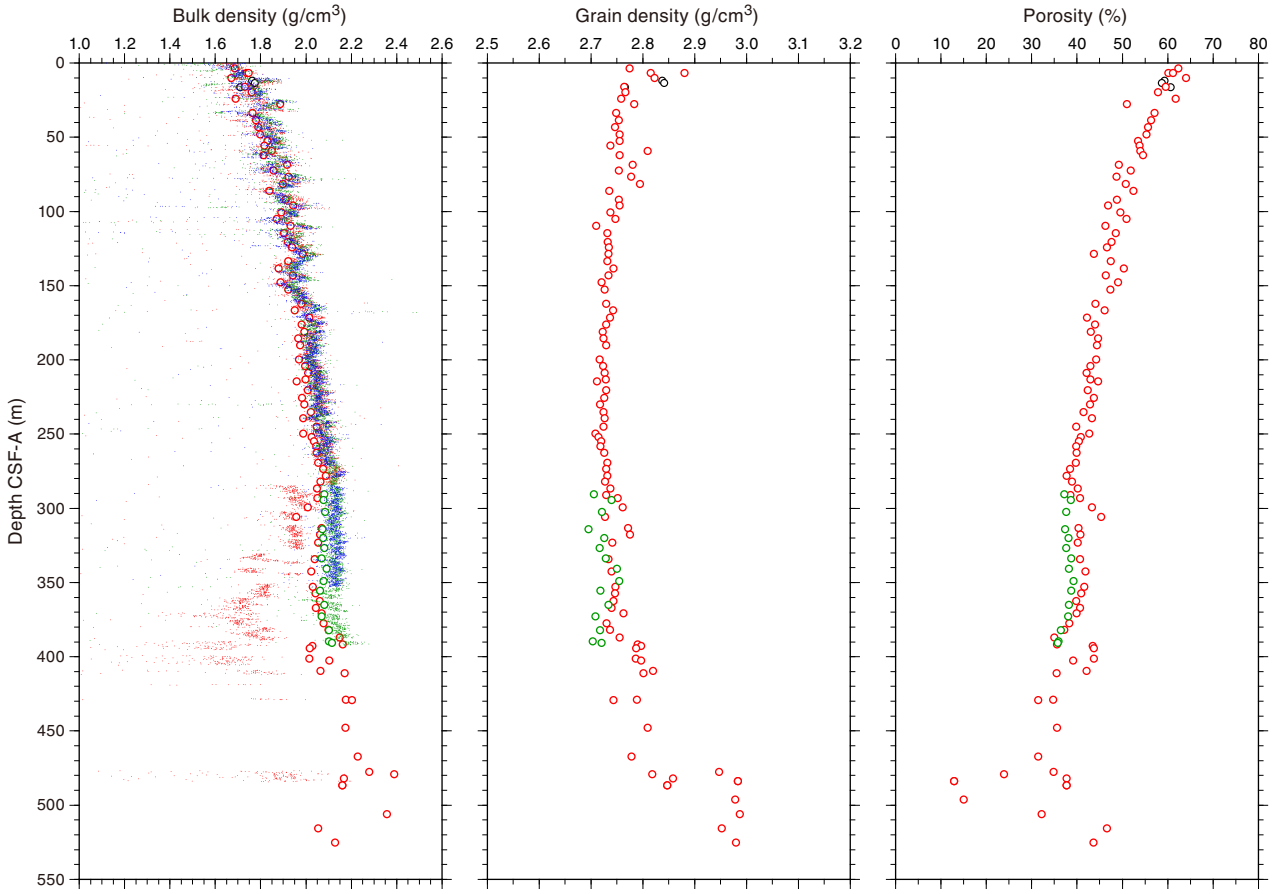

downward. MAD bulk density measurements are in agreement with bulk density estimated by GRA from the surface to about 100 m CSF-A. Deeper than 100 m CSF-A, discrete measurements tend to be slightly lower than GRA bulk density estimates, and this discrepancy increases to 285 m CSF-A in Hole U1463B. This difference in bulk density estimates is consistent with the fact that variations in the GRA coefficient (μ) are dependent on mineralogy, resulting in errors up to 5% (Blum, 1997). We see that these sediments have lower grain densities, and thus different mineral properties, compared to those from previous sites in this expedition. Our observations suggest that μ would have to decrease as grain density increases in order to correct GRA for true bulk density (see **Physical properties** in the Site U1464 chapter [Gallagher et al., 2017d] for an extended discussion). Deeper than 285 m CSF-A in Hole U1463B, coring switched from the APC to XCB system, and as a result, cores did not fill the core liner. Therefore, discrete bulk density measurements are higher than GRA bulk densities, as observed at previous sites (Figure **F29**; see for example, **Physical properties** in the Site U1461 chapter [Gallagher et al., 2017b]). APC cores in Holes U1463C and U1463D reveal relatively constant bulk densities of 2.13 g/cm³ deeper than 300 m CSF-A. This value is higher than the bulk densities generated by discrete samples. Note that at this depth discrete samples were taken in Hole U1463C to assess the differences in bulk density seen between discrete measurements in Hole U1463C and GRA bulk densities obtained from Hole U1463C. Discrete bulk densities measured in this interval (deeper than 300 m CSF-A) in Hole U1463C (HLAPC cores) were higher than those seen in Hole U1463B (XCB cores) but remain lower than the GRA bulk densities from Holes U1463C and U1463D. This again points to an effect related to HLAPC/APC versus XCB coring.

Porosity shows a decreasing trend from about 64% at the surface to about 40% at 250 m CSF-A (Figure **F29**). Porosity remains at about 40% to 390 m CSF-A. Deeper than 390 m CSF-A to the bottom of Hole U1463B (530 m CSF-A), porosity becomes variable, with values ranging from 13% to 47%. Porosity measured on cores from Hole U1463C (290–390 m CSF-A) is slightly lower than that measured on those from Hole U1463B at the same depth interval. This is consistent with the slightly higher bulk densities in Hole U1463C in the same interval. It should be noted that correction for increased pore water salinity raises the absolute value of porosity by up to 1.4% (at about 300 m CSF-A), which is a relative increase of 3.1%. High pore water salinity also increases the bulk density by as much as 0.011 g/cm³, which is, however, insufficient to account for the discrepancy between MAD and GRA bulk density estimates from 100 to 285 m CSF-A.

In the upper 10 m, grain densities are relatively high, with values ranging from 2.76 to 2.88 g/cm³ (Figure **F29**), corresponding to lithostratigraphic Unit I, which is rich in aragonite with a mineral density of 2.94 g/cm³ (see **Lithostratigraphy**). These values also correspond to the low in NGR counts seen in all holes, as described above. At greater depths at the site, grain densities decrease to 2.73 g/cm³ at 110 m CSF-A. Densities remain between 2.71 and 2.74

g/cm³ to 390 m CSF-A. The dominant mineralogy in this interval is calcium carbonate (mineral density = 2.71 g/cm³, see **Lithostratigraphy** for lithologies). Deeper, grain densities are variable, ranging between 2.74 and 2.98 g/cm³. These rocks contain considerable amounts of dolomite and some celestite and anhydrite (grain density of 2.85, 3.97, and 2.98 g/cm³, respectively; see **Lithostratigraphy** for lithologies).

Discrete stress measurement

Discrete measurements of shear and normal stress were taken in Hole U1463B. The measurements were taken where the sediments were soft enough to use the handheld Torvane and the pocket penetrometer. In the top 300 m, normal stress values increase from 0 to ~500 N/m². Shear strength values also increase to ~600 N/m² at 250 m CSF-A. However, the shear strength values increase rapidly up to ~1800 N/m² at 260 m CSF-A and decrease to ~1000 m/s at 300 m CSF-A (Figure **F30**).

Reflectance spectroscopy and colorimetry

Reflectance spectroscopy and colorimetry was performed on the archive halves of the split core sections at 2.5 cm intervals. Reflectance (L*), red versus green (a*), and blue versus yellow (b*) were measured on all cores. Abrupt shifts in colorimetry were observed at different depths in Holes U1463B and U1463C (Figure **F31**). These shifts exactly corresponded to noon or midnight and changes in scientific personnel. We reran several sections that showed this abrupt operator-related color anomaly and failed to reproduce it. By experimenting with different amounts of plastic cover, from no plastic to two layers of plastic, it became clear that this was the source of the anomalies. Scientists had been using plastic to cover the wettest cores and measuring drier cores without plastic, but not in a consistent manner between shifts. An effort was made to correct this error in Hole U1463C by remeasuring the affected cores. However, we only interpret the colorimetry record of Hole U1463D, where colorimetry measurements were made consistently using a single layer of plastic on all cores. L* and b* from Hole U1463D show a general decreasing trend throughout the cored interval, whereas a* fluctuates around 0. Superimposed on these trends are 10–20 m scale variations that seem to correspond well to those seen in NGR (Figures **F27**, **F31**).

Thermal conductivity, temperature, and heat flux

Thermal conductivity was measured in Holes U1463B and U1463C using two different devices: the needle shallower than 285 m CSF-A and the minipuck deeper. A steady increase in thermal conductivity from 0.97 to 1.7 W/(m·K) occurs from the surface to about 320 m CSF-A. At greater depths at the site, measurements of thermal conductivity become scattered and unreliable (Figure **F32D**).

We measured the in situ temperature with the APCT-3 during piston coring in Hole U1463C. Measurements were made in Cores 356-U1463C-4H, 7H, 10H, 13H, 16H, and 20H. We were not able to estimate the temperature at the seafloor with confidence from the temperature logs. The shallowest estimate of temperature was at 32.51 m CSF-A (23.01°C). The deepest temperature reading was taken at 182.24 m CSF-A (30.88°C) (Figure **F32A**). Inspection and extrapolation of these temperature records suggest that they are all of good to excellent quality, except for the shallowest temperature estimate in Core 4H (32.51 m CSF-A). This measurement showed some apparent heating after about 1 min, but we were able to use the early part of the cooling curve to make a reasonable estimate of the in situ temperature. The temperature measurements define a geothermal gradient with little deviation from linearity. The resulting gradient is 51.9°C/km. From the thermal conductivities measured in cored material (Figure **F32B**) we were able to estimate a geothermal heat flux of 65.3 mW/m². The Bullard plot shows a linear relationship between temperature and thermal resistance (Figure **F32C**) (see **Physical properties** in the Expedition 356 methods chapter [Gallagher et al., 2017a]). Therefore, we are confident that the temperature profile has not been perturbed by fluid flow or internal heat production.

Figure F30. Penetrometer strength and Torvane shear strength results, Hole U1463B.

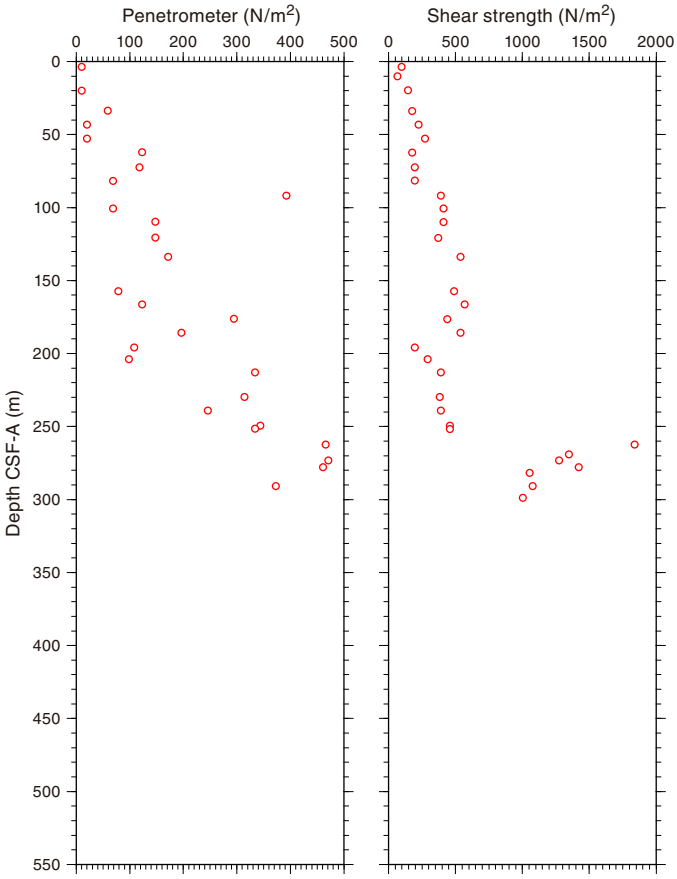

Figure F31. Reflectance spectroscopy and colorimetry (L*, a*, and b*), Site U1463. Hole U1463C data were corrected by rescanning affected core sections (see text for details).

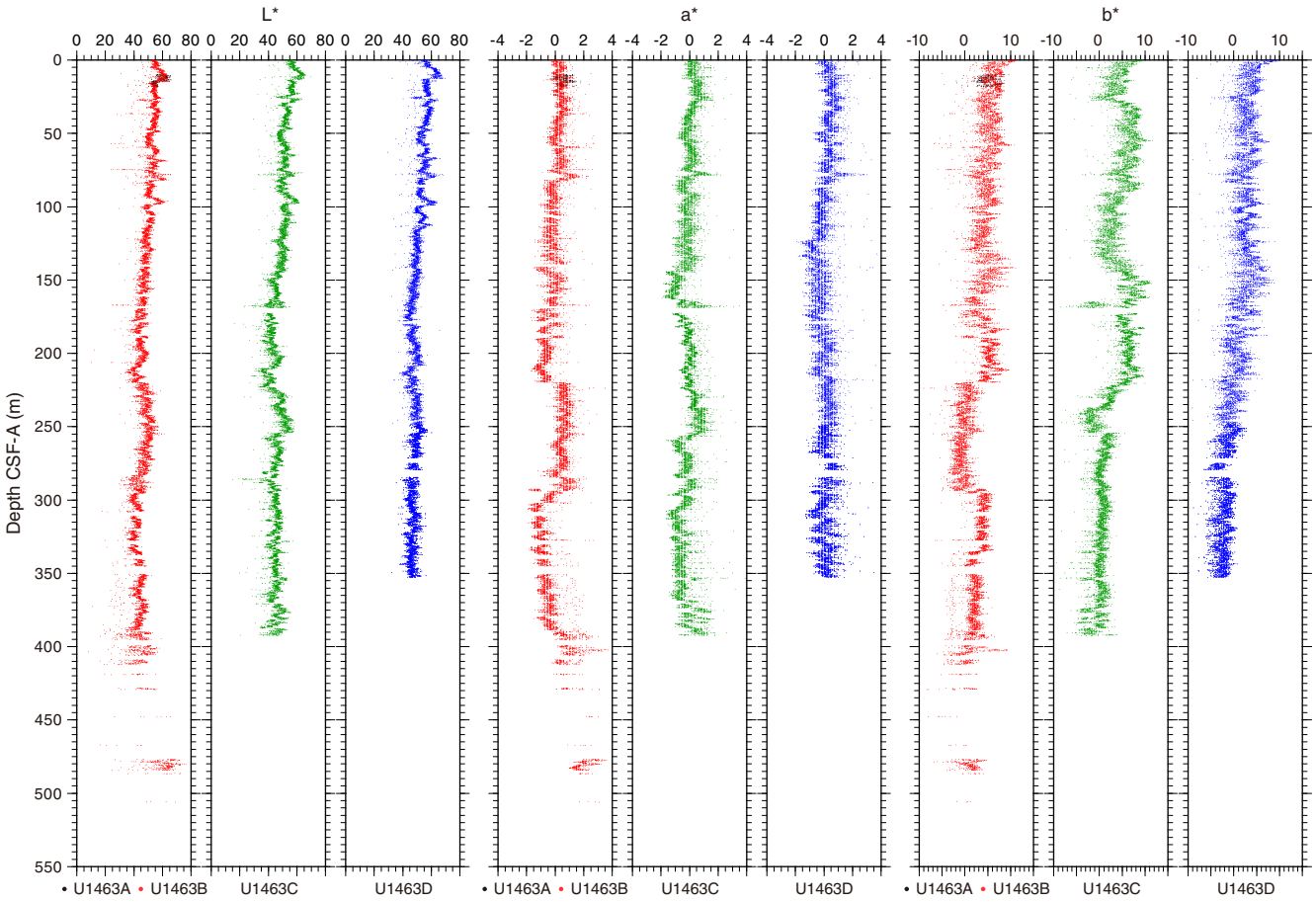

Figure F32. A. In situ temperatures measured with APCT-3, Hole U1463C. B. Thermal conductivity (*k*) measured on Hole U1463B (red) and U1463C (blue) cores and used in heat flow calculation. C. Thermal resistance (Ω) vs. temperature (*T*) (Bullard plot). D. Thermal conductivities as measured throughout entire cored interval. In B and D, only data with standard deviations <0.1 W/(m·K) are shown. Symbol width indicates standard deviation of each measurement.

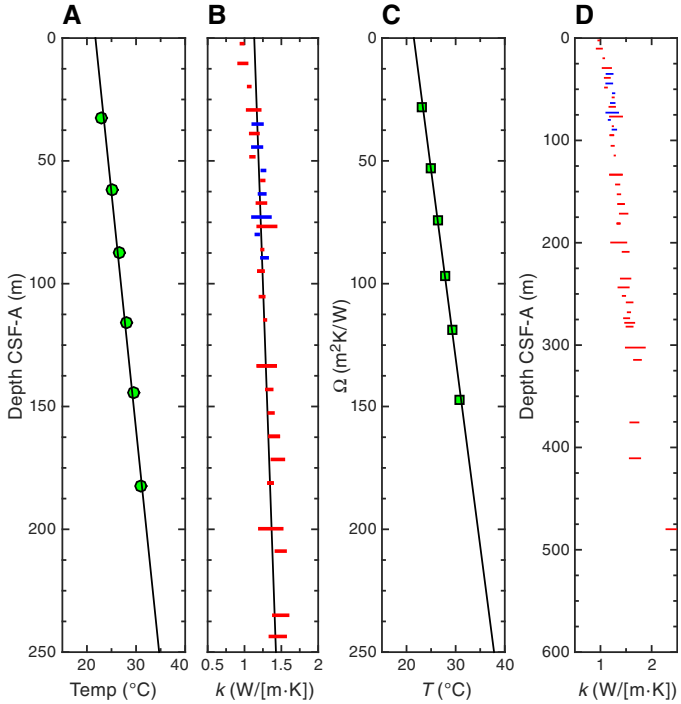

Downhole measurements

Downhole measurements were conducted in Hole U1463B. The triple combo tool string was run first between 452 m wireline log matched depth below seafloor (WMSF) and the seafloor. The triple combo measured borehole width, HSGR, bulk density, porosity, resistivity, and MS. We attempted a run with the VSI, but because marine mammals were commonly seen within the exclusion zone, operations with the VSI were terminated with measurements carried out at only a single station. We next ran a double pass with the FMS-sonic tool string (444–122 m WMSF). The HSGR log was in good agreement with core NGR data and allowed for correlation of wireline and core data. MS measurements were affected by temperature and were judged to be of insufficient quality for interpretation. Wireline bulk density and porosity measurements corresponded to the results of discrete sampling in cores in most of the logged interval. *P*-wave sonic velocities measured with the FMS-sonic tool string are consistently higher than sonic velocities measured on cored material. However, the same 20–30 m scale variability in sonic velocity is observed in both wireline logs and core-based measurements. Although the borehole diameter was relatively large, the FMS made full contact with the borehole wall and the FMS resistivity images are generally of good quality. Six APCT-3 in situ temperature measurements were made in Hole U1463C.

Depth matching

The logs were processed on shore before the processed logs were sent back to the ship during Expedition 356. The depth scales of the preprocessed logs were first shifted to make them relative to the seafloor (–158 m), which was determined by the step in gamma ray values observed on the triple combo main run. This differed by 1.7 m from the calculated seafloor depth of 156 m below rig floor determined by the drillers. The depth-shifted logs were then depth matched to the HSGR log from the main pass of the triple combo. Based on the correlation of distinct features between the wireline HSGR record and NGR measured on cores (see below), we consider that there is a 1–4 m discrepancy between core depths (CSF-A) and wireline logging depths (WMSF). In the discussion below, we refer to all logs in WMSF and all cores in CSF-A, realizing that the match between the two is only approximate within several meters.

Natural gamma radiation

HSGR was measured during both the down and up passes with the triple combo in Hole U1463B. Wireline HSGR data measured during the up pass showed good agreement with the composite NGR data obtained on whole-round cores from this site (Figure **F33**). In the upper part of the section, HSGR increased in a stepwise manner downhole, with steps at ~78 and ~110 m WMSF, the first of which corresponded to the end of the drill pipe. Between 110 and 200 m WMSF, HSGR showed strong meter-scale variability and ranged between 30 and 80 American Petroleum Institute gamma radiation units (gAPI). The five-window spectroscopy of the HSGR tool allowed the approximate concentrations of uranium (U), thorium (Th), and potassium (K) to be determined. These data showed that the peaks in HSGR in this interval were mainly driven by variations in U content. At 208 m WMSF, we observed a prominent peak in HSGR. This peak was also observed in core-based NGR, where it occurred at 210 m CSF-A. Between 210 and 385 m WMSF, HSGR remained relatively high and ranged between 30 and 60 gAPI. The amplitudes of the highest frequency variations in this interval were smaller than in the interval above. This interval was also characterized by low U concentrations, whereas the Th and K concentrations were relatively high. At 385 m WMSF, HSGR fell to about 20 gAPI and remained at that low level to the bottom of the hole at 433 m WMSF. This drop in HSGR corresponded to reductions in Th and K concentrations.

As mentioned above, some features in the wireline HSGR records from Holes U1463B were also observed in core-based NGR from this site. Six of the most robust core-log correlations are indicated by horizontal gray lines on Figure **F33** and consist of characteristic gamma ray peaks and troughs. The correlation of these distinct features indicates that the wireline depth is consistently shallower than the cored depth. The offset between wireline and coring depth varied between 1 and 4 m.

Magnetic susceptibility

MS was measured during downhole wireline logging with the triple combo in Hole U1463B. Similar to what was observed during downhole logging at Sites U1461 and U1462, the wireline MS measurements were affected by temperature (see **Downhole measurements** in the Site U1461 chapter and **Downhole measurements** in the Site U1462 chapter [Gallagher et al., 2017b, 2017c]). This resulted in wireline MS measurements that were not comparable to MS data measured on cores. This effect was not corrected for during processing. Therefore, the wireline MS data were judged to be of insufficient quality for interpretation.

Porosity, density, and resistivity

We measured porosity and density with the triple combo (Figure **F34**). Bulk density was measured with the Hostile Environment Litho-Density Sonde (HLDS) between 78.0 and 433.0 m WMSF, and porosity was measured with the Accelerator Porosity Sonde (APS) between 79.0 and 424.4 m WMSF. The results were judged to be of very good quality, based on the systematic variation in the logs, standoff distance of the APS (the distance between the tool and wall inferred from the APS signal), and consistency with the discrete MAD measurements on cores from Holes U1463A–U1463C. In our analysis of the wireline porosity and bulk density logs, we smoothed these properties over ~15 m, whereas the APS standoff was smoothed over ~30 m. The inferred bulk density is ~1.5 g/cm^3 at 78 m WMSF, just below the drill pipe, and increases markedly to about 2 g/cm^3 at 125 m WMSF. From 125 m WMSF, the wireline-inferred bulk density systematically increases to 2.25 g/cm^3 at the base of the logged interval (433 m WMSF).

Porosity measured by the APS, and corrected assuming that the material is limestone, starts at ~60% at 79 m WMSF. Porosity drops quickly to ~40% at 90 m WMSF and stays at this value for ~20 m before increasing to ~50% at 110 m WMSF. From 110 m WMSF to the base of the interval logged with the APS, porosity decreases to ~35% with small-amplitude fluctuations of ~5% in the interval between 290 m WMSF and the base of the logged interval. The wireline tracking of both the systematic increase in bulk density and the systematic decrease in porosity from 110 to 450 m WMSF agrees with the values measured on cores. We attribute the low bulk density and fluctuating porosity in the interval between 78 and 110 m WMSF to the wide borehole, whose diameter was >17.5 inches in this interval, although the standoff distance of the APS is inferred to be <1 inch (Figure **F34**).

Formation MicroScanner

The FMS-sonic made two passes in Hole U1463B. The FMS images reveal differences in textures and lithology through a logged in-

Figure F33. Hole U1463B diameter (caliper) and HSGR measured by triple combo, NGR from Hole U1463B–U1463D whole-round cores, and elemental uranium, thorium, and potassium concentrations estimated from Hole U1463B HSGR spectra.

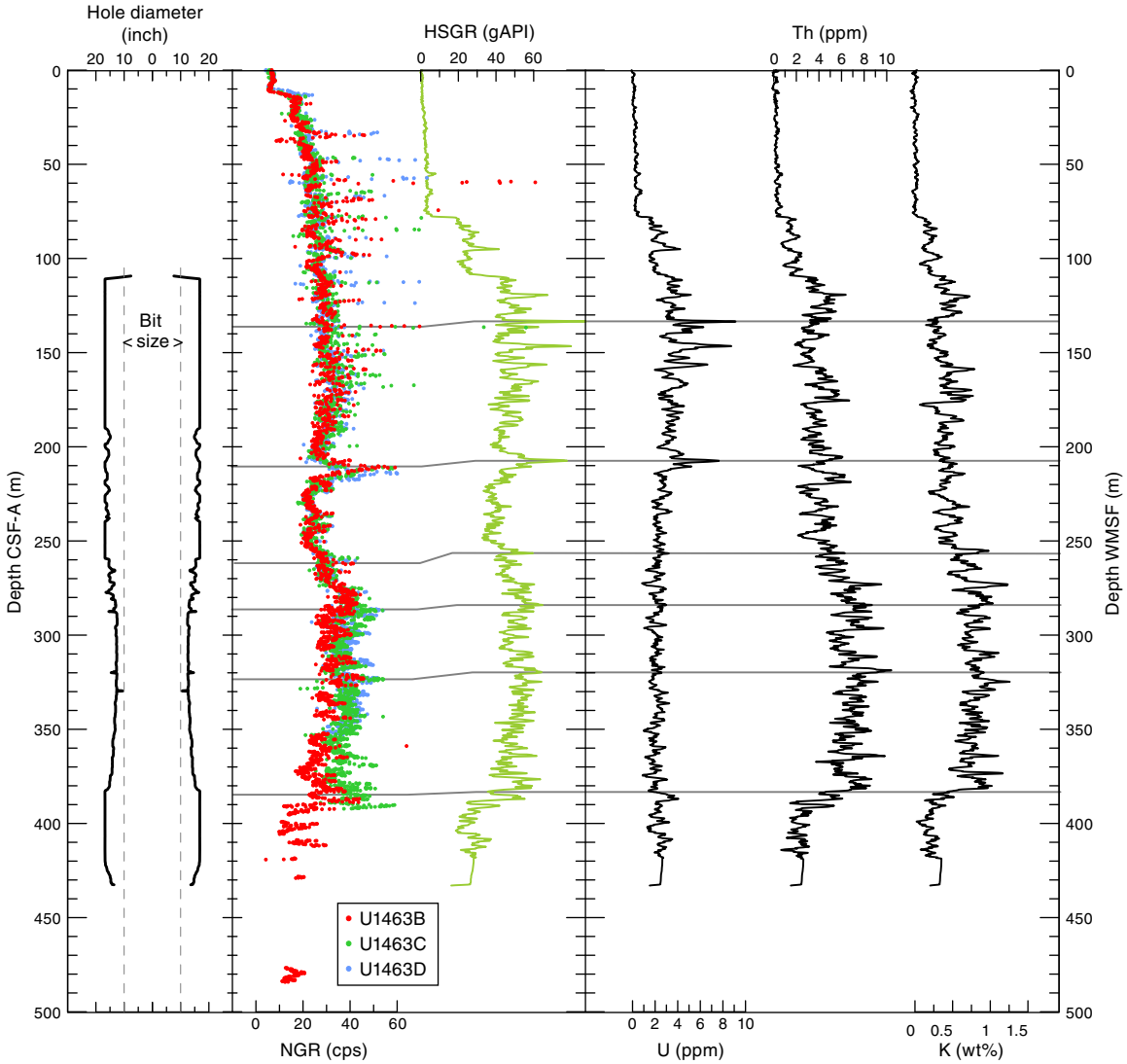

terval extending from ~122 to 444 m WMSF. Both passes yielded FMS images of generally good quality except for the upper section of the hole (shallower than 280 m WMSF) where the FMS pads appeared not to be making full contact with the borehole wall and thus complete coverage of the borehole was lacking. Within much of the borehole, the images generated from the two passes are very similar. This gives us confidence in the results, while also suggesting that the pads from the two passes followed nearly the same pathway upward, presumably due to the shape of the borehole or grooves that developed in the first upward pass. The consistency in results is illustrated for the interval from 359 to 366 m WMSF (Figure **F35**). From about 443 m WMSF upward, the FMS showed 20–50 cm wide horizontal resistive bands with diffuse edges that were separated by about 5 m. Upward from ~406 m WMSF, there were occasional distinct bands of high conductivity with thicknesses <5 cm. Starting at ~380 m WMSF, these thin conductive bands became more prevalent and some have the appearance of being tilted from the horizontal less than 20°. This pattern continues upward but changes in borehole diameter became more obvious at ~280 m WMSF where regions of pervasive high conductivity appeared, probably due to loss of contact with the borehole walls.

Seismic properties

We measured the seismic properties of Site U1463 using both the FMS-sonic tool string and a vertical seismic profile using the VSI. The sonic *P*-wave velocity was determined in two passes with the FMS-sonic tool. Unfortunately, we were only able to determine the traveltime to one station during the VSI deployment because of the appearance of marine mammals and subsequent termination of seismic operations.

Wireline sonic velocities show a steady increase from ~1800 m/s at 80 m WMSF to ~2300 m/s at ~250 m WMSF. Superimposed on this gradual increase, meter-scale variations with an amplitude of ~250 m/s are observed (Figure **F36**). Between 250 and 280 m WMSF, wireline sonic velocities decrease to 2150 m/s, after which they start increasing again to 2450 m/s at 375 m WMSF. From that depth to the bottom of the logged interval (426 m WMSF), sonic velocities increase with depth at a higher rate, reaching a maximum

Figure F34. Hole U1463B diameter (caliper; black) and smoothed standoff distance (×10; blue) inferred from APS on triple combo with bulk density and porosity (lines = smoothed Hole U1463B wireline HLDS/APS, circles = Hole U1463A–U1463C discrete MAD measurements).

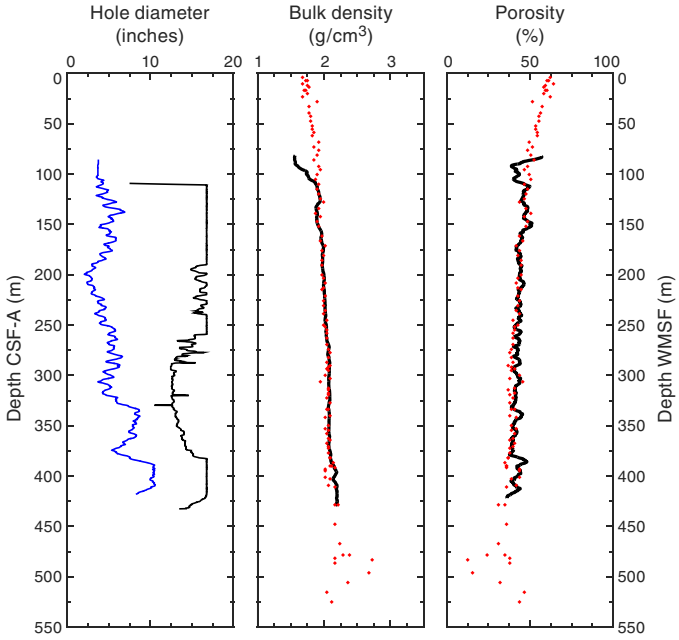

of 2950 m/s at 425 m WMSF. The wireline logging sonic velocities were considerably higher than discrete measurements with the *P*-wave caliper (see **Physical properties**). Sonic velocities measured on cores recovered with the XCB system from Hole U1463B (300–470 m CSF-A) showed a smaller discrepancy with wireline sonic velocities than measurements on HLAPC/APC cores from Hole U1463C in the same depth interval.

In situ temperature

In situ temperature measurements were made in Hole U1463C using the APCT-3 in Cores 4H, 7H, 10H, 13H, 16H, and 20H. The temperature logs are described and interpreted in **Physical properties**.

Figure F35. FMS images processed with dynamic method, Hole U1463B Passes 1 and 2.

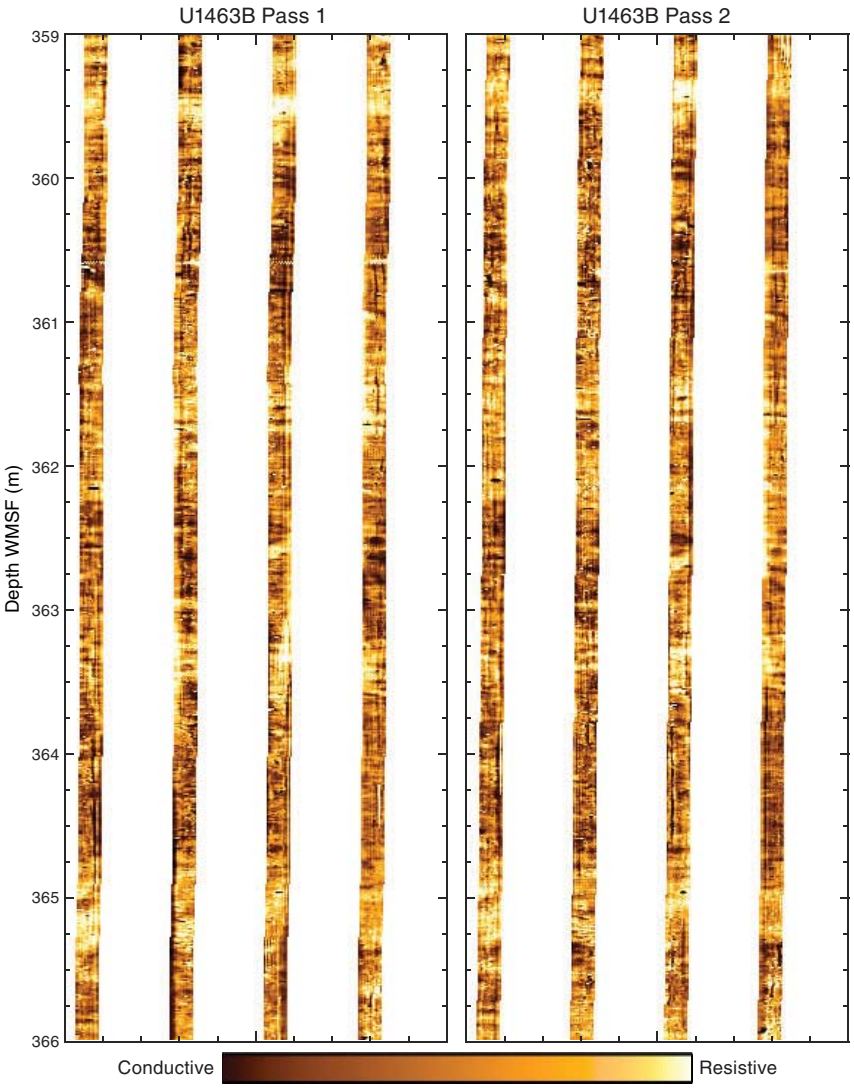

Figure F36. Hole U1463B diameter (caliper) measured by FMS-sonic caliper and sonic velocities from Hole U1463B wireline and Hole U1463B–U1463D discrete core measurements.

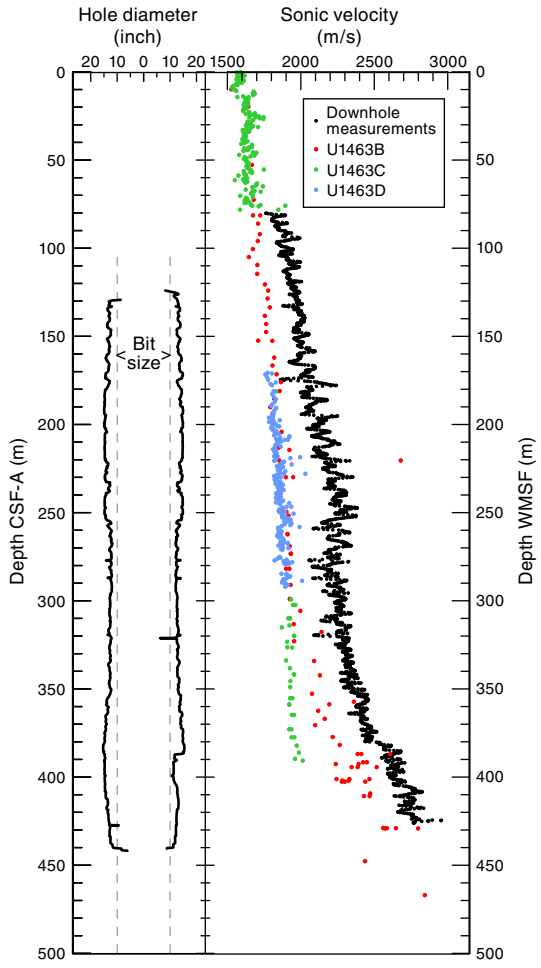

Stratigraphic correlation

Site U1463 was triple cored from the seafloor to 352 m CSF-A using the APC, HLAPC, and XCB systems in order to recover a complete and continuous section (Figure **F37**). The stratigraphic correlators provided guidance to the drillers to ensure drilling gaps between holes did not overlap and to determine the mudline depths for the second and third APC holes. A correlation was generated for the upper ~350 m between Holes U1463B, U1463C, and U1463D (Figure **F38**), and a splice was produced to 276.11 m CSF-A (Tables **T16**, **T17**, **T18**; Figure **F39**). Hole U1463B extends beyond the correlated depth to 530 m CSF-A (Core 356-U1463B-60X). High recovery in the upper ~350 m is attributed to the absence of hardgrounds, unlike at other Expedition 356 sites, and the presence of sediments suitable for deeper piston coring. Variability in lithology and coring methods between holes causes some uncertainty in the correlation of the physical properties values. The physical properties values change downhole to the extent that a switch from a MS-based correlation to a NGR-based correlation became necessary. Hole and site summaries indicate generally high sedimentation rates, well above typical pelagic rates (Figures **F40**, **F41**, **F42**). Sedimentation rates are moderate through the Pliocene and increase (11–19 cm/ky) in the Pleistocene (Zone NN18/NN19 boundary to PT1a/Pt1b boundary). Rates decline again to moderate levels (5 cm/ky) at the Pt1a/Pt1b boundary.

Guidance for coring (using CSF-A)

Cores were measured for MS and GRA on the Special Task Multisensor Logger immediately after recovery at 10 cm intervals. The results were used to monitor for coring gaps in real time, and adjustments were made in Holes U1463C (e.g., Core 9H) and U1463D (e.g., Core 12H) to avoid producing recovery gaps at the same depths in all three holes. NGR data were used to determine the optimal penetration for the mudline cores of Holes U1463C and U1463D.

The tidal range at Site U1463 can reach 2.7 m (data provided by the Australian Bureau of Meteorology, Canberra, using 2012 Global Tidal Model). Therefore, if piston coring is started at different points in the tidal cycle, the depth to seafloor measurements will differ between holes and the mudline shot will not hit the desired depth target, complicating correlation (see more detailed discussion in **Stratigraphic correlation** in the Expedition 356 methods chapter [Gallagher et al., 2017a]). Tidal heights at the approximate times of mudline shots for Holes U1463B–U1463D were monitored to avoid a coring gap around the first core. Because tides change the water depth, the length of the drill string must be adjusted to ensure the mudline core is shot to reach the correct target depth. Therefore, the start depth for APC coring in Holes U1463C and U1463D was adjusted relative to the tidal height at the time coring began in Hole U1463B (see Figure **F37** for position of the start of coring for each hole relative to the tidal cycle).

In addition to making adjustments for coring guidance as a result of variable tidal heights, further operational guidance targeted intervals of low to no recovery or intervals with high core disturbance (Figure **F37**). Coring using the XCB system in Hole U1463B (deeper than ~285 m CSF-A) resulted in good recovery but intense drilling disturbance, particularly heavily biscuited cores and one core with zero recovery (Core 356-U1463B-41X). The low recovery and high disturbance is attributed to slow drilling rates (e.g., Core 356-U1463A-44X advanced just 4 m in 50 min of drilling time) through a dense, clay-rich interval. Holes U1463C and U1463D had much higher recovery through the same interval (~280–350 m CSF-A) as a result of using the HLAPC system instead of XCB coring and advancing by recovery. Although recovery rates improved and drilling disturbance was reduced, several very short cores resulted from this approach. The shortest core (356-U1463C-39F) has a length of 0.69 m. Additionally, differences in physical properties were discovered that appear to be linked to the type of coring system used (APC/HLAPC or XCB; see **Physical properties**).

Correlation of the cores (to produce CCSF-A)

All three holes had good recovery, so a correlation could be made to ~350 m core composite depth below seafloor (CCSF-A) (Figure **F38**). The offsets (Table **T16**) are generated in CSF-A and applied to the cores (Table **T17**) to produce a CCSF-A depth scale. Squeezed core liners were not included in the correlation and are responsible for most of the disturbance noted in full piston cores in Figure **F37** (e.g., Cores 356-U1463B-9H and 356-U1463C-5H).

The correlation between the three holes is high in the upper 276.11 m CSF-A (Figure **F38**). It is anchored on the mudline established in Hole U1463B and results in a CCSF-A scale (Tables **T16**, **T17**). The correlation from ~306 to ~395 m CSF-A (Core 356-U1463C-54F) is more tentative with a higher degree of uncertainty (Figure **F38G**, **F38H**). The CCSF-A depth scale provides a common

Figure F37. Timing of coring and quality of core recovery linked to position in the tidal cycle. Colors in the core recovery columns for Holes U1463B–U1463D identify zones of high (red) and moderate disturbance (orange). The level of disturbance is derived from visual core descriptions (see **Core descriptions**) and lithologic descriptions (see **Lithostratigraphy**). Operations timing is shown by H (start APC), F (start HLAPC), X (start XCB), and EOH (end of hole) relative to tides calculated for latitude 18°57.918′S, longitude 117°37.4220′E. Blue = portions of tidal cycle with no coring activity.

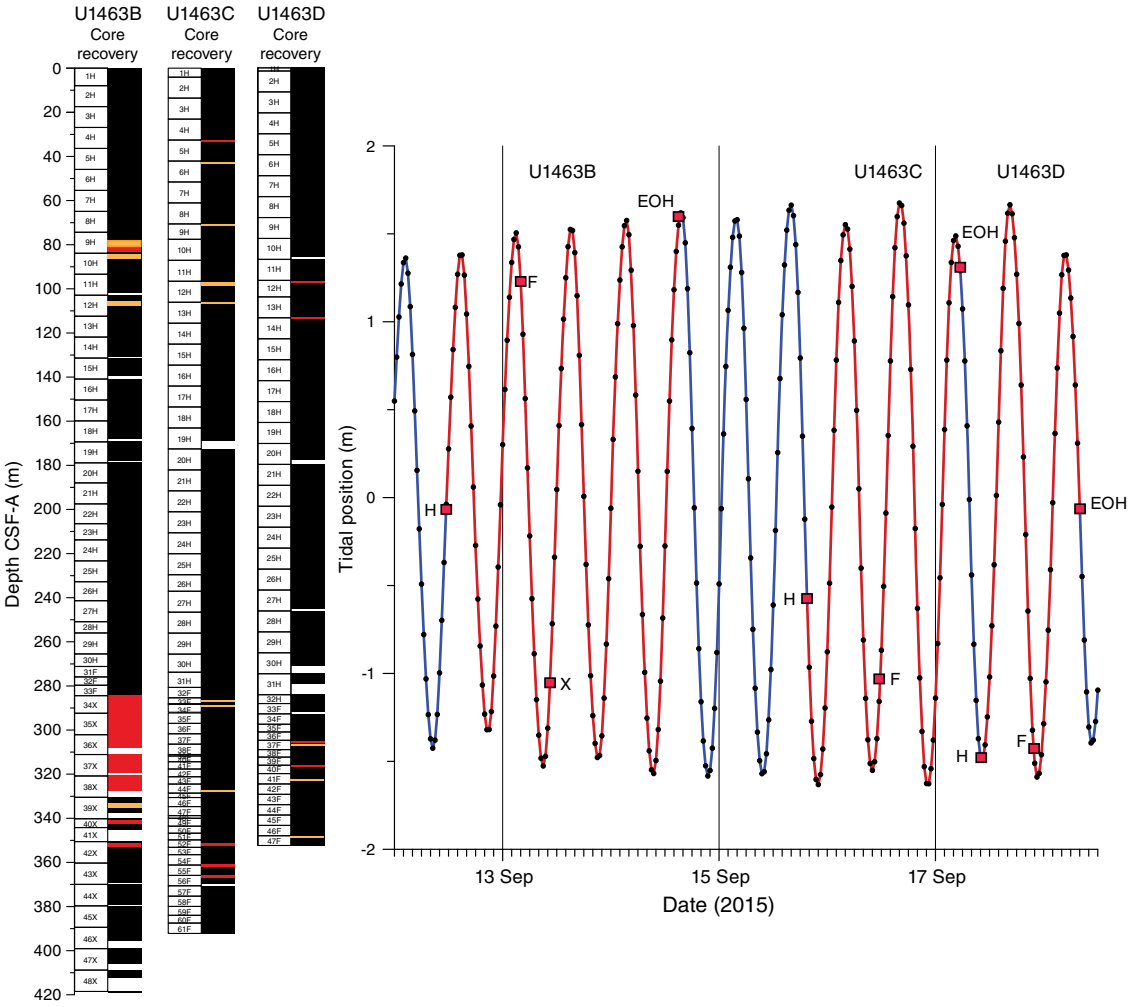

point of reference for all three holes and depths are typically deeper than the CSF-A scale (see **Stratigraphic correlation** in the Expedition 356 methods chapter [Gallagher et al., 2017a] for a detailed explanation). Offsets produce a growth rate of 9% (i.e., the total depth of the CCSF-A scale is ~9% greater than the CSF-A scale). As a result, the depth of the correlated portion of Hole U1463B grows from 340.2 m CSF-A to 371.4 m CCSF-A, the depth of Hole U1463C grows from 387.5 m CSF-A to 421.6 m CCSF-A, and the depth of Hole U1463D grows from 348.4 m CSF-A to 379.4 m CCSF-A (Table **T16**). Although top offsets from CSF-A (affine value, see Table **T17**) generally increase downhole, a few intervals exhibit decreases. For example, the offset from CSF-A in Core 356-U1463C-20H decreases by 3.3 m compared to the overlying Core 356-U1463C-19H (Table **T16**). Because Site U1463 was drilled during spring tides and tidal differences were as large as 2.5 m (Figure **F37**), some of these shifts in offset are likely due to tidal differences, although the changes are within the range of typical ship heave.

Even though offsets were applied to each core, the correlation was determined by the features that were most similar between holes (Figure **F38**; Table **T17**). Not all peaks can be matched to the CCSF-A depth (e.g., ~262–267 m CCSF-A [Figure **F38F**]), and cores are not stretched or compressed to match for the correlation or splice. The affine table used to create CCSF-A depths is presented in Table **T17**.

The correlation (Figure **F38**) is not unequivocal because of differences in the coring system used (e.g., APC, HLAPC, and XCB) and lithologic variability between holes. For example, the HLAPC system allowed recovery of excellent quality sediments to great depth (392.49 m CSF-A in Hole U1463C), but the shorter length of the core barrel (4.7 m maximum) limits the certainty of correlation between cores deeper than ~280 m CSF-A. This effect is particularly enhanced in Hole U1463B, where several cores were partial strokes resulting in even shorter cores, most frequently 2–4 m long but some even shorter. A guiding principle of stratigraphic correlation is to avoid using correlation tie points at the ends of cores, where the risk of disturbance or contamination is highest. However, short cores limit choices for tie points, particularly in regions where the signal being correlated is not consistent between holes. For example, some intervals have distinct peaks in either NGR or MS in one hole but not in all three holes (e.g., Hole U1463D has no NGR peak despite the strong peaks in Holes U1463B and U1463C at ~147 m CCSF-A [Figure **F38C**]). Furthermore, the intensity of the MS

Figure F38. Correlation of the upper ~350 m between Holes U1463B, U1463C, and U1463D. The correlation is defined in Table **T17** and graphically identifies features used to correlate between holes. Cores are mapped to the CCSF-A depth scale. Solid lines = tie points used in the correlation to align cores, short dashed lines = points that support the correlation but were not used to align cores, long dashed lines = uncertain correlations, arrows = splice tie points. Circles suggest intervals of core expansion. A. 0–50 m CCSF-A. B. 50–100 m CCSF-A. (Continued on next three pages.)

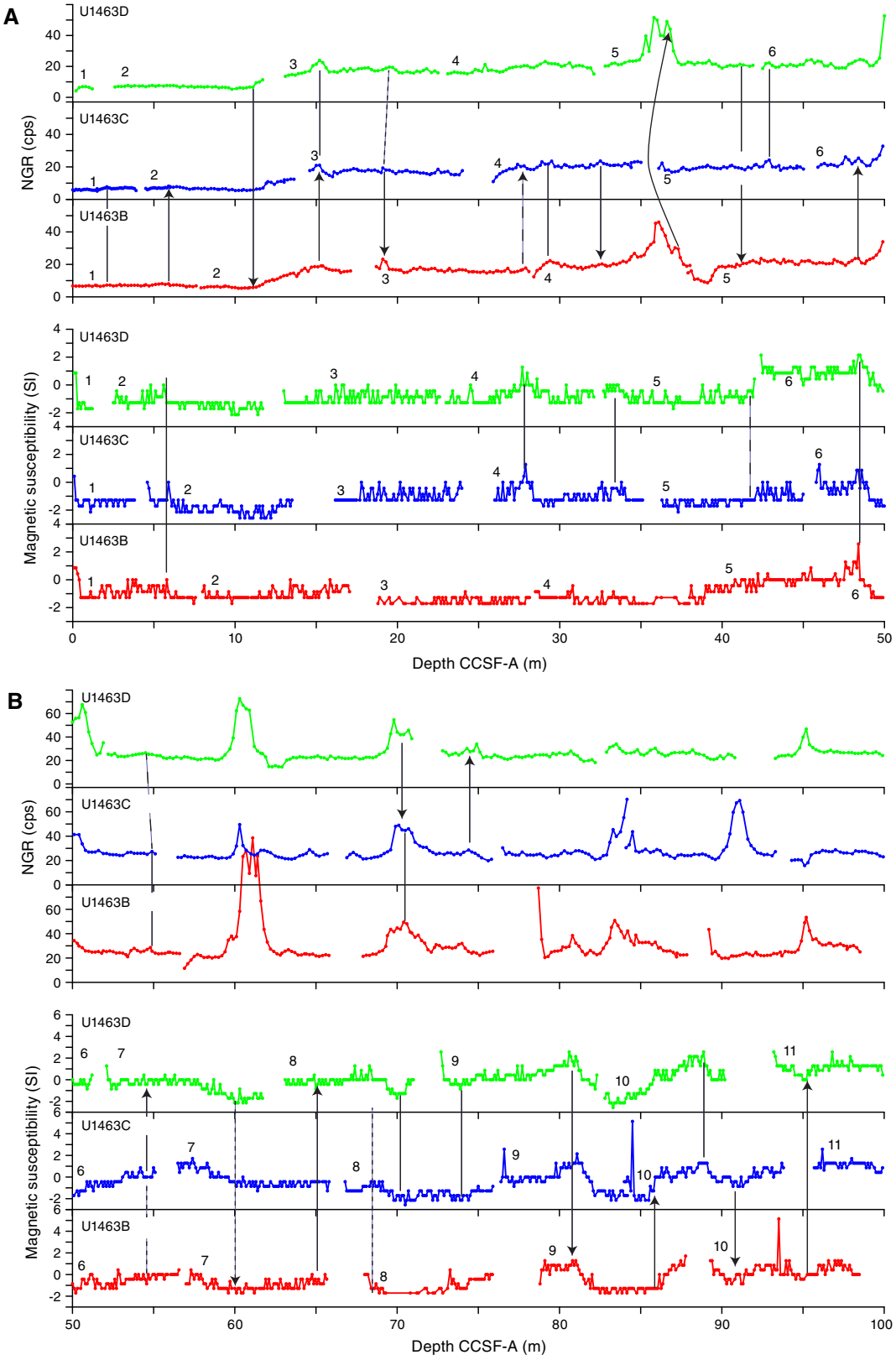

Figure F38 (continued). C. 100–150 m CCSF-A. D. 150–200 m CCSF-A. (Continued on next page.)

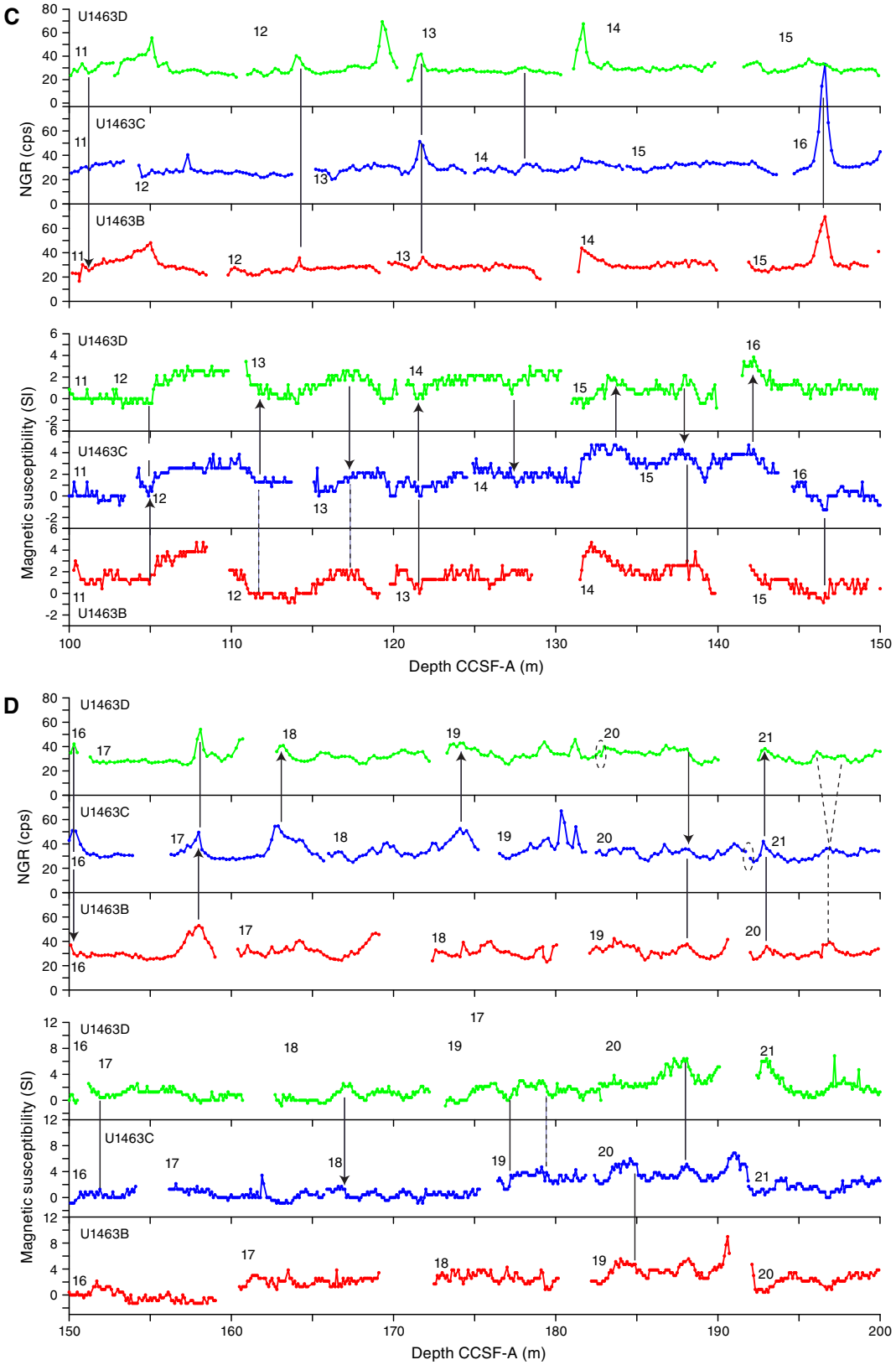

Figure F38 (continued). E. 200–250 m CCSF-A. F. 250–300 m CCSF-A. (Continued on next page.)

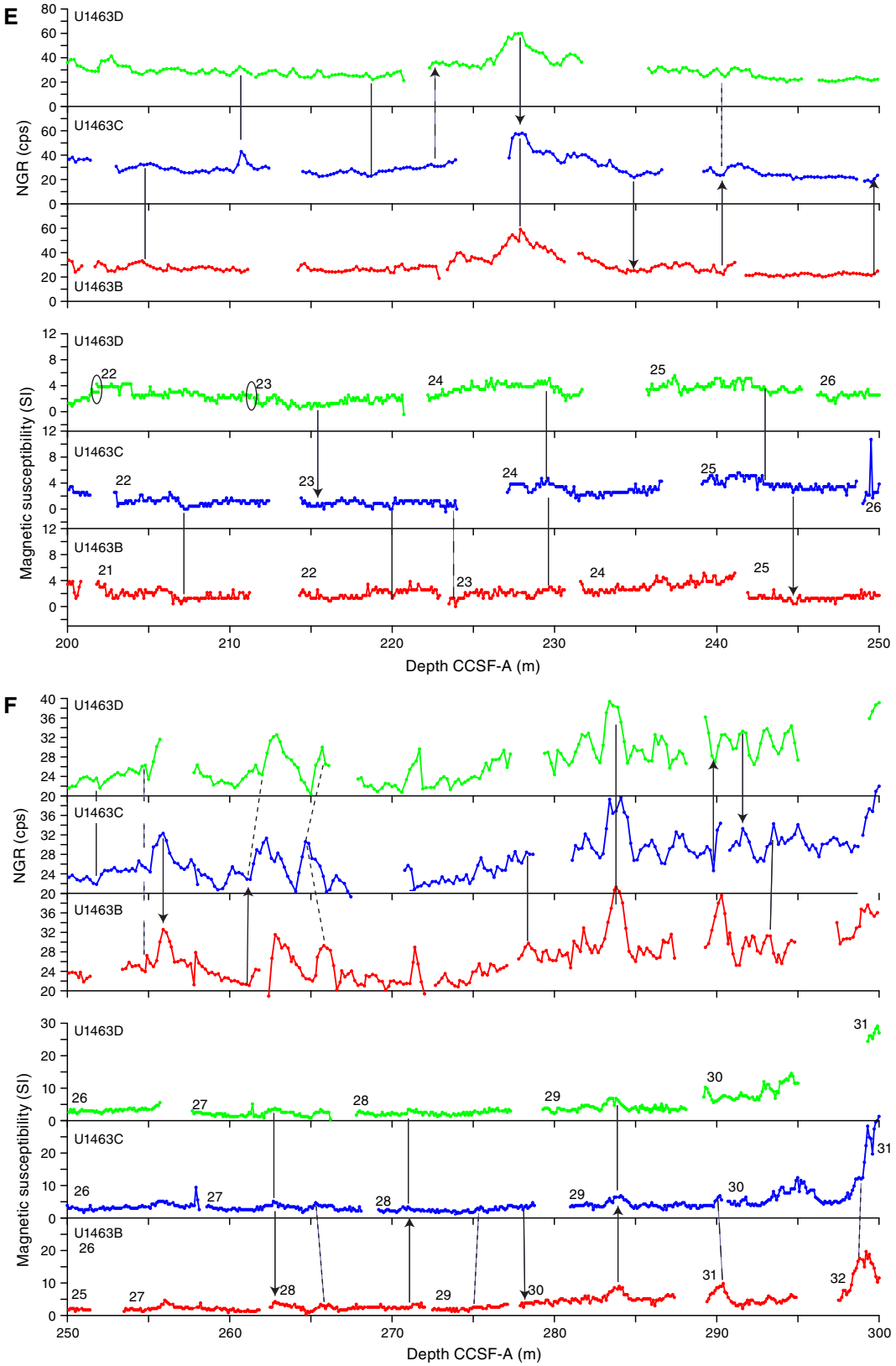

Figure F38 (continued). G. 300–350 m CCSF-A. Gray shading = zone of low certainty in correlation. H. 350–400 m CCSF-A.

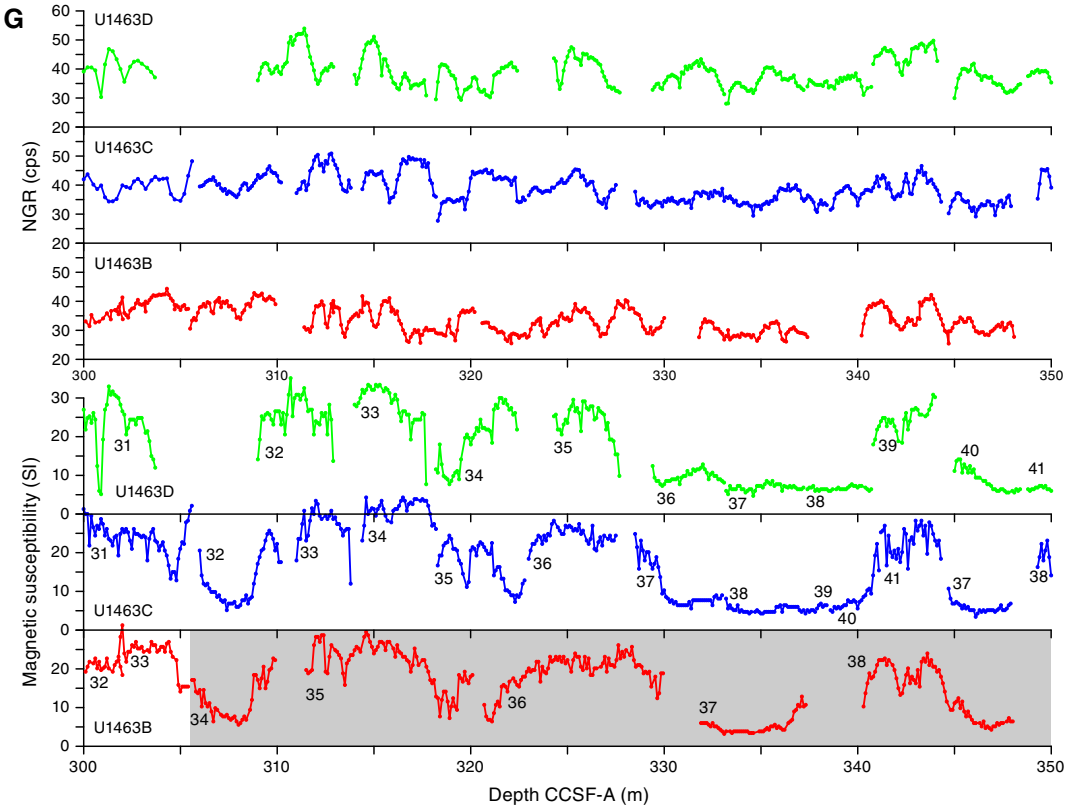

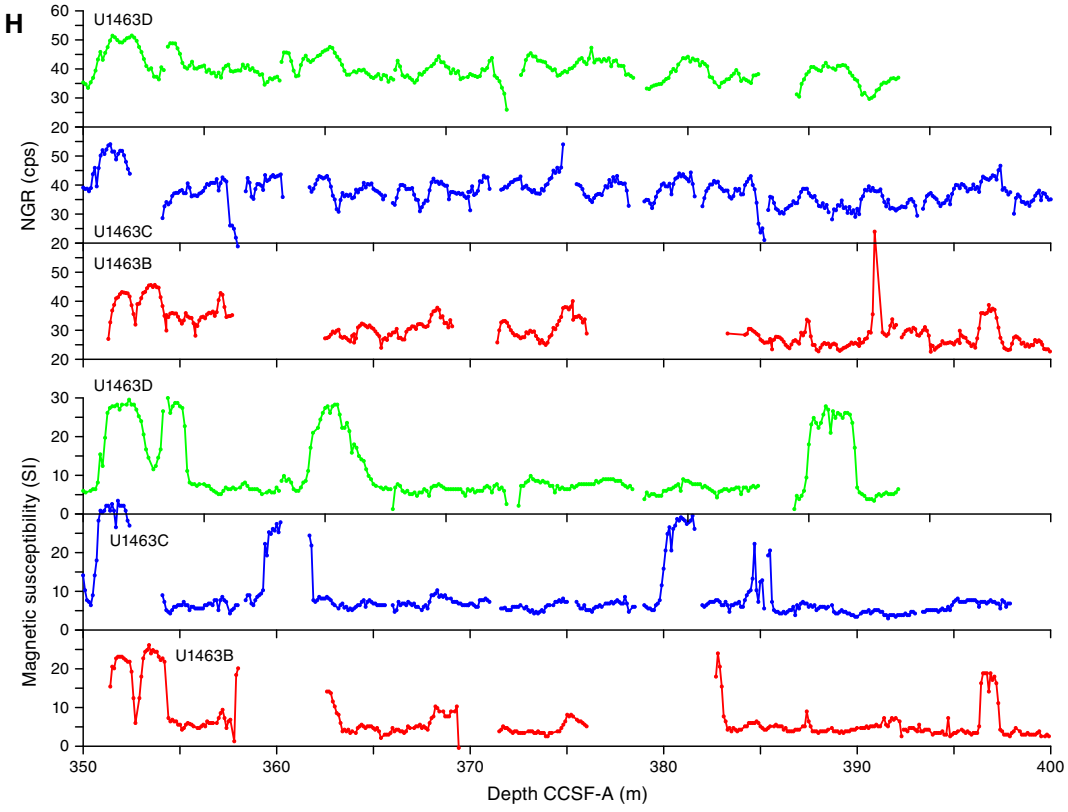

Figure F39. Spliced NGR record compared to NGR records from the individual holes, Site U1463. Tie points for the splice are shown in Figure **F38**. A. 0–100 m CCSF-A. B. 100–200 m CCSF-A. (Continued on next page.)

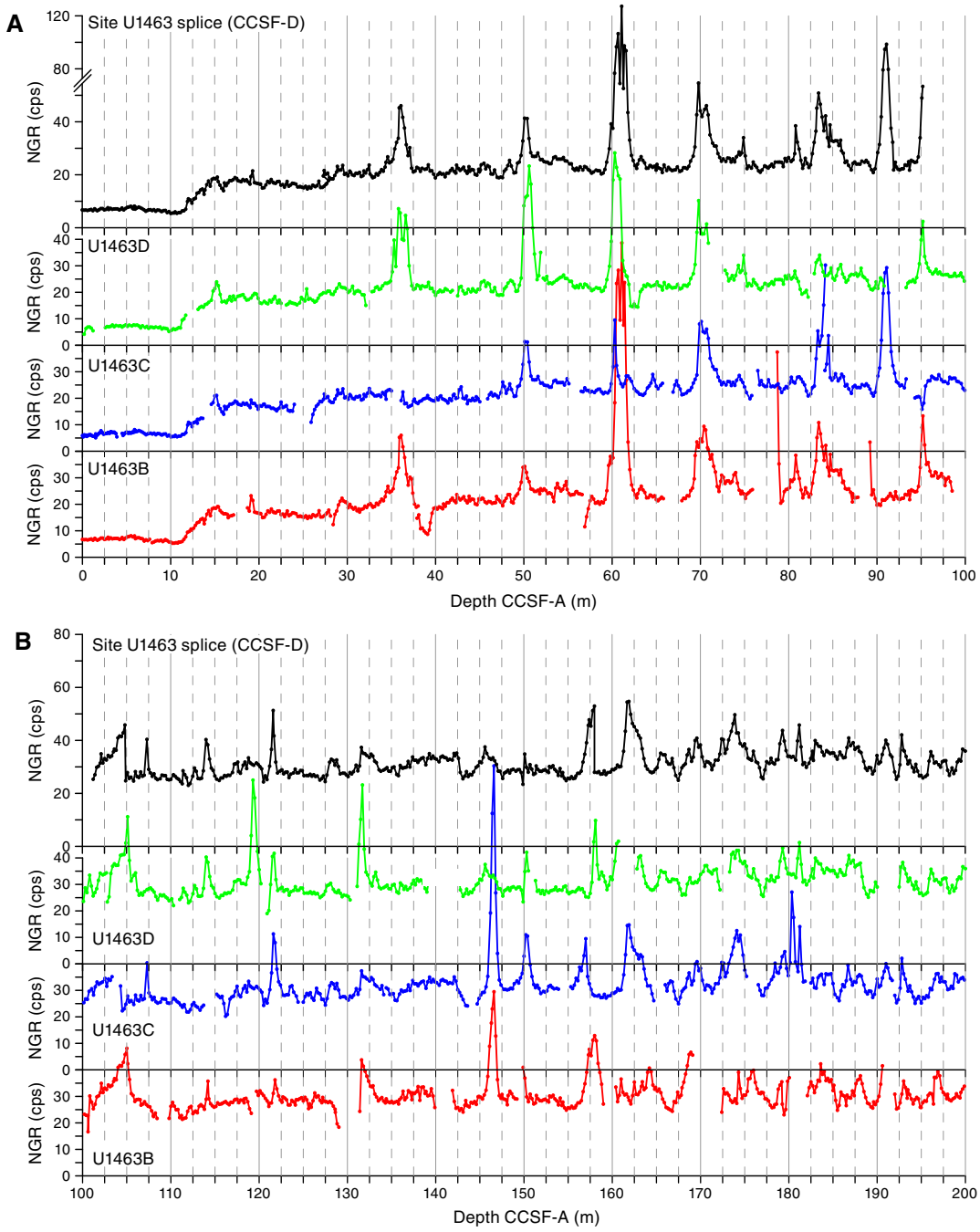

and NGR signals also changes downhole, from small- to large-amplitude variation (NGR exhibits strong peaks deeper than ~250 m CCSF-A and MS has very large values deeper than ~300 m CCSF-A) (see Figure **F38**). Much of the variability between and down holes is attributed to pyritization and other diagenetic alteration (see **Lithostratigraphy**) and to differences resulting from piston cores versus biscuited XCB cores.

Construction of a splice (to produce CCSF-D)

A splice based on the cores shown in Figure **F38** was created for the upper 276.11 m CSF-A in Hole U1463B, 273.5 m CSF-A in Hole U1463C, and 268.1 m CSF-A in Hole U1463D (these depths are all equivalent to 298.5 m CCSF-A in the composite or correlation; Table **T18**; Figure **F39**).

Unequivocal tie points were not always available, but because a correlation had to be made, some uncertainties in the correlation between holes were introduced. Correlations are uncertain in the interval between ~162 and 185 m CCSF-A (Figure **F39B**); NGR is highly variable between holes and MS exhibits low overall downhole variability. This uncertainty may break the stratigraphic continuity established at the mudline with Core 356-U1463B-1H. There is also a level of subjectivity in the selection of the exact locations of tie points, even though the patterns of peaks may be similar. For example, because the NGR peak at ~37 m CSF-A is not present in

Figure F39 (continued). C. 200–300 m CCSF-A.

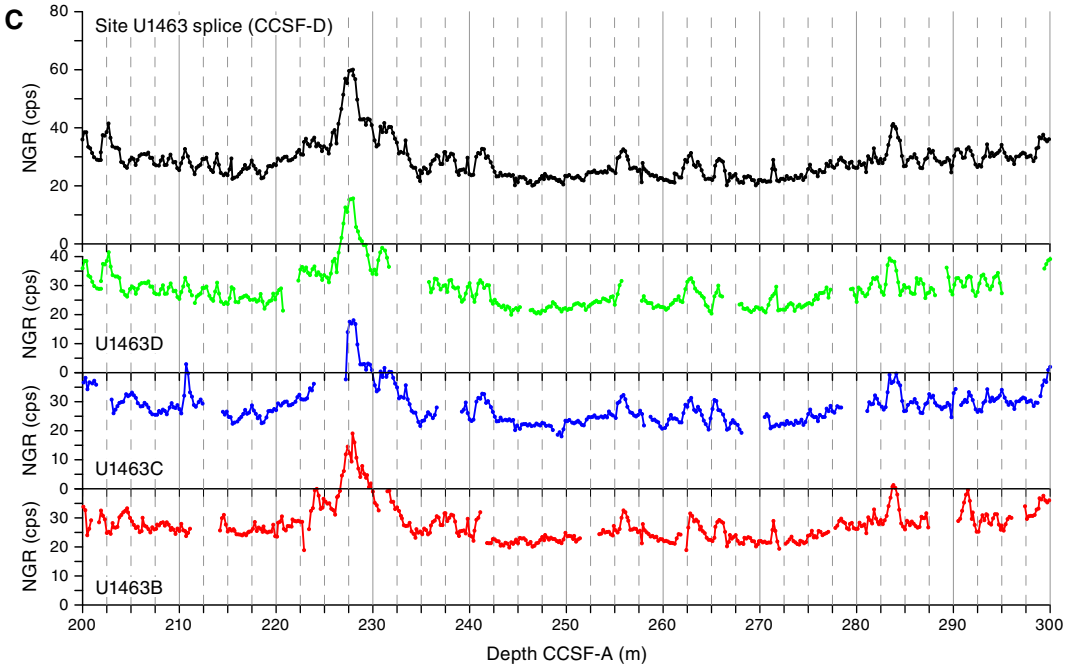

Hole U1463C and the shape of the peak differs between Holes U1463B and U1463D, the splice between Cores 356-U1463B-4H and 356-U1463D-5H assumes a correlation between the last (deepest) peaks in both Cores 356-U1463B-4H and 356-U1463D-5H (Figures **F38A**, **F39A**).

Note that the CCSF-D scale rigorously applies only to the spliced interval. Intervals outside the splice, although available with CCSF-A depth assignments, should not be expected to correlate precisely with fine-scale details within the splice or in other holes because of variation in the relative spacing of features in different holes. Such apparent depth differences of specific features may also reflect coring artifacts or fine-scale spatial variations in sediment accumulation and preservation at and below the seafloor.

Correlation of core to wireline

Hole U1463B was logged and the wireline gamma log (HSGR) was compared to core-based NGR data (Figure **F40**). The patterns are similar: large peaks in NGR are equivalent to peaks in the wireline gamma log, such as peaks at ~98 and 212 m CSF-A. Smaller peaks and troughs are also equivalent, such as at ~306 m CSF-A. However, there are some peaks or sets of peaks that do not correlate, such as between ~175 and 200 m CSF-A, where differences exist in both the number and intensity of the peaks. This is not attributed to minor coring gaps, or to the offset, which is minimal at this depth (see **Physical properties** and **Downhole measurements**).

Hole and site summaries (sedimentation rates)

A summary of the relationship between NGR and color reflectance b* (see **Physical properties**), biostratigraphic, lithostratigraphic (see **Biostratigraphy and micropaleontology** and **Lithostratigraphy**), and magnetostratigraphic (see **Paleomagnetism**) data, plus sedimentation rates calculated from biostratigraphic datums (see **Biostratigraphy and micropaleontology**), is presented graphically for Holes U1463B–U1463D (Figures **F40**, **F41**, **F42**) and Site U1463 (Figure **F43**). Sedimentation rates were calculated assuming a linear sedimentation rate between datums (in centimeters per thousand years and using the CSF-A depth scale).

Sedimentation rates are moderate (5–6 cm/ky) in the Miocene to early Pliocene (through Zone PL2) and increase (8–9 cm/ky) through Zone PL3 (Figures **F40**, **F41**, **F43**). The expanded early Pliocene section is characterized by low NGR and high MS. Sedimentation rates slow (4–5 cm/ky) in the late Pliocene (Zone PL5 and early Zone PL6) but increase greatly into the Pleistocene (16–19 cm/ky). Sedimentation rates are reduced (7 cm/ky) at around ~1 Ma (base of *R. asanoi*) (Figure **F40**) but increase (11–13 cm/ky) through Zone Pt1a. Sedimentation rates decrease in Zone Pt1B (2–5 cm/ky). Differences in sedimentation rates between the holes are attributed to differences in sampling intervals (see **Biostratigraphy and micropaleontology** for details on sampling) and not the lithologic differences between holes identified in the correlation (Figure **F38**).

The summary figure for Site U1463 (Figure **F43**) includes NGR measured on core, MS, and total gamma radiation values from wireline logging in Hole U1463B. Biostratigraphic datums were selected for the site summary figure to show the general biostratigraphic pattern and were used to determine sedimentation rates for the site as a whole. The site summary figure does not provide the level of detail found in the hole summary figures and does not illustrate the differences found, for example, in datum levels or lithostratigraphy between the holes. Magnetostratigraphy indicates a change from the Gilbert Chron to Gauss Chron at 282 m CSF-A.

The general pattern is one of moderate sedimentation rates through the Pliocene and an increase (11–19 cm/ky) in the Pleistocene (Zone NN18/NN19 boundary to Zone PT1a/Pt1b boundary). Sedimentation rates reduce to moderate levels (5 cm/ky) at the Zone Pt1a/Pt1b boundary (Figure **F41**). Sedimentation rates in this hemipelagic system are always well above average rates in pelagic systems. There is no clear relationship between changes in sedimentation rate and lithology, although this may be related to the coarse shipboard biostratigraphic sampling interval.

Figure F40. Hole U1463B summary showing core recovery, graphic lithology, lithostratigraphic units, age, and biostratigraphic data plotted against MS, NGR, and wireline HSGR. Biostratigraphic zone boundary ages are shown. Age-depth model was produced from biostratigraphic datums only (see **Biostratigraphy and micropaleontology**) and assumes a linear sedimentation rate between datums (solid circles = calcareous nannofossils, open circles = planktonic foraminifers). See Figure **F7** in the Expedition 356 methods chapter (Gallagher et al., 2017a) for lithology key. BF = benthic foraminifer, PF = planktonic foraminifer, NN = calcareous nannofossil. IS = inner shelf, MS = middle shelf, OS = outer shelf, UB = upper bathyal. Gray bar = casing depth.

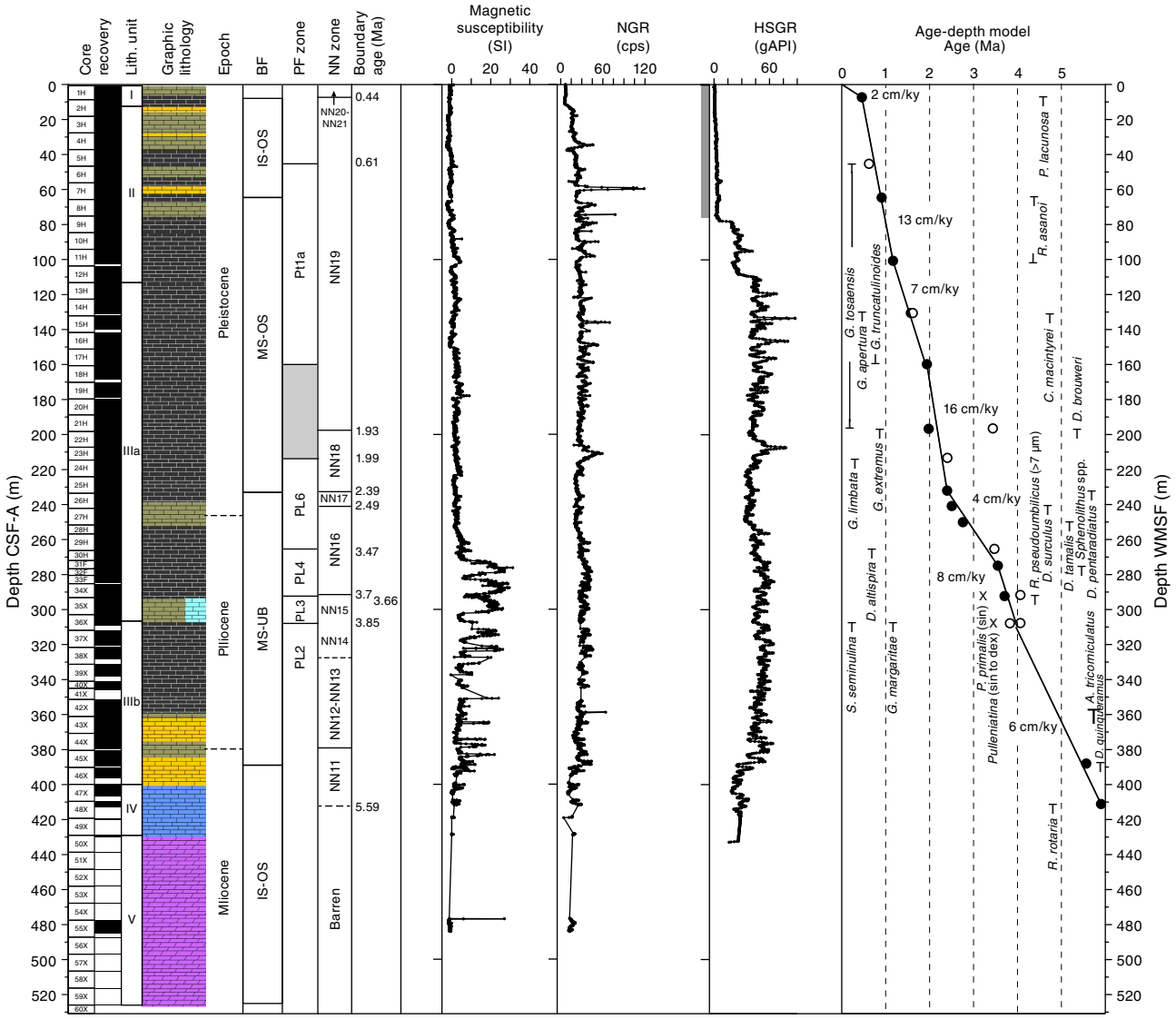

Figure F41. Hole U1463C summary showing core recovery, graphic lithology, lithostratigraphic units, age, and magnetostratigraphic and biostratigraphic data plotted against MS and NGR. Magnetostratigraphy and biostratigraphic zone boundary ages are shown. Age-depth model was produced from biostratigraphic datums only (see **Biostratigraphy and micropaleontology**) and assumes a linear sedimentation rate between datums (solid circles = calcareous nannofossils, open circles = planktonic foraminifers). See Figure **F7** in the Expedition 356 methods chapter (Gallagher et al., 2017a) for lithology key.

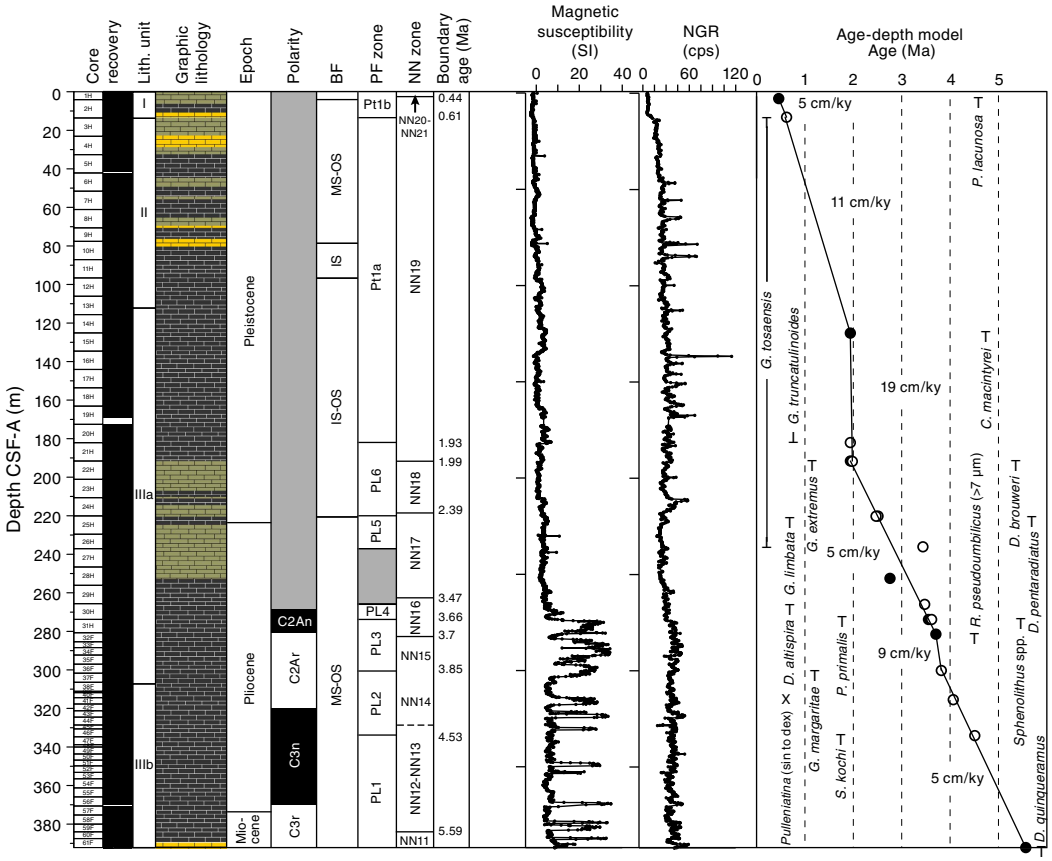

Figure F42. Hole U1463D summary showing core recovery, graphic lithology, and lithostratigraphic units, plotted against MS and NGR. No biostratigraphy or magnetostratigraphy was performed on this hole. See Figure **F7** in the Expedition 356 methods chapter (Gallagher et al., 2017a) for lithology key.

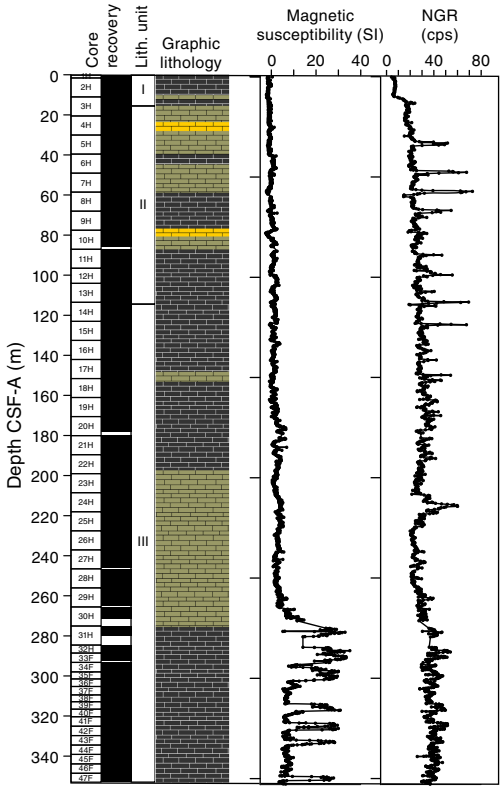

Table T16. Offset table, Holes U1463B–U1463D. **Download table in .csv format.**

Table T17. Affine table, Site U1463. **Download table in .csv format.**

Table T18. Splice tie points, Holes U1463B–U1463D. **Download table in .csv format.**

Figure F43. Site U1463 summary showing core recovery, lithostratigraphic units, age, magnetostratigraphy biostratigraphy, MS, and wireline HSGR. Biostratigraphic zone boundary ages are shown. Age-depth model was produced from select biostratigraphic datums (see Table **T6**) (solid circles = calcareous nannofossils, open circles = planktonic foraminifers). Sedimentation rates assume a linear sedimentation rate between datums. Benthic foraminiferal assemblages were smoothed to generate this synthesis, resulting in slight differences from data presented in hole summaries. Gray bar = pipe depth.

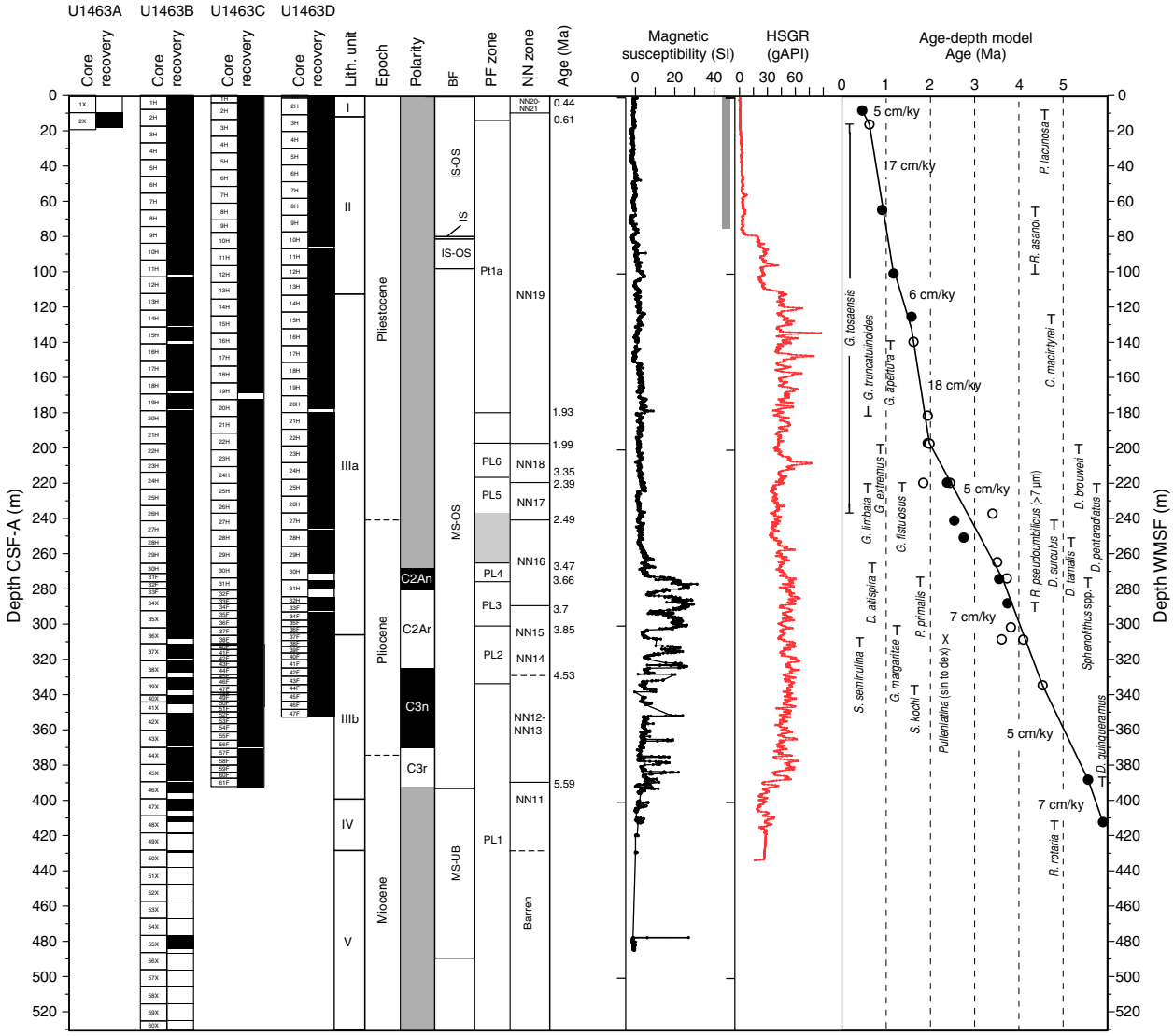

References

Blum, P., 1997. *Technical Note 26: Physical Properties Handbook—A Guide to the Shipboard Measurement of Physical Properties of Deep-Sea Cores*. Ocean Drilling Program. **http://dx.doi.org/10.2973/odp.tn.26.1997**

Chaisson, W.P., and Pearson, P.N., 1997. Planktonic foraminifer biostratigraphy at Site 925: middle Miocene–Pleistocene. *In* Shackleton, N.J., Curry, W.B., Richter, C., and Bralower, T.J. (Eds.), *Proceedings of the Ocean Drilling Program, Scientific Results,* 154: College Station, TX (Ocean Drilling Program), 3–31. **http://dx.doi.org/10.2973/odp.proc.sr.154.104.1997**

Dunlop, D.J., and Özdemir, Ö., 1997. *Cambridge Studies in Magnetism* (Volume 3): *Rock Magnetism: Fundamentals and Frontiers:* Cambridge, United Kingdom (Cambridge University Press).

Gallagher, S.J., Fulthorpe, C.S., Bogus, K., Auer, G., Baranwal, S., Castañeda, I.S., Christensen, B.A., De Vleeschouwer, D., Franco, D.R., Groeneveld, J., Gurnis, M., Haller, C., He, Y., Henderiks, J., Himmler, T., Ishiwa, T., Iwatani, H., Jatiningrum, R.S., Kominz, M.A., Korpanty, C.A., Lee, E.Y., Levin, E., Mamo, B.L., McGregor, H.V., McHugh, C.M., Petrick, B.F., Potts, D.C., Rastegar Lari, A., Renema, W., Reuning, L., Takayanagi, H., and Zhang, W., 2017a. Expedition 356 methods. *In* Gallagher, S.J., Fulthorpe, C.S., Bogus, K., and the Expedition 356 Scientists, *Indonesian Throughflow.* Proceedings of the International Ocean Discovery Program, 356: College Station, TX (International Ocean Discovery Program). **http://dx.doi.org/10.14379/iodp.proc.356.102.2017**

Gallagher, S.J., Fulthorpe, C.S., Bogus, K., Auer, G., Baranwal, S., Castañeda, I.S., Christensen, B.A., De Vleeschouwer, D., Franco, D.R., Groeneveld, J., Gurnis, M., Haller, C., He, Y., Henderiks, J., Himmler, T., Ishiwa, T., Iwatani, H., Jatiningrum, R.S., Kominz, M.A., Korpanty, C.A., Lee, E.Y., Levin, E., Mamo, B.L., McGregor, H.V., McHugh, C.M., Petrick, B.F., Potts, D.C., Rastegar Lari, A., Renema, W., Reuning, L., Takayanagi, H., and Zhang, W., 2017b. Site U1461. *In* Gallagher, S.J., Fulthorpe, C.S., Bogus, K., and the Expedition 356 Scientists, *Indonesian Throughflow.* Proceedings of the International Ocean Discovery Program, 356: College Station, TX (International Ocean Discovery Program). **http://dx.doi.org/10.14379/iodp.proc.356.106.2017**

Gallagher, S.J., Fulthorpe, C.S., Bogus, K., Auer, G., Baranwal, S., Castañeda, I.S., Christensen, B.A., De Vleeschouwer, D., Franco, D.R., Groeneveld, J.,

Gurnis, M., Haller, C., He, Y., Henderiks, J., Himmler, T., Ishiwa, T., Iwatani, H., Jatiningrum, R.S., Kominz, M.A., Korpanty, C.A., Lee, E.Y., Levin, E., Mamo, B.L., McGregor, H.V., McHugh, C.M., Petrick, B.F., Potts, D.C., Rastegar Lari, A., Renema, W., Reuning, L., Takayanagi, H., and Zhang, W., 2017c. Site U1462. *In* Gallagher, S.J., Fulthorpe, C.S., Bogus, K., and the Expedition 356 Scientists, *Indonesian Throughflow.* Proceedings of the International Ocean Discovery Program, 356: College Station, TX (International Ocean Discovery Program). **http://dx.doi.org/10.14379/iodp.proc.356.107.2017**

Gallagher, S.J., Fulthorpe, C.S., Bogus, K., Auer, G., Baranwal, S., Castañeda, I.S., Christensen, B.A., De Vleeschouwer, D., Franco, D.R., Groeneveld, J., Gurnis, M., Haller, C., He, Y., Henderiks, J., Himmler, T., Ishiwa, T., Iwatani, H., Jatiningrum, R.S., Kominz, M.A., Korpanty, C.A., Lee, E.Y., Levin, E., Mamo, B.L., McGregor, H.V., McHugh, C.M., Petrick, B.F., Potts, D.C., Rastegar Lari, A., Renema, W., Reuning, L., Takayanagi, H., and Zhang, W., 2017d. Site U1464. *In* Gallagher, S.J., Fulthorpe, C.S., Bogus, K., and the Expedition 356 Scientists, *Indonesian Throughflow.* Proceedings of the International Ocean Discovery Program, 356: College Station, TX (International Ocean Discovery Program). **http://dx.doi.org/10.14379/iodp.proc.356.109.2017**

Gradstein, F.M., Ogg, J.G., Schmitz, M.D., and Ogg, G.M. (Eds.), 2012. *The Geological Time Scale 2012:* Amsterdam (Elsevier).

James, N.P., Bone, Y., Kyser, T.K., Dix, G.R., and Collins, L.B., 2004. The importance of changing oceanography in controlling late Quaternary carbonate sedimentation on a high-energy, tropical, oceanic ramp: northwestern Australia. *Sedimentology,* 51(6):1179–1205. **http://dx.doi.org/10.1111/j.1365-3091.2004.00666.x**

Jones, H.A., 1973. *Marine geology of the Northwest Australian Continental Shelf.* Bureau of Mineral Resources, Geology and Geophysics, Canberra, Australia (Australian Government Publishing Service), 136. **http://www.ga.gov.au/corporate_data/104/Bull_136.pdf**

Kennett, J.P., and Srinivasan, M.S., 1983. *Neogene Planktonic Foraminifera: A Phylogenetic Atlas:* Stroudsburg, PA (Hutchinson Ross).

Lumsden, D.N., 1979. Discrepancy between thin section and X-ray estimates of dolomite in limestone. *Journal of Sedimentary Petrology,* 49(2):429–436. **http://dx.doi.org/10.1306/212F7761-2B24-11D7-8648000102C1865D**

Martini, E., 1971. Standard Tertiary and Quaternary calcareous nannoplankton zonation. *In* Farinacci, A. (Ed.), *Proceedings of the Second Planktonic Conference, Roma 1970:* Rome (Edizioni Tecnoscienza), 2:739–785.

Pearson, P.N., 1995. Planktonic foraminifer biostratigraphy and the development of pelagic caps on guyots in the Marshall Islands group. *In* Haggerty, J.A., Premoli Silva, I., Rack, F., and McNutt, M.K. (Eds.), *Proceedings of the Ocean Drilling Program, Scientific Results,* 144: College Station, TX (Ocean Drilling Program), 21–59. **http://dx.doi.org/10.2973/odp.proc.sr.144.013.1995**

Saito, T., 1976. Geologic significance of coiling direction in the planktonic foraminifer *Pulleniatina. Geology,* 4(5):305–309. **http://dx.doi.org/10.1130/0091-7613(1976)4<305:GSOCDI>2.0.CO;2**

van Hinsbergen, D.J.J., Kouwenhoven, T.J., and van der Zwaan, G.J., 2005. Paleobathymetry in the backstripping procedure: correction for oxygenation effects on depth estimates. *Palaeogeography, Palaeoclimatology, Palaeoecology,* 221(3–4):245–265. **http://dx.doi.org/10.1016/j.palaeo.2005.02.013**

Wade, B.S., Pearson, P.N., Berggren, W.A., and Pälike, H., 2011. Review and revision of Cenozoic tropical planktonic foraminiferal biostratigraphy and calibration to the geomagnetic polarity and astronomical time scale. *Earth-Science Reviews,* 104(1–3):111–142. **http://dx.doi.org/10.1016/j.earscirev.2010.09.003**

Young, J.R., 1998. Neogene. *In* Bown, P.R. (Ed.), *Calcareous Nannofossil Biostratigraphy:* Dordrecht, The Netherlands (Kluwer Academic Publishing), 225–265.